Nano- and chromobodies for the structural and functional analysis of the mitochondrial outer membrane associated components, Miro1 and DRP1

Dissertation

der Mathematisch-Naturwissenschaftlichen Fakultät

der Eberhard Karls Universität Tübingen

zur Erlangung des Grades eines

Doktors der Naturwissenschaften

(Dr. rer. nat.)

vorgelegt von

Funmilayo Opeyemi Fagbadebo

aus Lagos, Nigeria

Tübingen

2022

Gedruckt mit Genehmigung der Mathematisch-Naturwissenschaftlichen Fakultät der Eberhard Karls Universität Tübingen.

Tag der mündlichen Qualifikation:	11.07.2022
Dekan:	Prof. Dr. Thilo Stehle
1. Berichterstatter:	Prof. Dr. Ulrich Rothbauer
2. Berichterstatter:	Prof. Dr. Thilo Stehle

CONTENTS

FIGURES

TABLES

ABBREVIATIONS

aa	amino acid
AD	Alzheimer's disease
ALS	Amyotrophic lateral sclerosis
ATP	adenosine triphosphate
BSA	bovine serum albumin
BLI	biolayer interferometry
Cb	chromobody
cDNA	complementary deoxyribonucleic acid
CDR	complementary determining region
cfu	colony forming unit
C_H	constant domain of heavy chain
C_L	constant domain of light chain
ctr	control
Da	Dalton
DAPI	4',6-diamidino-2-phenylindole
DARPin	Designed Ankyrin Repeat Protein
DBCO	Dibenzocyclooctyne
ddH_2O	double distilled water
DMEM	Dulbecco's Modified Eagle's Medium
DMSO	dimethyl sulfoxide
DNA	deoxyribonucleic acid
dNTP	deoxynucleotide triphosphate
EDTA	ethylenediaminetetraacetic acid
ELISA	enzyme linked immunosorbent assay
F2H	fluorescent two hybrid
FBS	fetal bovine serum
FR	framework
FRAP	fluorescence recovery after photobleaching
GAPDH	glyceraldehyde 3-phosphate dehydrogenase
GBP	GFP binding protein

GED	GTPase effector domain
GFP	green fluorescent protein
GTP	guanosine-5’-triphosphate
hcAb	heavy chain antibody
HD	Huntington’s disease
HRP	horse radish peroxidase
IC-IP	intracellular-immunoprecipitation
IF	immunofluorescence
Ig, IgG	immunoglobulin G
IMAC	immobilized metal ion affinity chromatography
IP	immunoprecipitation
IPTG	isopropyl-beta-D-thiogalactopyranoside
LB	luria Bertani
mRNA	messenger ribonucleic acid
MS	mass spectrometry
n	number of technical replicates
N	number of independent experiments
Nb	nanobody
NHS	N-hydroxysuccinimide
NLS	nuclear localization signal
NTA	nitrilotriacetic acid
PAGE	polyacrylamide gel electrophoresis
PBS	phosphate buffered saline
PD	Parkinson’s disease
PEG	polyethyleneglycol
PMSF	phenylmethanesulfonylfluoride
RNA	ribonucleic acid
Rpm	rounds per minute
scFv	single chain variable fragment
sdAb	single domain antibody
SDS	sodium dodecylsulfate
TBS	tris buffered saline

TBST	tris buffered saline with 0.05% Tween 20
TEMED	tetramethylethylenediamine
v/v	volume per volume
V_H	variable domain of heavy chain
V_HH	variable domain of heavy-chain-only antibody
V_L	variable domain of light chain
w/v	weight per volume
wt	wildtype
Y2H	yeast two hybrid

ABSTRACT

Mitochondrial outer membrane (MOM) associated proteins are critical players in mitochondrial transport, dynamics, and quality control. The MOM-anchored GTPase, Miro1, is a key player in mitochondrial transport, homeostasis and mitophagy. Aberrant Miro1 function has been implicated in Parkinson's disease (PD) and amyotrophic lateral sclerosis (ALS), suggesting that Miro1 may be a potential biomarker or drug target in neuronal disorders. However, the molecular functionality of Miro1 under normal and diseased conditions is poorly known. Another MOM associated GTPase, DRP1 is required for mitochondrial and peroxisomal fission. Though abnormal mitochondrial dynamics caused by DRP1 dysregulation in neurodegenerative disorders has been implied, concise information on its involvement remain elusive.

Therefore, considering the roles played by Miro1 and DRP1 in neurodegenerative diseases and the lack of precise knowledge on their molecular functionality in these conditions, there is a great need for novel tools to study Miro1 and Drp1 in relevant research contexts.

In this thesis, nanobodies (Nbs) were selected and generated as potential tools to characterize the molecular interactions, intracellular localization, and dynamics of Miro1 and DRP1. High affinity Nbs were selected from immune libraries by stringent phage display-based techniques and validated by detailed biochemical and functional assays. Using state-of-the-art methods, selected monovalent and generated bivalent Nbs were functionalized as nanotraps which efficiently capture their endogenous and exogenous antigens for proteomic applications. Bivalent Miro1-Nbs conjugated to fluorophores by advanced site-specific labelling methods were engineered and applied for the detection of Miro1 in immunofluorescence studies. Additionally, intracellularly functional Nbs were formatted into chromobodies (Cbs) which could trace Miro1 in real time by live cell imaging. As a further step towards the *in vivo* modulation of Miro1, intracellularly functional Miro1-Nbs were combined with an F-box domain to yield Nb-degrons, which were applied for the targeted degradation of Miro1.

In summary, this study introduces a collection of novel Nbs that are promising tools for the biochemical characterization, intracellular visualization, and modulation of Miro1 and DRP1. The generation and application of these Nbs demonstrate the applicability of Nbs for the functional characterization of mitochondrial proteins.

ZUSAMMENFASSUNG

Mitochondriale Proteine, die mit der äußeren Membran (MOM) assoziiert sind, spielen eine entscheidende Rolle für den mitochondrialen Transport, die mitochondriale Dynamik und Umsatz. Die MOM-verankerte GTPase Miro1 ist ein wichtiger Akteur beim mitochondrialen Transport, der Homöostase und der Mitophagie. Eine gestörte Miro1-Funktion wurde unter anderem bei der Parkinson-Krankheit (PD) und der amyotrophen Lateralsklerose (ALS) festgestellt, was darauf hindeutet, dass Miro1 ein potenzieller Biomarker oder Angriffspunkt für Medikamente bei neuronalen Störungen sein könnte. Die molekulare Funktionalität von Miro1 unter normalen und krankhaften Bedingungen ist jedoch kaum bekannt. Eine weitere MOM-assoziierte GTPase, DRP1, ist für die mitochondriale und peroxisomale Teilung erforderlich. Obwohl es Hinweise auf eine abnorme mitochondriale Dynamik gibt, die durch eine Dysregulation von DRP1 bei neurodegenerativen Erkrankungen verursacht wird, sind präzise Informationen über die Beteiligung von DRP1 nach wie vor schwer zu finden.

In Anbetracht der Rolle, die Miro1 und DRP1 bei neurodegenerativen Erkrankungen spielen sowie des Mangels an genauen Kenntnissen über ihre molekulare Funktionsweise bei diesen Erkrankungen besteht daher ein großer Bedarf an innovativen Methoden zur Untersuchung von Miro1 und Drp1 in relevanten wissenschaftlichen Bereichen.

In dieser Arbeit wurden Nanobodies (Nbs) als potenzielle Werkzeuge zur Charakterisierung der molekularen Interaktionen, der intrazellulären Lokalisierung und der Dynamik von Miro1 und DRP1 isoliert und erzeugt. Nbs mit hoher Affinität wurden aus Immunbibliotheken durch strenge Phagen-Display-basierte Techniken isoliert und durch detaillierte biochemische und funktionelle Tests validiert. Mit modernsten Methoden wurden isolierte monovalente und generierte bivalente Nbs als Nanotraps funktionalisiert, die ihre endogenen und exogenen Antigene für proteomische Anwendungen effizient binden. Mit Fluorophoren konjugierte bivalente Miro1-Nbs, wurden zum Nachweis von Miro1 in Immunfluoreszenzstudien entwickelt und eingesetzt. Darüber hinaus wurden intrazellulär funktionelle Nbs zu Chromobodies (Cbs) formatiert, mit denen Miro1 in Echtzeit durch Bildgebung in lebenden Zellen verfolgt werden kann. In einem weiteren Schritt zur In-vivo-Modulation von Miro1 wurden intrazellulär funktionelle Miro1-Nbs mit einer F-Box-Domäne kombiniert, um Nb-Degrons zu generieren, die für den gezielten Abbau von Miro1 eingesetzt wurden.

Zusammenfassend wird in dieser Studie eine Sammlung neuartiger Nbs entwickelt, die vielversprechenden Werkzeuge für die biochemische Charakterisierung, intrazelluläre Visualisierung und Modulation von Miro1 und DRP1 darstellen. Die Generierung und

Anwendung dieser Nbs zeigen die Anwendbarkeit von Nbs für die funktionelle Charakterisierung von mitochondrialen Proteinen.

1 INTRODUCTION

1.1 Mitochondria: structure and function

The term, mitochondrion, coined from the Greek words, ‘mitos’ and ‘chondros’ meaning thread and granule was introduced by Carl Benda (Benda 1898) to describe the appearance of ubiquitous structures which were found to be responsible for cellular respiration in the mid-1900s (Ernster and Schatz 1981). Since then, efforts have revealed that mitochondria are sites of a vast array of metabolic and signaling processes which are still largely uncharted (Pagliarini and Rutter 2013).

Morphologically, mitochondria are composed of an outer membrane (MOM) and an inner membrane (MIM) separated by the intermembrane space (IMS); cristae which are formed by the extensively folded inner membrane; and the mitochondrial matrix. These compartments all perform distinct roles and vary structurally in different cell types to meet up with mitochondrial functional needs (Glancy et al. 2020).

Apart from the primary role of energy (ATP) production mainly by oxidative phosphorylation (OXPHOS), mitochondria also play significant part in Ca^{2+} signaling. Ca^{2+} ions can be transiently stored in the matrix or released for cytosolic buffering. Interactions between mitochondria and the ER at mitochondria-ER contact sites (MERCs) allow for Ca^{2+} exchange (Malli et al. 2003; Petersen 2002) and phospholipid metabolism (Peruzzo et al. 2020). Additionally, mitochondria are both the major sources and targets of reactive oxygen species (ROS) and therefore control cellular redox homeostasis (Ma et al. 2020; Collins et al. 2012). Under conditions of stress and ageing, mitochondrial ROS cause oxidative damage to mitochondrial proteins, lipids and mitochondrial DNA causing inflammation (Zhou et al. 2011; Nakahira et al. 2011) and the release of pro-death factors. As a result of this, mitochondria play a central role in the initiation of apoptotic cell death. Other known functions of mitochondria are iron metabolism (Levi and Rovida 2009) and in the regulation of innate immunity (Zhang et al. 2010; West et al. 2011; Weinberg et al. 2015).

Mitochondria are highly dynamic organelles, constantly undergoing processes of transport, fission, fusion, and removal to meet up with energy demands or changes in their environment. Remarkably, impairment in these mitochondrial processes have been associated with several pathological disorders (reviewed in (Mishra and Chan 2014; Flannery and Trushina 2019; Suárez-Rivero et al. 2016)).

1.1.1 Mitochondrial transport

To maintain proper cellular functions, a comprehensive regulation of mitochondrial trafficking is required. Depending on the cell type, mitochondria are shuttled to areas needing high ATP supply and calcium buffering. For example, in neurons, mitochondria are actively transported from the cell body to synapses (Bogan and Cabot 1991), active growth cones and branches (Misgeld and Schwarz 2017; Ruthel and Hollenbeck 2003). Studies have also reported that mitochondria migrate to the top of migrating cancer cells (Arismendi-Morillo et al. 2012; Desai et al. 2013) to provide onsite energy to the cells.

In metazoans, mitochondria are transported along the actin- and microtubule-based cytoskeletal network by kinesins/dynein motors (Reis et al. 2009; Rube and Van Der Bliek 2004). For long range trafficking, mitochondria are tethered to microtubules by the interaction of the adaptor proteins TRAK1/2 with the MOM-anchored protein Miro1 on one side and with the kinesin/dynein motor on the other (Fransson et al. 2006). The short-range actin-based transport and anchoring of mitochondria is facilitated by the interaction of Myo19 and Miro proteins (Oeding et al. 2018). Also implicated in mitochondrial transport are the Metaxins, MTX1 and MTX2, components of the SAM complex which bind to MIRO-1 and kinesin light chain KLC-1, forming a complex to mediate kinesin-1-based movement of mitochondria.(Zhao et al. 2021). Disrupted In Schizophrenia 1 (DISC1), is another protein which facilitates kinesin-mediated mitochondrial trafficking by interacting with GTP-bound Miro1(Norkett et al. 2020). Mitochondrial trafficking is certainly a process involving the interplay of different proteins and its significance for proper physiological function is underscored by its involvement in the pathogenesis of several neurodegenerative diseases (Magrané et al. 2014).

1.1.2 Mitochondrial dynamics

Constant mitochondrial fission and fusion are mandatory for cell growth and survival. The balance of fission and fusion events, which is termed mitochondrial dynamics, helps to regulate the size, number, distribution, quality and transport of mitochondria in cells (Yu et al. 2020).

Mitochondrial fission is required to generate new mitochondria from existing ones, for example, to distribute mitochondria to daughter cells during cell division (Mishra and Chan 2014). On the other hand, fission events also occur to facilitate the spatial segregation of damaged mitochondria.

Mitochondrial fission in mammals is mediated by DRP1, a dynamin related GTPase. DRP1 forms complexes on the MOM and constricts the mitochondria to cause fission (Ni et al. 2015).

Four MOM-anchored proteins interact with DRP1 in the process of mitochondrial division (Loson et al. 2013). Mitochondrial fission protein 1 (Fis1), recruits and functions an adapter for DRP1 (Ihenacho et al. 2021). Second is the mitochondria fission factor (Mff) which helps to recruit DRP1 to mitochondria (Gandre-Babbe and van der Bliek 2008). Lastly, mitochondrial dynamics proteins of 49kDa and 51kDa (MiD49 and MiD51) regulate mitochondrial fission by targeting DRP1 to the MOM. The knockdown of MiD49 and MiD51 significantly impaired DRP1-dependent mitochondrial fission in fibroblasts (Palmer et al. 2011; Samangouei et al. 2018).

The fusion of mitochondria plays a critical role in the maintenance of mitochondrial function. It entails the merging, first of the MOM, and then the MIM of two distinct mitochondria. The fusion process serves to prevent the accumulation of mutations during aging and to enhance the spreading of molecules and mtDNA throughout the mitochondrial compartment (Suárez-Rivero et al. 2016). It has been proposed as a possible rescue mechanism for damaged mitochondria from elimination (Suárez-Rivero et al. 2016). Fusion of the MOM is mediated by the dynamin related GTPases, Mitofusin 1 and 2 (Mfn1 and Mfn2). Subsequent fusion of the MIM is facilitated by the dynamin related GTPase, optic atrophy 1 (OPA1) (Meeusen et al. 2004; Xian and Liou 2021).

In humans, genetic defects in proteins which regulate mitochondrial dynamics have been implicated in mitochondrial disorders. For example, mutations in Mfn2 gene has been linked to Charcot-Marie-Tooth neuropathy type 2A (Cho et al. 2007). Also, dominant optic atrophy (DOA), a neuro-ophthalmic disorder marked by degeneration of the optic nerves, is associated with mutations in nuclear genes encoding OPA1 (Alexander et al. 2000). The imbalance of mitochondrial fission and fusion could be causative factors in neurodegenerative diseases exemplified by DRP1 mediated hyper-fission in the fibroblasts of Huntington's disease patients (Xian and Liou 2021).
Consequently, detailed understanding of the roles played by proteins involved in mitochondrial dynamics are required.

1.1.3 Mitochondrial quality control

Mitochondrial quality control systems regulate the effects of mitochondrial stress and damage by mechanisms ranging from the degradation of individual proteins up to the removal of mitochondria by autophagy, which is termed mitophagy (Roca-Portoles and Tait 2021). To compensate for the loss in mitochondrial populations due to mitophagy, mitochondrial biogenesis mechanisms come into play to ensure the growth and division of pre-existing mitochondria (Jornayvaz and Shulman 2010). Therefore, maintenance of healthy

mitochondrial networks requires a tightly regulated balance between mitochondrial biogenesis and mitophagy.

Many mechanisms are involved in the maintenance of mitochondrial “health”. First, the mitochondrial proteolytic system degrades misfolded proteins that could potentially affect mitochondrial function (Baker and Haynes 2011). Also, damaged MOM proteins can be degraded by the proteasome (Karbowski and Youle 2011). Additionally, segregation of damaged mitochondria via the fission process and exchange of material between healthy mitochondria via the fusion process helps to maintain mitochondrial health (van der Bliek et al. 2013). Furthermore, mitochondria-derived vesicles (MDVs) formed under oxidative stress conditions could fuse with lysosomes for the degradation of oxidized mitochondrial proteins (Roberts et al. 2016). Ultimately, irreversibly damaged mitochondria would be degraded by PINK1/Parkin-dependent or independent mitophagy. Of these, the best characterized pathway is the PINK1/Parkin-mediated mitophagy. Under healthy conditions PINK1, a serine/threonine kinase, is imported into the mitochondrial matrix and subsequently degraded by mitochondrial proteases (Lazarou et al. 2015). However, upon mitochondrial damage and depolarisation, PINK1 accumulates on the MOM (Jin et al. 2010). Here, PINK1 mediates ubiquitin phosphorylation causing the recruitment and activation of Parkin, a ubiquitin E3-ligase, to the MOM (Kazlauskaite and Muqit 2015). Activated Parkin then ubiquitinates a wide range of MOM-localized proteins such as Miro1/2, Mitofusins, VDAC and Tom20 which are critical for mitochondrial transport and function. This arrests motility and leads to segregation and subsequent degradation of the damaged mitochondrion (Sarraf et al. 2013).

As a result of the defects in mitochondrial quality control which have been implicated in Parkinson’s, Huntington’s, Alzheimer’s disease and Amyotrophic lateral sclerosis (ALS), the precise roles played by the implicated mitochondrial proteins warrant further study (Pickles et al. 2018).

1.2 The atypical GTPase Miro1

Miro1 is a member of the Miro family of Ras GTPases (Boureux et al. 2007; Reis et al. 2009; Yamaoka and Hara-Nishimura 2014) which comprises Miro1 and Miro2. Both proteins are highly similar with ~60% amino acid sequence homology. Miro1 and Miro2 are ~70kDa consisting of 618 amino acid residues (Reis et al. 2009) and have been found to be evolutionary conserved from yeast to mammals (Vlahou et al. 2011).

Miro1 is composed of a C-terminal transmembrane domain which is anchored in the mitochondrial outer membrane (MOM). The cytoplasmic exposed region comprises two distinct

N- and C-terminal GTPase domains flanking a pair of calcium binding EF-hands (Fransson et al. 2003, 2006) (**Figure 1)**. Notably, the N-terminal GTPase (nGTPase) domain of Miro1 is structurally and functionally distinct from its C-terminal (cGTPase) domain. It has been shown that the nGTPase specifically hydrolyses GTP while the cGTPase shows promiscuous NTP activity (Klosowiak et al. 2013; Smith et al. 2020) which makes Miro1 as well as Miro2, the only currently known proteins that contain two distinctly active GTPase domains (Kay et al. 2018; Grossmann et al. 2020).

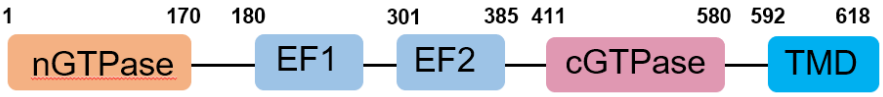

Figure 1*. Schematic illustration of Miro1 domain structure*

Overexpression of Miro1 in mammalian cells resulted in the formation of thread-like interconnected mitochondria, but this phenotype disappeared in cells expressing Miro1 with non-functional nGTPase and EF hand domains (Fransson et al. 2006; Reis et al. 2009) highlighting the significance of these domains for mitochondrial morphology. In developing Miro1 knockout mouse models, it was observed that mice with global Miro1 knockout were cyanotic and died at birth, whereas mice with neuron-specific Miro1 knockout developed severe neuronal damage and died prematurely (Nguyen et al. 2014; Kay et al. 2018).

1.2.1 The central role of Miro1 in mitochondrial transport

Especially in neurons, bidirectional transport and positioning of mitochondria on microtubules are necessary for maintaining energy supply and other functions of cells. As a mitochondrial anchor, Miro1 interacts with the adapter proteins TRAK1 and TRAK2 via its cytoplasmic domains. (Fransson et al. 2006). The TRAK proteins further recruit kinesin-1 (KIF5B) or dynein/dynactin, which confer the transport of mitochondria along microtubules (van Spronsen et al. 2013; MacAskill et al. 2009a) as shown in **Figure 2**. Notably, the interaction of Miro1 with TRAK1 can recruit both kinesin and dynein/dynactin for anterograde and retrograde movement of mitochondria in the axons while interactions with TRAK2 forms a functional motor complex for retrograde mitochondrial movement at dendrites (van Spronsen et al. 2013). Though the role of TRAK proteins in the Miro1 mediated transport of mitochondria is accepted, it has been reported that Miro1 may be able to bind directly to KIF5 *in vitro* without TRAK involvement (MacAskill et al. 2009b).

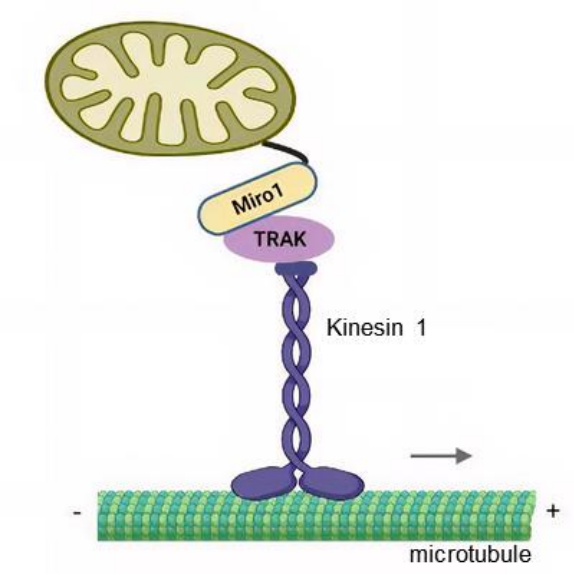

Figure 2. The role of Miro1 in mitochondrial transport. Miro1 and adaptor proteins, TRAK tether mitochondria to Kinesin-1 (KIF5B) for the anterograde movement of mitochondria on microtubules.

Studies have also shown that the microtubule-based transport of mitochondria can be regulated by the Ca^{2+} binding functions of Miro1. Here, at elevated intracellular Ca^{2+} levels, the anchoring of mitochondria to KIF5 motors is inhibited by Ca^{2+} binding at Miro1 EF hands (Saotome et al. 2008; MacAskill et al. 2009a; Wang and Schwarz 2009). Furthermore, mitochondrial transport speed was linked with intramitochondrial Ca^{2+} levels which raised questions on how Miro1's cytosolic domains could influence Ca^{2+} influx into the mitochondrial matrix (Chang et al. 2011; Grossmann et al. 2020).

Other mitochondrial trafficking functions of Miro1, for example, during cytokinesis have been described. Here, Cenp-F is recruited to mitochondria by Miro1 which leads to association of mitochondria with microtubule growing tips and subsequent transport to daughter cells (Kanfer et al. 2015). Similar to its role in the intracellular trafficking of mitochondria, Miro1 is a key regulator of mitochondrial transport from mesenchymal stem cells to epithelial cells via intercellular tunneling nanotubes (TNT) (Ahmad et al. 2014; Babenko et al. 2018).

Though the involvement of Miro1 in mitochondrial transport has been well described, there are still unanswered questions about the influence of intramitochondrial and cytosolic Ca^{2+} levels (Saotome et al. 2008; Chang et al. 2011), and the specific contribution of Miro1 domains (Stephenson 2010).

1.2.2 Miro1 in mitochondrial quality control

The maintenance of the mitochondrial network requires active coordination of mitochondrial biogenesis and mitophagy. Removal of damaged mitochondria is particularly important in post-mitotic cells like neurons, which are unable to dilute toxic components through cell division (Grossmann et al. 2020).

During the mitophagy cascade, the ubiquitination of Miro1 by Parkin and later, its proteasomal degradation is primarily responsible for the halt in movement of damaged mitochondria (Birsa et al. 2014; Lazarou et al. 2015; Liu et al. 2012; Kazlauskaite et al. 2014). Some studies report that Miro1 directly interacts with PINK1 and is phosphorylated creating a signal for the ubiquitination of Miro1 by Parkin (Wang et al. 2011; Weihofen et al. 2009).

Apart from its interaction with PINK1 and Parkin, the ubiquitination and degradation of Miro1 from the MOM could be mediated by other proteins. It has been shown that the kinase, LRRK2 complexes with Miro1 to promote Miro1 degradation from damaged mitochondria (Hsieh et al. 2016). Notably, the pathological impairment of Miro1 clearance has been reported even in the presence of functional Parkin and LRRK2 suggesting that Miro1 might be involved in other interactions which contribute to its removal during mitophagy (Shaltouki et al. 2018; Hsieh et al. 2019). Further studies are therefore required to characterize the role played by the Miro1 interactome during mitophagy.

1.2.3 Miro1 dysfunction in neurodegenerative diseases

The central roles played by Miro1 in mitochondrial transport and mitophagy are particularly relevant for neuronal health. Impaired Miro1 ubiquitination for proteasomal degradation has been linked to Parkin and LRRK2 mutants found in some Parkinson's disease (PD) patients and in fibroblasts from an at-risk cohort (Hsieh et al. 2016; Nguyen et al. 2021). In these studies, a direct connection between Miro1 and neurodegeneration in Parkinson's disease was mapped. The accumulation of damaged mitochondria resulting from aberrant mitophagy leads to a stress response and subsequent neuronal damage. Due to the direct and functional interaction between Miro1 and other proteins implicated in PD, it has been proposed as a potential biomarker and druggable target (Hsieh et al. 2016; Grossmann et al. 2020).

Amyotrophic lateral sclerosis (ALS), a motor neuron disease which is characterized by progressive neurodegeneration has also been linked with Miro1 dysfunction (Hardiman et al. 2017). It was reported that significantly lower Miro1 expression levels were detected in the spinal cord of ALS patients which could be responsible for the deficits in Miro1-mediated mitochondrial movement in the motor neurons (Zhang et al. 2015). It was suggested that the

increase in PINK1/Parkin mediated Miro1 degradation was facilitated by a mutant superoxide dismutase (SOD1) associated with ALS (Moller et al. 2017).

1.3 Dynamin related protein DRP1

Membrane remodeling processes such as mitochondrial fission are very important for maintaining cellular homeostasis and are mediated by dynamin superfamily mechanoenzymes (Ford and Chappie 2019). One of such proteins, DRP1, a large GTPase about ~80kDa is normally localized in the cytosol but recruited to the MOM upon induction of the mitochondrial fission process (Smirnova et al. 2001). Structurally, DRP1 is composed of an N-terminal GTPase domain; a middle domain comprising the Bundle Signalling element (BSE) and a four-helix bundle known as the stalk domain; a B-Insert or Variable domain which is analogous to the Pleckstrin homology domain found in dynamins; and a GTPase effector domain (GED) whose C-terminal coiled coil is the site of multimerization (Fröhlich et al. 2013; Otera et al. 2013; Kalia et al. 2018; Kraus et al. 2021). A graphical depiction of DRP1 domain structure is shown in **Figure 3**.

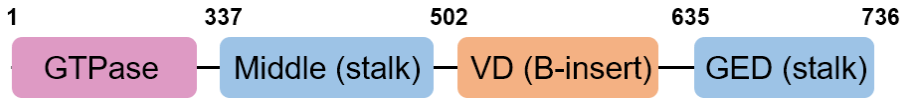

***Figure 3**. Graphical illustration of DRP1 domain organization*

Post-translation modifications of DRP1 has been shown to play critical roles in its function. For instance, DRP1 phosphorylation at Serine (Ser) 616 by various kinases including PINK1 leading to increased mitochondrial fragmentation (Kashatus et al. 2015; Han et al. 2020). Also, phosphorylation at Ser637 by cyclic AMP-dependent protein kinase A was found to inhibit intramolecular interactions between the GED and GTPase domains of DRP1 causing inhibition of GTPase activity and thus confer elongated mitochondria phenotypes (Gomes et al. 2011; Cribbs and Strack 2007).

In the absence of functional DRP1, cells have perinuclear mitochondrial networks which are elongated and extensive. Also, mutation or knockout of DRP1 has been shown to delay the release of cytochrome C in cells suggesting that DRP1 might have pro-apoptotic functions (Munoz-Pinedo et al. 2006).

1.3.1 Role of DRP1 in the regulation of mitochondrial dynamics

Mitochondrial dynamics involves the coordinated cycles of fission and fusion that mitochondria undergo to maintain their size and distribution (Tilokani et al. 2018). Mitochondrial fission occurs in multiple steps resulting in the division of a mitochondrion into two daughter mitochondria. To facilitate fission, it is hypothesized that DRP1 oligomers may be recruited to the MOM by mitochondrial adaptor proteins Fis1, Mff, MiD49/51(Loson et al. 2013; Otera et al. 2013) since it lacks the Pleckstrin homology domain possessed by other membrane binding dynamins(Pagliuso et al. 2018). After recruitment to the MOM, DRP1 dimers assemble into ring-like structures which wrap around the mitochondrial tubule (see **Figure 4**). The GTPase activity of DRP1 provides the energy needed to drive the membrane constriction needed for scission(Kalia et al. 2018; Otera et al. 2013; Pagliuso et al. 2018; Smirnova et al. 2001).

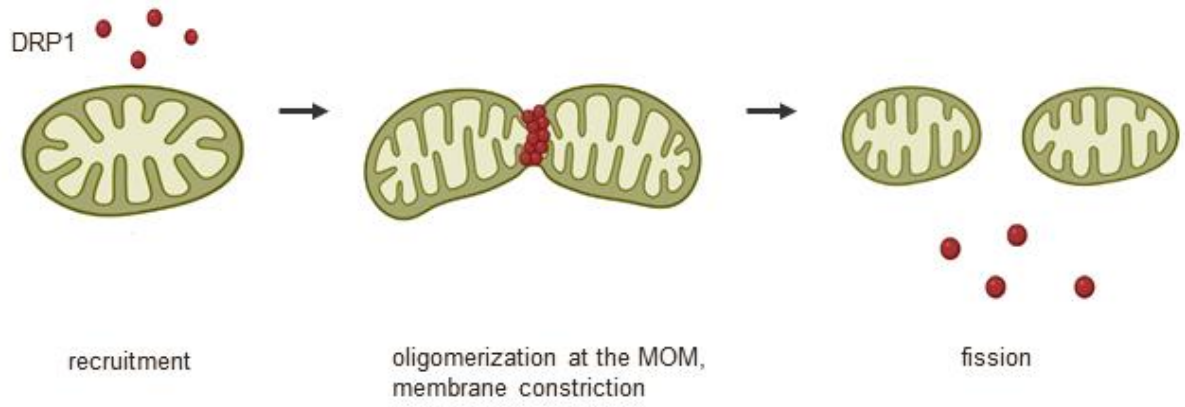

Figure 4. *The role of DRP1 in mitochondrial dynamics. DRP1 is recruited to mitochondria to oligomerize at fission sites on mitochondria which leads to constriction of the MOM and subsequent fission.*

Although the formation of ring-like structures around mitochondrial constriction sites by DRP1 has been studied in detail, the mechanism of how DRP1 mediates membrane cleavage is still unclear (Yoon et al. 2001). It has been speculated that dynamin 2 (DNM2) may be involved in the final cleavage event required for mitochondrial fission (Lee et al. 2016). However, this hypothesis has been repeatedly rejected (Kamerkar et al. 2018; Fonseca et al. 2019).

The importance of DRP1 also arises from reports that dysfunctional mitochondrial fission caused by mutations in human DRP1 is lethal (Waterham et al. 2007). Despite the well-

characterized role of DRP1 in mitochondrial fission, many questions about the molecular mechanism of DRP1-mediated membrane constriction remain unanswered.

1.3.2 The role of DRP1 in apoptosis

The fragmentation of mitochondria as a prelude to apoptosis is a highly conserved process in eukaryotes (Fannjiang et al. 2004; Jagasia et al. 2005). Thus, DRP1 associates with pro-apoptotic proteins, Bax and Bak at apoptotic foci in mitochondria (Karbowski et al. 2002). Following the induction of apoptosis, Bax oligomers mediate the formation of membrane pores responsible for the release of mitochondrial contents such as cytochrome c, Smac, and mtDNA into the cytosol (McArthur et al. 2018; Riley et al. 2018). Recently, it was shown that the interaction between Bax and DRP1 is induced at apoptotic foci and stabilized until cell death further establishing that DRP1 activates Bax for apoptosis (Jenner et al. 2022). Notably DRP1-deficient cells also undergo apoptosis (Parone et al. 2006), thus the functional role of DRP1 in this process is still unclear.

1.3.3 Neuropathologies associated with DRP1

Extensive mitochondrial division is a hallmark event in multiple human diseases namely neurodegenerative disorders and cancer (Serasinghe and Chipuk 2017). Up-regulation of DRP1 expression leading to increased mitochondrial fragmentation has been found in Alzheimer's disease (AD). A study on the postmortem brains of AD patients demonstrated elevated mRNA levels of fission genes including DRP1 and a concomitant increase in fission resulting in synaptic deficiencies and neurodegeneration (Cho et al. 2009). The study further linked the increased fission to the prevalence of s-nitrosylated DRP1 (SNO-DRP1) in the samples examined (Cho et al. 2009; Reddy et al. 2011). Preventing s-nitrosylation of DRP1 by mutations at Cys644 reportedly protected neurons from the effects of DRP1 upregulation. These findings suggest that DRP1 might be a molecular marker or therapeutic target in AD (Oliver and Reddy 2019).

Mitochondrial dysfunction as a result of elevated DRP1 levels were also observed in Huntington’s disease (HD) (Reddy 2009) and ALS(Joshi et al. 2018). Notably, the dysfunction of DRP1 in HD and ALS were linked with the downstream effects of aberrant huntingtin and SOD1 gene mutations (Song et al. 2011; Tafuri et al. 2015). However, the involvement of DRP1 in these and other neurodegenerative diseases (Oliver and Reddy 2019) underscores the need for detailed characterization of DRP1 as an important step toward understanding the underlying molecular causes of these diseases.

1.4 Tools for studying MOM-associated proteins, Miro1 and DRP1

Despite the availability of *in vitro* and *in vivo* studies on Miro1, detailed information about its structure-function dynamics and the exact role of its two GTPase domains are still unknown (Smith et al. 2020). Biochemical assays or cell biological approaches such as immunofluorescence microscopy preferentially use conventional antibodies against Miro1 or against corresponding epitope labels. These methods are however insufficient to monitor the real-time dynamics of Miro1. Studies involving Miro1 visualization rely either on ectopic expression of fluorescent fusion constructs or short epitope tagged Miro1 and consecutive staining with mitochondrial dyes for imaging. However, the function and interactions of exogenous Miro1 may not accurately mirror that of the endogenous protein. So far, the paucity of specific tools to shed light on the molecular functionality of Miro1 in its physiologically relevant state might be a limitation to understanding Miro1's involvement in mitochondrial quality control and mitochondrial transport.

The function of DRP1 as a mediator of mitochondrial fission has been extensively studied. Studies on DRP1 mostly rely on stable cell lines expressing DRP1 mutants and transient expression of epitope-tagged variants (Smirnova et al. 2001; Lee et al. 2004; Song et al. 2011; Loson et al. 2013; Guo et al. 2017; Luo et al. 2017; Joshi et al. 2018; Kamerkar et al. 2018; Jenner et al. 2022). Though fluorescently labelled DRP1 have been used in several studies (Hatch et al. 2016; Guo et al. 2017; Ji et al. 2017; Whitley et al. 2018), altered oligomerization dynamics of GFP-tagged DRP1 monomers have been recently reported (Montecinos-Franjola et al. 2020). This could be a disadvantage in studies focused on the stoichiometry of DRP1 self-assembly at fission foci.

Alternatively, antibodies specific for DRP1 and phosphorylated DRP1 (at Ser616 and Ser637) have been applied for the characterization of DRP1 by IF and biochemical assays (Bossy et al. 2010; Kashatus et al. 2015; Roe and Qi 2018). However, these specific and well-characterized reagents are insufficient to monitor the real-time dynamics of DRP1 in normal and apoptotic fission events.

To adequately understand the molecular significance of Miro1 and DRP1 in mitochondrial health and related pathologies, novel tools and approaches need to be explored. The application of such tools should be based on affinity, specificity, and provide spatiotemporal information about Miro1 and DRP1 without compromising their functions at the molecular level.

1.5 Affinity reagents

Currently used methods in cell biology such as proteomic studies, biochemical assays and microscopy rely heavily on affinity reagents. In addition to classical antibodies, these include antibody fragments, non-immunoglobulin scaffolds, peptides, nucleic acids and small molecules, which are usually selected from extensive libraries.

Antibodies, produced by B-lymphocytes, are key components of the humoral immune system of mammals which have also found great use as research reagents. In biochemical research contexts, the immunoglobulin gamma (IgG) isotype is the most used. IgGs have a molecular weight of ~150 kDa, is are structurally composed of two identical light chains and two identical heavy chains linked by disulfide bridges. The heavy and light chains comprise constant (C_H and C_L) and variable (V_H and V_L) domains depicted in (**Figure 5A**). The V_H and V_L have conserved regions as well as three complementarity determining regions (CDRs) which confer the paratope of the IgG. The use of IgGs as affinity reagents is limited by their complex structure, batch-to-batch variation, poor functionality in intracellular applications and costly and labour some production (Frenzel et al. 2013; Slastnikova et al. 2018). These limitations stimulated the search for smaller antibody fragments such as single chain variable fragments (scFvs), Fab fragments, diabodies and minibodies (**Figure 5B**) (Frenzel et al. 2013). Despite the advantages of the scFv and Fab fragments due to their smaller size (Gebauer and Skerra 2015), they often show lower thermal stabilities and reduced affinities compared to full length IgG (Kang and Seong 2020). Furthermore, due to the hydrophobic residues present on the interfaces between the V_H and V_L in scFvs, they show reduced solubility, improper folding and aggregation during their intracellular expression (Biocca et al. 1990). Nonetheless, intracellularly functional scFvs targeting mitochondrial and cytosolic antigens have been reported (Beerli et al. 1994a, b; Thammasit et al. 2015; Cioni et al. 2019; Flego et al. 2019; Preger et al. 2020).

The use of non-Ig scaffold-based affinity reagents have emerged as an alternative to conventional antibodies(Nygren and Skerra 2004). So far, over 20 different types of non-Ig scaffolds are currently in use including reagents such as affibodies, avimers, monobodies, DARPins (designed ankyrin repeat proteins), anticalins and Kunitz domain proteins (Schlehuber and Skerra 2005; Koide and Koide 2007; Skerra 2007; Skrlec et al. 2015). These novel molecules are engineered to have desired properties such as small size, pharmacokinetic properties optimal for their intended use, rapid folding, high physicochemical stability, absence of cysteines for intracellular applications, ease of conjugation or reformatting, and ease of recombinant expression and production (Lofblom et al. 2011). Examples of non-Ig based affinity reagents are depicted in **Figure 5C**.

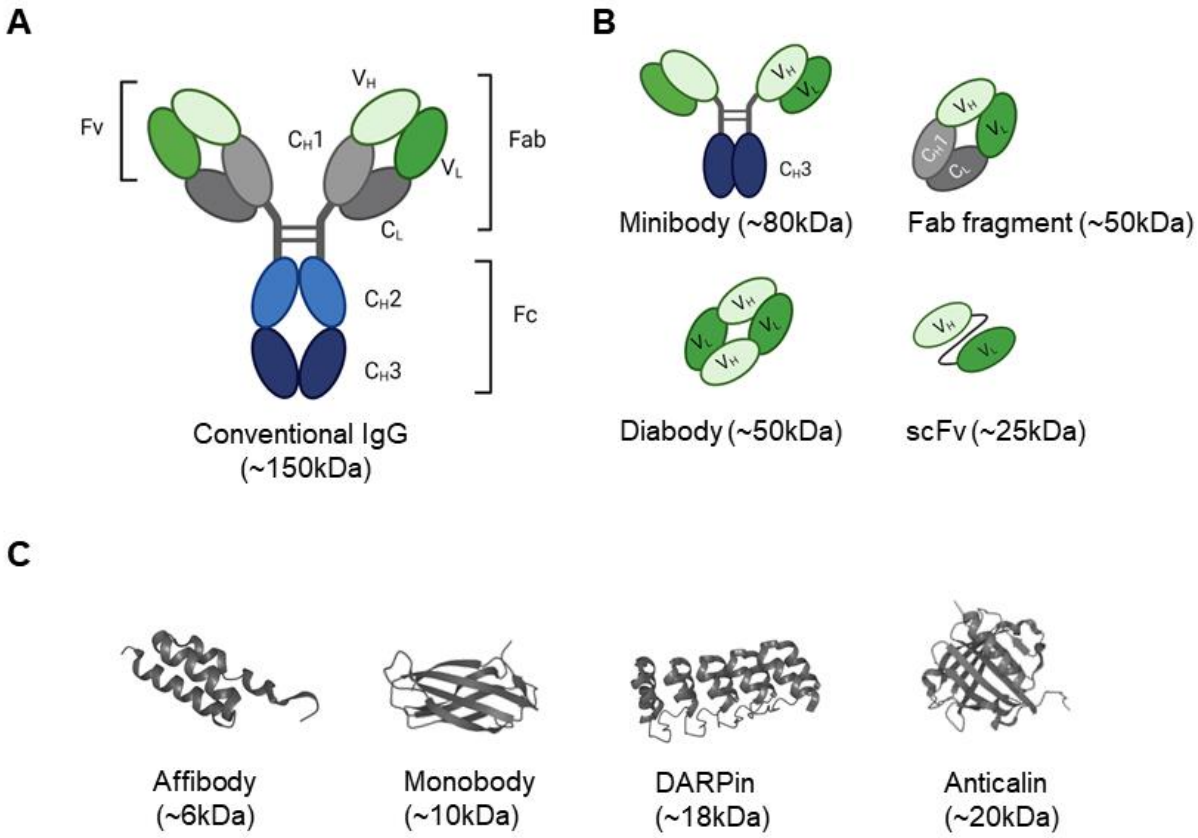

***Figure 5**. Protein based affinity reagents for biochemical research. Schematic representation of (**A**) conventional IgG molecule and (**B**) smaller Ig-based scaffolds comprising the variable heavy (V_H) and variable light (V_L) domains for antigen recognition. (**C**) Non-Ig based proteins used as affinity reagents. Exemplary structures were sourced and modified from the Protein Data Bank (affibody: 2KZI; monobody: 3RZW; DARPin: 6FP9; anticalin:4IAW) (Berman et al. 2000).*

1.6 Nanobodies

In 1993, Hamers-Casterman and his co-workers identified two classes of heavy chain-only immunoglobulin-like molecules (hcAb) in the sera of members of the *Camelidae* family (Hamers-Casterman et al. 1993). They were described as IgG isotype 2 possessing a long hinge region and IgG isotype 3 which had a shorter hinge region. These IgG2 and IgG3 molecules are composed of two constant domains (C_H2 and C_H3), a hinge region, and an

antigen binding or variable heavy chain domain (V_HH) also known as the nanobody (Nb) or single domain antibody (sdAb) (**Figure 6A**).

Nanobodies are the smallest antigen binding reagents (~15kDa) which are derived from an Ig-scaffold. Similar to V_H and V_L domains of conventional IgGs, the Nb comprises four conserved framework regions (FR) which surround three hypervariable CDRs as illustrated in **Figure 6B**. Although all CDRs, as well as parts of the scaffold, can contribute to antigen binding, in most Nbs studied to date, CDR3 represent the major contact sites (Muyldermans 2013).

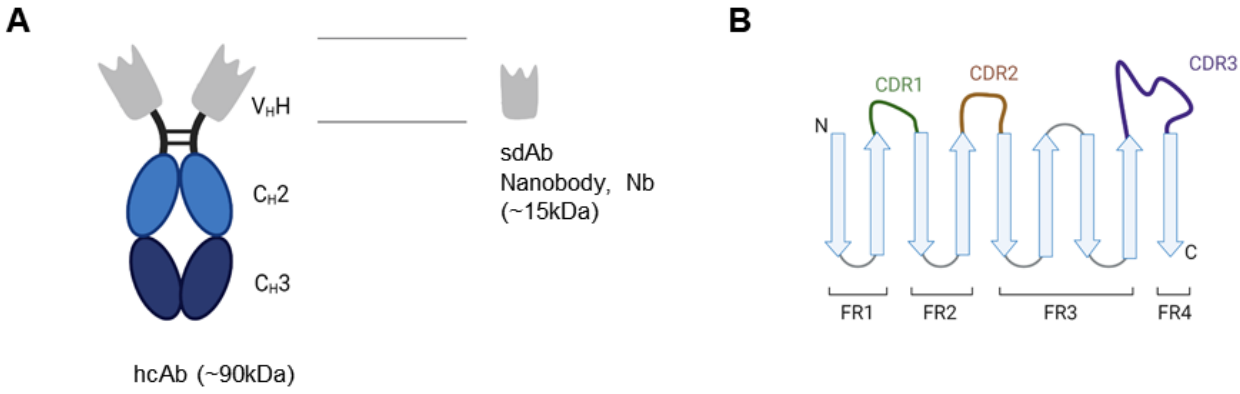

Figure 6. *Structural features of heavy chain-only antibodies and Nbs. Illustration of a (**A**) heavy-chain only antibody showing the V_HH domain known as the single domain antibody, sdAb or nanobody, Nb (**B**) schematic representation of the Nb secondary structure of 9 beta sheets comprising 4 framework regions (FR1 to FR4) separated by loops of which 3 are hypervariable (the CDR1 coloured in green; CDR2 coloured brown and CDR3, coloured purple). Adapted from (Mitchell and Colwell 2018) and (Berland et al. 2021).*

Compared to the variable heavy chain (V_H) domains of conventional antibodies, Nbs usually have better solubility due to the presence of hydrophilic residues in FR2 rather than the hydrophobic amino acids necessary for interaction with the light chain (Muyldermans 2013). They also demonstrate better physicochemical stability by retaining their function at high temperatures of up to 90°C, in the presence of proteases and under extreme pH conditions (Steeland et al. 2016; van der Linden et al. 1999). Additionally, like any VH domain the structure of Nbs is stabilized by an intramolecular disulfide bridge between cysteine residues located in FR1 and FR3 Regarding the antigen binding capacity of Nbs, long and flexible CDR3 loops increase the ability of Nbs to bind cryptic concave epitopes such as enzyme activation

sites (Zavrtanik et al. 2018). However, Nbs that bind their targets with high affinity despite short CDR3 loops have also been identified (Rothbauer et al. 2006). Although most of the Nbs preferably bind structural, three dimensional epitopes (Stijlemans et al. 2004; De Genst et al. 2006), Nbs binding short peptides or linear epitopes have also been reported (Braun et al. 2016; Traenkle et al. 2020; Götzke et al. 2019).

1.7 Selection of antigen specific Nbs

Target specific Nbs can be selected from sources such as naïve, immune and synthetic libraries. Most often favoured are immune libraries generated from camelid immunization. The animal is immunized until an adaptive immune reaction occurs. Blood is taken from the animal, from which lymphocytes are extracted. Using mRNAs obtained from the lymphocytes, the animal's immune gene repertoire is transcribed into cDNA from which Nb genes are amplified by PCRs resulting in a Nb library.

Various molecular display methods have been applied for the selection of specific Nbs from libraries namely phage, yeast, *E.coli*, ribosome, cDNA and mammalian display (Liu et al. 2018; Suzuki et al. 2018) of which phage display is the most used (Arbabi Ghahroudi et al. 1997; Li et al. 2017).

Phage display technology was first described by George Smith as a method for presenting proteins on the surface of lysogenic filamentous bacteriophages (Smith 1985). The applicability of phage display is based on the direct linkage between phage phenotype and genotype (Conrad and Scheller 2005). The coding sequence of the protein to be displayed is fused to a phage coat protein such as the pIII protein and inserted into a phagemid vector . The effective selection of high affinity Nbs using phage display requires a well-constructed Nb phage library and immunoselection conditions. Nb-phage libraries are created by cloning the Nb gene library into phagemid vectors. Biopanning, also known as immunoselection, is the process of selecting specific binders from the phage library. It is based on the repeated cycles of incubation, washing, amplification and reselection of bound phages (Coomber 2002). During biopanning, the target antigen is presented using various methods and several rounds of binding and elution are carried out to enrich phages with the desired binding activity (Tikunova and Morozova 2009). In addition to its robustness, an advantage of phage display is that a wide variety of specific binders can be obtained in a short period of time(Tikunova and Morozova 2009).

The Nb selection process proceeds with the detailed characterization of each Nb candidate to ascertain its affinity, stability and functionality under the desired application conditions.

1.8 Nbs as advanced research tools for versatile biomedical research.

Nbs have emerged as attractive alternatives to conventional antibodies in many areas of biomedical research. Due to their small size, compact structure, solubility and stability, Nbs are conferred with benefits for *in vitro* and intracellular applications (Muyldermans et al. 2009; Muyldermans 2013; Virant et al. 2018; Asaadi et al. 2021; De Meyer et al. 2014). Their ability to bind to and stabilize protein complexes and receptor conformations have positioned them as useful tools in protein structural studies using X-ray crystallography (Pardon et al. 2014) and cryo-EM (Sigoillot et al. 2019; Mukherjee et al. 2020). Moreover, the stability of Nbs especially make them amenable to modification without losing their functionality (Gettemans and De Dobbelaer 2021). The coupling of Nbs with fluorescent dyes, protein domains, oligonucleotides, small molecules, and other moieties have enabled their application in diverse research areas.

As an alternative to conventional antibodies, Nbs have been used to study protein-protein interactions through immunoprecipitations and affinity-purification mass spectrometry (AP-MS) (Beghein and Gettemans 2017). The covalent immobilization of Nbs to solid matrices like agarose, magnetic beads and polystyrene surfaces have yielded tools, also known as nanotraps, applicable for the affinity-based purification of both endogenous and recombinant targets (Rothbauer et al. 2008; Fagbadebo et al. 2022; Traenkle et al. 2020; Klooster et al. 2007). In addition to nanotraps used for IPs, Nbs have been applied in AP-MS studies using BioID proximity labelling, where the target-specific, intracellularly functional Nb is coupled to the promiscuous biotin ligase, BirA, resulting in biotinylation of proximal interacting partners of the target. These biotinylated proteins are then analyzed by streptavidin-based AP-MS (Roux et al. 2012; Beghein and Gettemans 2017).

The small size of Nbs have also contributed to their suitability as affinity detection reagents in super resolution microscopy. The improved resolution of organellar structures after staining with fluorophore conjugated Nbs compared with indirect labelling with conventional antibodies in single molecule and high-resolution microscopy have been well reported (Ries et al. 2012; Virant et al. 2018; Mikhaylova et al. 2015; Pleiner et al. 2015).

In recent years, Nbs have emerged as ideal candidates for *in vivo* imaging. High affinity Nbs targeting disease biomarkers, coupled to radionuclides ^{99m}Tc or ^{111}In have been utilized for SPECT imaging in mice (Chakravarty et al. 2014; De Vos et al. 2014). Nb-based tracers are also being applied for the PET imaging of tumours. PET tracers coupled to Nbs targeting tumour biomarkers such as the human epidermal growth factors, HER2 and HER3, CD20, and epidermal growth factor EGFR showed specific accumulation in the tumour microenvironment

(Vosjan et al. 2011; Xavier et al. 2013; Krasniqi et al. 2017; Warnders et al. 2017). A PET tracer, ^{68}Ga-labelled HER2 Nb is currently undergoing phase II clinical trials for the non-invasive visualization of HER2 expression in primary lesions and metastases (Harmand et al. 2021).

Some Nbs which do not have additional disulfide bonds can retain their antigen-binding properties in the reducing environment of the cytosol (Traenkle and Rothbauer 2017). These intracellularly functional Nbs, termed intrabodies, are therefore candidates for visualization and modulation of their endogenous antigens. Target specific Nbs can be genetically fused to fluorescent proteins, resulting in chimeric constructs termed chromobodies (Cbs) and introduced as DNA-encoded expression constructs in living cells (Rothbauer et al. 2006). Cbs have been applied in the targeting and tracing of their antigen in living cells and in whole organisms (Rothbauer et al. 2006; Schornack et al. 2009; Panza et al. 2015). With these tools, the visualization of antigens in different subcellular compartments has been achieved. The intracellular expression of a Cb specific for the nuclear localized protein, PCNA, enabled real time visualization of endogenous PCNA(Burgess et al. 2012) and was used to investigate compounds which may influence cell cycle progression (Schorpp et al. 2016). Cbs have been applied to monitor dynamic changes of cytoskeletal components including lamin (Rothbauer et al. 2006; Zolghadr et al. 2012), actin (Panza et al. 2015) and vimentin (Maier et al. 2015). The interactions and dynamics of cytosolic proteins such as the GTPase, Dynamin (Galli et al. 2017), RhoA/B (Keller et al. 2019), huntingtin (Maiuri et al. 2017) have also been studied using Cbs. As a result of their stoichiometric binding, Cbs have been presented as useful biosensors of changes in endogenous antigen concentration which could enable deeper understanding of protein regulation during cell signalling and differentiation (Keller et al. 2018).

The fusion of intracellularly functional Nbs with protein domains have generated tools which are applicable for the modulation of their respective antigens. Chimeric Nb fusion proteins have led to the glycosylation (Ramirez et al. 2020), relocalization(Steels et al. 2018) and destruction (Cheloha et al. 2020) of their targets on binding. The selected proteasomal degradation of intracellular proteins has been achieved using artificial Nb-based E3 ubiquitin ligase systems. In the deGradFP approach, an anti-GFP Nb fused with the Fbox protein subunit of the Skp1-Cul1-Fbox (SCF) E3 ligase complex have been used to mediate the knockout of GFP-tagged antigens in *Drosophila*, zebrafish, and mammalian cells (Caussinus et al. 2011). The degradation of nuclear localized antigens using target specific Nb-Fbox protein fusions have been recently reported (Moutel et al. 2016; Bery et al. 2019). A synthetic E3 ubiquitin ligase SPOP, was designed to overcome the limitations of the deGradFP system. It was shown that inducible expression of the anti-GFP Nb fused with SPOP effected the depletion of nuclear

localized GFP-tagged H2B more rapidly than RNAi mediated gene silencing (Ju Shin et al. 2015). Recently, a Nb-based TRIMbody-Away technique was applied for the acute and inducible depletion of eGFP in HEK293T cells (Chen et al. 2021). This technique utilized fusion with the RBCC motif of the TRIM21 protein, a rapid acting E3 ubiquitin ligase utilized fusion with the TRIM21 protein, a rapid acting E3 ubiquitin ligase and Fc receptor involved in the intracellular immune response. The use of a Nb-fusion in the TRIMbody-Away technique ensured intracellular functionality which was a challenge in the original described IgG-based TRIMaway technology (Clift et al. 2018).

As briefly summarized here, the versatility and applicability of Nbs in different formats and constructs, illustrates their potential as novel, reliable tools that can be applied to address various research questions.

1.9 Aims and objectives of this study

Mitochondrial transport and dynamics are vital processes for the maintenance of cellular homeostasis. Dysregulation of these processes is a hallmark of many pathophysiological conditions, particularly neurodegenerative diseases. Miro1 dysfunction in mitophagy has recently been linked to PD, however detailed knowledge of its molecular functionality is severely lacking. Though DRP1 has been studied to an extent, detailed information about its functional significance in apoptosis is needed. The paucity of specific tools to shed light on the functionality of Miro1 and DRP1 may be limiting factors in the understanding of their involvement in different mitochondrial processes and malfunctions.

So far, Miro1 and DRP1 have been studied using affinity reagents like conventional antibodies, through ectopic expression as fluorescent or epitope-tagged fusion proteins, and stably expressed as knock-in mutants. However, to overcome the existing limitations of these methods, versatile tools are needed to study these proteins in relevant research contexts.

The goal of this project is, therefore, the generation and application of nanobodies and chromobodies as novel tools to elucidate the localization, organization, and dynamics of Miro1 and DRP1. The first step in the accomplishment of this objective entailed recombinant expression of the target antigens and subsequent immunization of alpacas. Next, target specific nanobodies were selected from nanobody libraries generated from the alpacas' immune repertoire. This was followed by detailed biochemical and intracellular characterization, functionalization, and optimization of the nanobodies and finally, their utilization for biochemical and cell biological applications.

2 MATERIALS AND METHODS

2.1 Materials

2.1.1 Chemicals, media, and solutions

Chemicals/ Media/ solutions	Manufacturer
2-Propanol	Carl Roth GmbH & Co. KG, Karlsruhe, Germany
2YT media	Carl Roth GmbH & Co. KG, Karlsruhe, Germany
3,3',5,5' Tetramethylbenzidine (TMB)	Carl Roth GmbH & Co. KG, Karlsruhe, Germany
5X Q5 High Fidelity Reaction buffer	New England Biolabs GmbH, Frankfurt, Germany
5x Q5 High GC Enhancer	New England Biolabs GmbH, Frankfurt, Germany
6x DNA Loading Dye	Thermo Fisher Scientific GmbH, Schwerte, Germany
10x Cutsmart® buffer	New England Biolabs GmbH, Frankfurt, Germany
Acetic Acid, 99-100%	Carl Roth GmbH & Co. KG, Karlsruhe, Germany
Acetone	Carl Roth GmbH & Co. KG, Karlsruhe, Germany
Acrylamide/Bisacrylamide	Carl Roth GmbH & Co. KG, Karlsruhe, Germany
Agarose, molecular biology grade	Carl Roth GmbH & Co. KG, Karlsruhe, Germany
Ammonium persulfate (APS)	Carl Roth GmbH & Co. KG, Karlsruhe, Germany
Ampicillin	AppliChem GmbH, Darmstadt, Germany
ATTO dyes (NHS Ester)	ATTO-TEC GmbH, Siegen, Germany
BSA	Sigma-Aldrich Chemie Gmbh, Munich, Germany
Coomassie Instant Blue	Abcam, Cambridge, United Kingdom
DAPI (4,6-diamiddino-2-phenylindole)	Roche Diagnostics GmbH, Mannheim, Germany
DBCO-Agarose beads	Jena Bioscience, Jena, Germany
DBCO conjugated AlexaFluor-647	Intavis Peptide Services GmbH, Tuebingen, Germany
DMEM, high glucose, with phenol red	Thermo Fisher Scientific, Schwerte, Germany
DMSO ≥99 %	Carl Roth GmbH & Co. KG, Karlsruhe, Germany
DNAse I	Applichem GmbH, Darmstadt, Germany
dNTP Solution Mix	New England Biolabs, Frankfurt, Germany
Ethanol, absolute grade	Sigma-Aldrich Chemie GmbH, Munich, Germany

Ethanol, denatured	Carl Roth GmbH & Co. KG, Karlsruhe, Germany
Ethidiumbromide solution (0.025%)	Carl Roth GmbH & Co. KG, Karlsruhe, Germany
Ethylene diamine tetraacetic acid (EDTA)	Applichem GmbH, Darmstadt, Germany
Fetal Bovine Serum (FBS)	Thermo Fisher Scientific, Schwerte, Germany
Formaldehyde (37%)	Applichem GmbH, Darmstadt, Germany
Gibson Assembly® Master Mix	New England Biolabs, Frankfurt, Germany
Glucose D(+)	Carl Roth GmbH & Co. KG, Karlsruhe, Germany
Glycine	Carl Roth GmbH & Co. KG, Karlsruhe, Germany
NEB HiFi DNA Assembly Master Mix	New England Biolabs, Frankfurt, Germany
Hoechst33258	Thermo Fisher Scientific, Schwerte, Germany
Hydrochloric acid 37%	AppliChem GmbH, Darmstadt, Germany
Hyperphage (M13K07ΔpIII)	Progen Biotechnik GmbH, Heidelberg, Germany
Imidazole >99%	Carl Roth GmbH & Co. KG, Karlsruhe, Germany
Isopropyl-beta-D-thiogalactopyranoside (IPTG)	Diagonal GmbH, Münster, Germany
Kanamycin	Carl Roth GmbH & Co. KG, Karlsruhe, Germany
L-Glutamine	Thermo Fisher Scientific, Schwerte, Germany
LB media	Carl Roth GmbH & Co. KG, Karlsruhe, Germany
Lipofectamine 2000	Thermo Fisher Scientific, Schwerte, Germany
Lysozyme	AppliChem GmbH, Darmstadt, Germany
Magnesium chloride	Sigma-Aldrich Chemie Gmbh, Munich, Germany
Methanol, min. 99 %	Sigma-Aldrich Chemie GmbH, Munich, Germany
Milk powder, blotting grade	Carl Roth GmbH & Co. KG, Karlsruhe, Germany
N′-tetramethylethylenediamine (TEMED)	Carl Roth GmbH & Co. KG, Karlsruhe, Germany
NEB-Buffers 1-4	New England Biolabs, Frankfurt, Germany
NHS-activated Sepharose™ 4 Fast Flow	GE Healthcare, Uppsala, Sweden
NP-40	Carl Roth GmbH & Co. KG, Karlsruhe, Germany
NucleoSpin Gel and PCR Clean-up	Macherey-Nagel, Düren Germany
NucleoSpin Plasmid Kit	Macherey-Nagel, Düren Germany
Nuclease-free water	New England Biolabs, Frankfurt, Germany

Opti-MEM, reduced serum media	Thermo Fisher Scientific, Schwerte, Germany
PageRuler™ Plus Prestained Protein Ladder	Thermo Fisher Scientific, Schwerte, Germany
Penicillin Streptomycin	Thermo Fisher Scientific, Schwerte, Germany
Phenylmethanesulfonylfluoride (PMSF)	SERVA Electrophoresis GmbH, Heidelberg, Germany
Phosphate Buffered Saline (PBS),1x	Thermo Fisher Scientific, Schwerte, Germany
Pierce™ BCA Protein Assay Kit	Thermo Fisher Scientific, Schwerte, Germany
Polyethyleneimine	Sigma-Aldrich Chemie GmbH, Munich, Germany
Ponceau S	Sigma-Aldrich Chemie Gmbh, Munich, Germany
Protease Inhibitor Mix B and Mix M	SERVA Electrophoresis GmbH, Heidelberg, Germany
Protein A/G beads	Cytiva GmbH, Freiburg, Germany
Q5® High GC Enhancer	New England Biolabs, Frankfurt, Germany
Q5® Hot Start™ High Fidelity DNA Polymerase	New England Biolabs, Frankfurt, Germany
Q5®Site-Directed Mutagenesis Kit	New England Biolabs, Frankfurt, Germany
Qiagen Plasmid MidiPrep Kit	Qiagen, Hilden, Germany
Restriction enzymes	New England Biolabs, Frankfurt, Germany
SOC medium	New England Biolabs, Frankfurt, Germany
Sodium carbonate	Sigma-Aldrich Chemie GmbH, Steinheim, Germany
Sodium chloride	Carl Roth GmbH & Co. KG, Karlsruhe, Germany
Sodium dodecyl sulfate (SDS)	Carl Roth GmbH & Co. KG, Karlsruhe, Germany
Sulfuric acid, 96 %	Carl Roth GmbH & Co. KG, Karlsruhe, Germany
T4 Ligation kit	New England Biolabs, Frankfurt, Germany
Terrific Broth Medium	Carl Roth GmbH & Co. KG, Karlsruhe, Germany
Triethylamine (TEA)	Carl Roth GmbH & Co. KG, Karlsruhe, Germany
Tris (trisaminomethane)	Carl Roth GmbH & Co. KG, Karlsruhe, Germany
Triton X-100	Carl Roth GmbH & Co.KG, Karlsruhe, Germany
Trypsin-EDTA (0.25%), with phenol red	Thermo Fisher Scientific, Schwerte, Germany
Tween 20	Carl Roth GmbH & Co.KG, Karlsruhe, Germany
β-Mercaptoethanol	Carl Roth GmbH & Co. KG, Karlsruhe, Germany

2.1.2 Devices

Device	Manufacturer
ÄKTA system	GE Healthcare, Uppsala, Sweden
Axiovert 200M Microscope	Zeiss AG, Oberkochen, Germany
Cell Observer SD	Zeiss AG, Oberkochen, Germany
Centrifuge 5424R	Eppendorf AG, Hamburg, Germany
Centrifuge 5810R	Eppendorf AG, Hamburg, Germany
Centrifuge	Eppendorf AG, Hamburg, Germany
Centrifuge Megafuge 1.0R	Heraeus Instruments, Hanau, Germany
CO_2 Incubator CB150	Binder GmbH, Tuttlingen, Germany
Electrophoresis chamber	Bio-Rad Laboratories GmbH, Munich, Germany
GFL water bath 1002	GFL, Burgwedel, Germany
GFL water bath 1083	GFL, Burgwedel, Germany
High-content microscope MetaXpressXL system	Molecular devices, Biberach, Germany
ImageXpress™ Micro Confocal High Content Screening system	Molecular devices, Biberach, Germany
Incubator shaker C25	New Brunswick Scientific, Nürtingen, Germany
INTAS UV documentation system	INTAS, Göttingen, Germany
Light microscope TMS-F	Nikon, Duesseldorf, Germany
Magnet stirrer RCT basic	IKA-Werke GmbH, Staufen, Germany
Multipipette plus	Eppendorf AG, Hamburg, Germany
Neubauer chamber	Brand, Wertheim, Germany
Octet RED96E system	Sartorius AG, Göttingen, Germany
Overhead rotator	Bachofer, Reutlingen, Germany
PCR cycler Biometra TOne	Analytik Jena GmbH, Jena, Germany
pH meter	Mettler-Toledo GmbH, Giessen, Germany
PHERAstar plate reader	BMG Labtech, Offenburg, Germany

Photometer	Eppendorf AG, Hamburg, Germany
Pipette HandyStep	Brand GmbH & Co KG, Wertheim, Germany
Pipets 10 µl, 20 µl, 100 µl, 200 µl, 1000 µl	Brand GmbH & Co KG, Wertheim, Germany
Pipettboy	Integra BioSciences, Fernwald, Germany
Plate-Incubator	Heraeus Instruments
PowerPac Basic Power Supply	Bio-Rad Laboratories GmbH, Munich, Germany
Prometheus NT.48	NanoTemper Technologies. Munich, Germany
Semi-dry transfer cell	Bio-Rad Laboratories GmbH, Munich, Germany
Sonifier Sonopulse HD60/UW60	Bandelin, Berlin, Germany
Spectrometer NanoDrop 2000	Thermo Scientific, Schwerte, Germany
Sterile hood	BDK GmbH, Sonnenbühl-Genkingen, Germany
Thermomixer comfort	Eppendorf AG, Hamburg, Germany
Typhoon TRIO Scanner	GE Healthcare, Uppsala, Sweden
Vortex Genie 2	Scientific Industries, Karlsruhe, Germany

2.1.3 Consumables

Consumables	**Manufacturer**
µClear 96-well microplate	Greiner Bio-One, Frickenhausen, Germany
96 well assay block	Thermo Scientific GmbH, Schwerte, Germany
Amersham Protan 0.45 µm Nitrocellulose	GE Healthcare, Uppsala, Sweden
Amicon® Ultra Centrifugal Filter Devices	Merck Chemicals GmbH, Darmstadt, Germany
Cell Culture Flasks T-25, T-75, T-125	Corning GmbH, Wiesbaden, Germany
Cell Culture Plates, p100	Corning GmbH, Wiesbaden, Germany
Cuvettes	Eppendorf AG, Hamburg, Germany
Falcon Tubes (15 and 50 ml)	Sarstedt AG & Co., Nümbrecht, Germany

Falcon-Tubes 15ml und 50ml	Greiner Bio-One, Frickenhausen, Germany
Filtropur S 0.45	Sarstedt AG & Co., Nümbrecht, Germany
Filtropur S 0.2	Sarstedt AG & Co., Nümbrecht, Germany
GeBAflex Midi Dialysis tubes	Scienova GmbH, Jena, Germany
GFP-Trap Multiwell plate	ChromoTek GmbH, Martinsried, Germany
GFP-Trap Agarose	ChromoTek GmbH, Martinsried, Germany
RFP-Trap	ChromoTek GmbH, Martinsried, Germany
HisTrap™ FF column 1 ml	GE Healthcare, Uppsala, Sweden
LoBind tubes	Eppendorf, Hamburg, Germany
Multiwell plate: 6, 12, 24, 96 well, (sterile)	Corning GmbH, Wiesbaden, Germany
NHS-activated Sepharose 4 Fast Flow	GE Healthcare, Uppsala, Sweden
Parafilm	Brand GmbH & Co. KG, Wertheim, Germany
PCR-Reaction tube, 200 µl/500 µl	Sarstedt AG & Co., Nümbrecht, Germany
Petri-dish, 145 x 20 mm	Greiner Bio-one, Frickenhausen, Germany
Petri-dish, 92 x 16 mm	Sarstedt AG & Co., Nümbrecht, Germany
pH Indicator strips, pH 0-14	Merck KGaA, Darmstadt, Germany
Pipettes (2, 5, 10 und 25 ml)	Sarstedt AG & Co., Nümbrecht, Germany
Pipette tips (10, 20, 200, 1000, 1250 µl)	Starlab GmbH, Hamburg, Germany
Reaction tube 1,5 ml / 2 ml (sterile)	Sarstedt AG & Co., Nümbrecht, Germany
Superdex 75 10/300 GL	GE Healthcare, Uppsala, Sweden
Hi Load® 26/600 Superdex 200pg column	Cytiva Europe GmbH, Freiburg, Germany
syringe (2, 5, 10, 20, 50 ml)	B. Braun Melsungen AG, Melsungen, Germany
TALON Superflow beads	Cytiva Europe GmbH, Freiburg, Germany
Zeba-spin desalting columns	Thermo Fisher Scientific, Schwerte, Germany

2.1.4 Antibodies

Antibodies (species)	Dilution factor	Manufacturer
Anti-DRP1 (clone D6C7; rabbit, mAb)	1000	Cell Signaling, Frankfurt, Germany
anti-GAPDH (rabbit, pAb)	1000	Santa Cruz, Dallas, USA
anti-GFP (clone 3H9; rat, mAb)	250	ChromoTek, Munich, Germany
anti-M13 (mouse, mAb), HRP conjugate	2000	GE Healthcare, Uppsala, Sweden
Anti-His_6	250	GE Healthcare, Uppsala, Sweden
anti-Penta His (mouse, mAb)	1000	Qiagen, Hilden, Germany
anti-Miro1 (clone 4H4; mouse, mAb)	500	Sigma-Aldrich Chemie GmbH, Munich, Germany
anti-Miro1 (rabbit, pAb)	300	Bio-Techne GmbH, Wiesbaden, Germany
anti-Miro1 (rabbit, pAb)	2.5 µg for IP	Thermo Fisher Scientific, Schwerte, Germany
anti-RFP (clone 3F5; mouse, mAb)	250	ChromoTek, Munich, Germany
anti-TagRFP (clone AB233; rabbit, mAb)	1000	Evrogen, Moscow, Russia
Anti-VHH (goat, pAb), Cyanine Cy™5 conjugate	500	Jackson ImmunoResearch, Ely, United Kingdom
Anti-VHH (goat, pAb) FITC conjugate	500	Jackson ImmunoResearch, Ely, United Kingdom
Anti-VHH (goat, pAb), HRP conjugate	5000	Jackson ImmunoResearch, Ely, United Kingdom
Secondary antibodies		
anti-mouse (donkey) Alexa 488/546/647 conjugates	2000	Thermo Fisher Scientific, Schwerte, Germany
anti-rabbit (donkey) Alexa 488/546/647 conjugates	2000	Thermo Fisher Scientific, Schwerte, Germany
anti-rat (donkey) Alexa 488/546/647 conjugates	2000	Thermo Fisher Scientific, Schwerte, Germany

2.1.5 Oligonucleotides

The following oligonucleotides were used in this study for polymerase chain reactions. They were all synthesized by Integrated DNA Technologies (Leuven, Belgium)

Name	Sequence (5´- 3´)
CALL001	GTCCTGGCTGCTCTTCTACAAGG
CALL002	GGTACGTGCTGTTGAACTGTTCC
FR1-1	CATGGCNSANGTGCAGCTGGTGGANTCNGGNGG
FR1-2	CATGGCNSANGTGCAGCTGCAGGANTCNGGNGG
FR1-3	CATGGCNSANGTGCAGCTGGTGGANAGYGGNGG
FR1-4	CATGGCNSANGTGCAGCTGCAGGANAGYGGNGG
FR1-ext1	GTAGGCCCAGCCGGCCATGGCNSANGTGCAGCTGGTGG
FR1-ext2	GTAGGCCCAGCCGGCCATGGCNSANGTGCAGCTGCAGGA
FR4-1	GATGCGGCCGCNGANGANACGGTGACCNGNRYNCC
FR4-2	GATGCGGCCGCNGANGANACGGTGACCNGNGANCC
FR4-3	GATGCGGCCGCNGANGANACGGTGACCNGRCTNCC
FR4-4	GATGCGGCCGCRCTNGANACGGTGACCNGNRYNCC
FR4-5	GATGCGGCCGCRCTNGANACGGTGACCNGNGANCC
FR4-6	GATGCGGCCGCRCTNGANACGGTGACCNGRCTNCC
NB-uni-for	ATATATCTGCAGGAGTCTGGGGGAGGCTTGGTGCA
NB-uni-rev	ATATATTCCGGAGGAGACGGTGACCTGGGTCCC
M13rev (-29)	CAGGAAACAGCTATGACC
Adaptor-phagemid-for	ACACTCTTTCCCTACACGACGCTCTTCCGATCTGGATTGTTATTACTCGCGGCC
Adaptor-phagemid-rev	GACTGGAGTTCAGACGTGTGCTCTTCCGATCTGATCAGCTTCTGTTCTGCGGC
NEW PK/FF-for	GGGAGATCTCCGGCCATGGCNSADGTGCAGCTG
NEW PK/FF-rev	GGGAAGCTTTCTGAGGAGACGGTGACCNG
p4-NMI_for	TGACCATGATTACGCCAAGC
p4-NMI_rev	TCCACAGACAGCCCTCATAGTTA
bivM114GA_for	GCCGGCGTGCACTCTGAGGTACAGCTGCAGGAGTCGGG
nterm1273_rev	CACCACCGCCAGATCCACCGCCACCTGATCCTCCGCCTCCGCTGCTAACGGTGACC
bivM114GA2_for	GGTGGATCTGGCGGTGGTGGAAGTGGTGGCGGAGGTAGTGAGGTACAGCTGCAGGAGTCGGG

downEcoRI_rev	GTTGTAAAACGACGGCCAGTG
bivM114FPCR_for	GTCTGTGACCGCCGGCGTGCACTCTGAG
bivM114FPCR_rev	TTTAATTAAGCGGCCGCGAATTGTTGTAAAACGACGGCCAGTG
Miro1fragB_rev	CAAGCTCTTCAGCAATATCACGG
Miro1fragA_for	CGTGTGGATACATGGCCATTGTTGTCAATTTAACAAAGA
Miro1fragA_rev	TGGTGGCGGAGGTAGCATGAAGAAAGACGTGCGGATC
vectorGA_for	TGGCTACCCGTGATATTGCTG
vectorGA_rev	CGTCTTTCTTCATGCTACCTCCGCCACCACTTC
nGTP_for	ATTGGTACCTTTTGGCTTCGAGCAAGTTTTGG
nGTP_rev	ATTGGTACCCTCCTTCTCCTCTGGGC
nGTPEF2_rev	GCGGGTACCATTTCTTTGAGTTTGTTTTTTCTGCAGG
Delta nGTP_for	ATTGGTACCGAGGAGAAGGAGATGAAACCAGC
Delta nGTP_rev	GCTGGTACCCATGCTACCTCCGCCACC
cGTP_for	AAAAAACAAACTCAAAGAAATGTGTTCAGATG
cGTP_rev	CATGCTACCTCCGCCACCACTTCC
NM95_for	TAATCTAGAGGGCCCTATTCTATAGTG
NM95_rev	GCTGGAGACGGTGACCTG
frag2IRES_for	CCCAGGTCACCGTCTCCAGCTAACTAGAGGTTAACGAATTC
frag2IRES_rev	GGTTGTGGCCATATTATC
nls-insert_for	AAGAAGAGGAAGGTTTGAGCGGCCGCGACTCTA
nls-insert_rev	CTTAGGGCTGCCTCCATTAAGTTTGTGCCCCAGTTTGCTAG
frag3-tRFP-nls_for	ATGATAATATGGCCACAACCATGGTGTCTAAGGGCGAAG
frag3-tRFP-nls_rev	GAATAGGGCCCTCTAGATTAAACCTTCCTCTTCTTCTTAGG
NM1007backbone-for	TGAGGATCCACCGGATCTAG
NM1007backbone-rev	CATGCTACCTCCGCCACC
DRP1-GTPase-for	GTGGTGGCGGAGGTAGCATGGAGGCGCTAATTCCTGTC
DRP1-GTPase-rev	CTAGATCCGGTGGATCCTCATTGGAGTAAAGTAGCACTTTTATC
DRP1-C-term-rev	CTAGATCCGGTGGATCCTCACCAAAGATGAGTCTCCCG
DRP1-VD-rev	CTAGATCCGGTGGATCCTCATTTTCGTGCAACAGGAAC
DRP1-MD-rev	CTAGATCCGGTGGATCCTCAAAAGTCTGGATGTTTTGTG
DRP1-GED-for	CGAAAACTATCTGCTCGGGAAC

2.1.6 Expression constructs

Constructs	Origin
Miro1(nGTPase-EF1-EF2)-His_6	Plasmid provided by Natascha Bartlick
Miro1-V5 HisA	Plasmid provided by Julia Fitzgerald
GFP-Miro1	this study
pEGFP-N1	Clontech
GFP-Miro1(nGTPase)	This study
GFP-Miro1(nGTPase-EF1-EF2)	This study
GFP-Miro1(EF1-EF2-cGTPase)	This study
GFP-Miro1 (cGTPase)	This study
AcGFP-DRP1	Plasmid provided by Andreas Jenner
GFP-DRP1	This study
GFP-DRP1 (GTPase-MD-VD)	This study
GFP-DRP1 (GTPase-MD)	This study
GFP-DRP1 (GTPase)	This study
GFP-DRP1 (GED)	This study
pHEN4	(Arbabi Ghahroudi et al. 1997)
pHEN6	(Rothbauer et al. 2008)
pHEN6_Nb constructs	This study
pCDNA3.4	Addgene
bivM41-Nb	This study
bivM114-Nb	This study
pTagRFP	(Panza et al. 2015)
All Cbs	This study
pCDNA3_NSlmb-vhhGFP4	(Caussinus et al. 2011)
Fbox-PEPNb	This study
Fbox-GBP-IRES-$TagRFP_{NLS}$	This study
Fbox-M41-IRES-$TagRFP_{NLS}$	This study
Fbox-M114-IRES-$TagRFP_{NLS}$	This study

2.1.7 Bacterial strains

Cell lines	Additional information	Obtained from
E. coli XL1	Chemically competent	Agilent Technologies GmbH, Waldbronn, Germany
E.coli INV110	Chemically competent	Thermo Fisher Scientific, Schwerte, Germany
E.coli BL21	Chemically competent	Thermo Fisher Scientific, Schwerte, Germany
E.coli TG1	Electroporation competent	Agilent Technologies GmbH, Waldbronn, Germany

2.1.8 Mammalian cell lines

Cell lines	Additional information	Obtained from
HeLa Kyoto	Cellosaurus no. CVCL_1922 human cervix adenocarcinoma	Kyoto University, Japan
HEK293	CRL-3216 human embryonic kidney cells	ATCC
U2OS	HTB-96 human bone osteosarcoma cells	ATCC
HAP1	C631 Chronic Myelogenous Leukaemia cells	Horizon Discovery, UK
ExpiCHO™	A29127 subclone of CHO-S Chinese hamster ovary (CHO) cells	Thermo Fisher Scientific

2.2 Methods

2.2.1 Molecular biology methods

2.2.1.1 Polymerase chain reactions

To amplify DNA fragments and to introduce specific restriction sites, polymerase chain reaction (PCR) was performed. The standard PCR set-up contained the following components: (1) template DNA, (2) forward and reverse DNA primers (listed under oligonucleotides in subheading 2.1.5) (3) a thermostable DNA polymerase, (4) deoxynucleotide triphosphates (dNTPs) mix, (5) reaction buffer and optionally, (6) High GC Enhancer (**Table 1**). The amplification reactions were carried out according to the conditions shown in **Table 2** wherein the annealing temperature was adjusted to the nucleotide composition of the DNA primers and the extension time to the length of the amplicon.

***Table 1**. Standard PCR components*

Component	**Volume**	**Final conc.**
5x Q5®HF buffer	5 µl	1x
dNTP mix (10 mM)	0.5 µl	200 µM
forward primer (10µM)	1 µl	400 nM
reverse primer (10µM)	1 µl	400 nM
Q5® HotStart™ DNA polymerase	0.25 µl	0.01 U/µl
Template DNA (10 ng/µl)	1-2 µl	0.4- 0.8 ng/µl
5x High GC Enhancer	5 µl	1x
Nuclease free dH_2O	to 25 µl	

***Table 2**. Standard PCR cycling steps*

Step	**Temp**	**Time**	**Number of cycles**
Initial denaturation	95 °C	30 s	1
Denaturation	95 °C	10 s	25x
Annealing	53 - 67 °C	20 s	
Extension	72 °C	20 s per kb	
Final extension	72 °C	3 min	1
End	4 °C	∞	

2.2.1.2 Restriction digestion

Digestion of plasmids or amplified DNA fragments was performed using restriction enzymes obtained from New England Biolabs according to the manufacturer's instructions. For analytical purposes and restriction-based cloning, 0.5 - 1 µg and 2 - 5 µg DNA were digested respectively by restriction enzymes.

2.2.1.3 Agarose gel electrophoresis

The analysis and separation of DNA fragments from enzymatic restriction and amplicons from PCR reactions was done by agarose gel electrophoresis. To accomplish this, the DNA probes were mixed with 6X DNA loading dye and separated using 0.9 - 1.5 % agarose dissolved in 1X Tris-acetate-EDTA (TAE) buffer containing 0.025 µg/ml ethidium bromide to allow detection of DNA under UV exposure. As standard Generuler 1 kb Plus DNA Ladder was used. Ethidium bromide-stained DNA was detected with an Intas UV system (Intas Science Imaging). For preparative gels, respective DNA bands were cut out from the gel and purified using the NucleoSpin Gel and PCR clean-up Kit (Macherey-Nagel) according to the manufacturer's instructions.

2.2.1.4 Site-directed mutagenesis

Using site-directed mutagenesis (SDM), targeted mutations such as insertions and deletions were introduced into plasmid DNA. First, primers containing the desired mutation were designed with the NEBase Changer online software (version 1.3.2). In the next step, the primers were used in a PCR (**Table 3.**), resulting in the amplification of the whole plasmid.

***Table 3**. Components of site directed mutagenesis PCR*

Component	**Volume for 25µl reaction**	**Final conc.**
Q5® HotStart™ HF 2x Master Mix	12.5 µl	1x
forward primer (10µM)	1.25 µl	500 nM
reverse primer (10µM)	1.25 µl	500 nM
Template DNA (10 ng/µl)	1 µl	0.4 ng/µl
Nuclease free dH_2O	9 µl	

The amplification by PCR was carried out according to the conditions shown in **Table 4**. The annealing temperature was adjusted based on the nucleotide composition of the DNA primers and the extension time selected based on the length of the amplicon.

Table 4*.Site directed mutagenesis PCR cycling steps*

Step	**Temp**	**Time**	**Number of cycles**
Initial denaturation	98 °C	30 s	1
Denaturation	98 °C	10 s	25x
Annealing	58 - 72 °C	20 s	
Extension	72 °C	30 s per kb	
Final extension	72 °C	5 min	1
End	4 °C	∞	

After the PCR, a kinase, ligase and DpnI (KLD) treatment was carried out for ligation and template removal by DpnI, a methylation-dependent endonuclease (**Table 5**).

Table 5. *KLD reaction components*

Component	**Volume for 10µl reaction**	**Final conc.**
PCR product	2 µl	
2x KLD reaction buffer	5 µl	1x
10x KLD enzyme mix	1 µl	1x
Nuclease free dH_2O	2 µl	

KLD reaction mixture was incubated at room temperature for 30 min and subsequently 5 µl of the mixture was transformed in chemically competent *E. coli*. Enzymes and buffers used for the PCR and KLD treatment were supplied in the Q5® Site Directed Mutagenesis Kit.

2.2.1.5 Gibson assembly cloning

For the generation of the constructs requiring the assembly of multiple DNA fragments, Gibson assembly cloning (Gibson et al. 2009) was used. For the Gibson assembly cloning of GFP-Miro1 and bivM114, amplification primers were designed by Dr Philipp Kaiser (NMI). For other

constructs, amplification primers were designed using the NEBuilder Assembly online software (version 2.5.6). the primers are listed under subheading 2.1.5. DNA insert fragments containing appropriate overlaps were amplified using standard PCR as previously described (**Table 1** and **Table 2**). The linearized vector backbone was generated by a restriction digest or by PCR amplification (listed under section 2.1.6). All fragments were analysed on an agarose gel and purified using the NucleoSpin Gel and PCR Clean-up kit (Macherey-Nagel) according to manufacturer's instruction. Concentrations of all DNA fragments were determined using the NanoDrop™ 2000 spectrometer. Gibson Assembly reactions were set up using NEB™ Gibson assembly or the NEB™ HiFi DNA assembly kit as described in **Table 6** and incubated at 50 °C for 30 to 60 min. Subsequently, 5 µl of the reaction were transformed into chemically competent *E. coli*.

***Table 6**. DNA assembly reaction components*

Component	**Amount for 2-3 fragment assembly (NEB™Gibson assembly kit)**	**Amount for 2-3 fragment assembly (NEB™HiFi DNA assembly kit)**
Vector	50 ng	50 ng
Insert	2 to 3-fold excess	2-fold excess
Total amount of fragments (in *X* µl)	0.02 – 0.5 pmol	0.03 – 0.2 pmol
2× Master Mix	10 µl	10 µl
Nuclease free dH_2O	10-*X* µl	10-*X* µl
Total volume of reaction	20 µl	20 µl

2.2.1.6 DNA ligation

To generate plasmids containing a desired DNA insert and linearized vector backbone, DNA ligation was performed using the NEB™ T4 DNA ligase. Molar ratios used for ligation ranged from 3:1 to 7:1 (insert to vector ratio). For larger insert sizes similar to the size of the digested vector backbone, a ratio of 3:1 was chosen, whereas high molar ratios (7:1) were chosen for small DNA inserts. Ligation reactions (**Table 7**) were incubated at 22°C for 2 h or at 16°C overnight and afterwards the ligase was inactivated at 65°C for 10 min. 5 µl of the reaction was then transformed into chemically competent *E. coli*. To determine the background due to

undigested vector or vector re-circularization, the digested backbone without insert was employed as ligation control.

***Table 7**. DNA ligation reaction components*

Component	10 µl reaction
T4 DNA ligase buffer	1 µl
Vector DNA	100 ng
Insert DNA	3 to 7-fold excess
T4 DNA ligase	1 µl
Nuclease free dH_2O	Up to 10 µl

2.2.1.7 Transformation of bacteria

Chemically competent *E. coli* XL1 blue or *E. coli* INV110 (*dam* and *dcm* methylation negative) or *E.coli* BL21(DE3) were transformed with plasmids in this study. The bacteria were thawed on ice for 10 min and subsequently, 5 µl of the ligation or DNA assembly reaction were added to the cells and mixed by flicking the reaction tube. Cells were continuously incubated on ice for 5 min followed by a heat shock at 42 °C for 40 s. Tubes were again placed on ice for 2 min followed by the addition of 150 µl SOC media (prewarmed to 37 °C) to the bacteria. Tubes were incubated at 37 °C for 60 min with agitation at 600 rpm. After the incubation cells were plated on agar plates with appropriate selection antibiotics and incubated overnight at 37 °C.

2.2.1.8 Plasmid extraction

Transformed *E. coli* were grown overnight at 37 °C in 5 ml LB medium for small scale plasmid preparations (Miniprep) or in 50 ml LB medium for larger DNA amounts (Midiprep)
in the presence of appropriate selection antibiotics. Miniprep DNA extractions were performed with the NucleoSpin® Plasmid kit while high DNA amounts were extracted with Qiagen Plasmid MidiPrep kit following the respective manufacturer's protocol. DNA concentrations were determined by measuring the absorbance at 260 nm using a NanoDrop™ 2000 spectrometer.

2.2.1.9 Generation of expression constructs used in this study

The plasmids used during this study were generated using classical cloning, site-directed mutagenesis, and Gibson assembly methods. A summary of the procedure for the generation of each construct as well as the backbone, inserts, and amplification primers used are described in **Table 8**. The sequences of all generated constructs were confirmed by Sanger sequencing by Eurofins Genomics GmbH, Ebersberg.

***Table 8**. Cloning strategies of expression constructs generated in this study.*

Constructs	Template/backbone	Cloning steps with respective primers
GFP-Miro1	pEGFP-N1	a. Amplification of Miro1 sequence from Miro1-V5 HisA plasmid with primers, Miro1fragA_for/Miro1fragA_rev and Miro1fragB_for/Miro1fragB_rev b. Gibson assembly of amplicon and linearized backbone with primers VectorGA_for /VectorGA_rev
GFP-Miro1(nGTPase)	GFP-Miro1	a. Deletion of EF1-EF2-cGTPase domains by amplification with primers nGTP_for and nGTP_rev. *KpnI/DpnI* digestion of amplicon followed by intramolecular re-ligation
GFP-Miro1(nGTPase-EF1-EF2)	GFP-Miro1	Deletion of cGTPase domain by amplification with primers nGTP_for and nGTPEF2_rev. *KpnI/DpnI* digestion of amplicon followed by intramolecular ligation
GFP-Miro1(EF1-EF2-cGTPase)	GFP-Miro1	Deletion of nGTPase domain by amplification with primers Delta nGTP_for and Delta nGTP_rev. *KpnI/DpnI* digestion of amplicon followed by intramolecular ligation
GFP-Miro1 (cGTPase)	GFP-Miro1	Deletion of nGTPase-EF1-EF2 domains using Q5™ site directed mutagenesis kit with primers cGTP_for and cGTP_rev.
GFP-DRP1	pEGFP-N1	DNA assembly of DRP1 coding sequence amplified from AcGFP-DRP1 construct with primers Drp1-GTPaseFor and Drp1-C-term-rev; and pEGFP-N1 backbone linearized with primers

		NM1007backboneFor and NM1007backboneRev.
GFP-DRP1 (GTPase-MD-VD)	pEGFP-N1	DNA assembly of amplified DRP1 GTPase-Middle-Variable domains from AcGFP-DRP1 construct with primers Drp1-GTPaseFor and Drp1-VD-rev; and pEGFP-N1 backbone linearized with primers NM1007backboneFor and NM1007backboneRev.
GFP-DRP1 (GTPase-MD)	pEGFP-N1	DNA assembly of amplified DRP1 GTPase-Middle domains from AcGFP-DRP1 construct with primers Drp1-GTPaseFor and Drp1-MD-rev; and pEGFP-N1 backbone linearized with primers NM1007backboneFor and NM1007backboneRev.
GFP-DRP1 (GTPase)	pEGFP-N1	DNA assembly of amplified DRP1 GTPase domain from AcGFP-DRP1 construct with primers Drp1-GTPaseFor and Drp1-GTPase-Rev; and pEGFP-N1 backbone linearized with primers NM1007backboneFor and NM1007backboneRev.
GFP-DRP1 (GED)	GFP-DRP1	Deletion of GTPase-Middle-Variable domains from GFP-DRP1 expression construct using Q5™ site directed mutagenesis kit with primers DRP1-GED-for and NM1007backboneRev.
All monovalent nanobodies	pHEN6(C)	restriction cloning from phage display vector, pHEN4 using *SfiI/BstEII* or *NcoI/BstEII*
bivM41-Nb	pCDNA3.4	Restriction cloning from synthesized sequence using *NheI/AgeI* sites and ligation into *XbaI/AgeI* digested pCDNA3.4 vector

bivM114-Nb	pCDNA3.4	I. Amplification of M114 sequence in two separate PCRs with primer sets bivM114GA-for and nterm1273_rev; bivM114GA2_for and downEcoRI_rev; II. overlap-extension PCR to fuse both amplicons using primer set bivM114FPCR_for and bivM114FPCR_rev. III. Gibson assembly cloning of resulting sequence and *Esp3I*- and *EcoRI*- digested pCDNA3.4 expression vector.
All Cbs	pTagRFP	I. PCR amplification of Nb sequences from pHEN6 vectors with primers NEW PK/FF-for and NEW PK/FF-rev. II. Restriction cloning into *BglII/ BstEII* or *BglII/HindIII* sites of the previously described Cb expression vector(Panza et al. 2015).
Fbox-Nb-IRES constructs	pCDNA3_NSlmb-vhhGFP4(Caussinus et al. 2011)	I. PCR amplification of the vector backbone with primers NM95_for and NM95_rev. II. PCR amplification of the IRES sequence, from pcDNA3.1(+)IRES-GFP, with primers frag2IRES_for and frag2IRES_rev. III. (a) insertion of an NLS sequence downstream of the TagRFP sequence in a Cb expression vector with primers nls-insert_for and nls-insert_rev using the Q5 Site-Directed Mutagenesis Kit (NEB). (b) PCR amplification of

		$TagRFP_{NLS}$ sequence with primers frag3-tRFP-nls_for and frag3-tRFP-nls_rev.
	IV.	Gibson assembly of all fragments with NEBuilder HiFi DNA assembly

2.2.2 Biochemical methods

2.2.2.1 Expression of recombinant proteins

In this project, Miro1(aa 1-290), monovalent Miro1 and DRP1-Nbs were expressed in *E.coli* under the control of the lac-promoter. Bivalent Miro1-Nbs were expressed in ExpiCHO™ cells according to the manufacturer's protocol.

For bacterial protein expression, bacteria from frozen glycerol stocks or colonies from agar plates were scraped with a sterile pipet tip and suspended into 50 ml of LB medium supplemented with respective antibiotic. The culture was grown overnight at 37 °C with shaking at 130 rpm. The next day, the cultures were spun down, and the resulting pellet resuspended in 1L Terrific Broth (TB) medium. The cultures were grown at 37°C, 120 rpm in baffled Erlenmeyer flasks with a capacity of four or five litres. OD_{600} was monitored using photometer in disposable plastic cuvettes. When OD_{600} was >1, protein expression was induced by adding IPTG to a final concentration of 1 mM. IPTG is a structural analog of lactose that permanently binds to the *lacI* repressor and allows constant protein expression of genes controlled by the *lac*-promoter. The cultures were grown overnight at 30°C with shaking at 150 rpm. The next day, OD_{600} values were measured, and the bacteria were harvested by centrifugation at 6000 rpm for 10min at 4°C. The pellets were stored at -20°C or resuspended in binding buffer (for Miro1, 25 mM HEPES, 0.3M NaCl, 1 mM $MgCl_2$, 1 mM DTT and 25 mM Imidazole, pH 7.4; for Nbs, 1xPBS, 0.5M NaCl, 50 mM Imidazole at pH 7.4) for further processing.

2.2.2.2 Preparation of bacterial periplasmic extracts

Nb expression from *E.coli* XL1 cells in 1 ml cultures were carried 12-well plates using the same procedures described in *section 2.2.2.1* above. 16 - 20 h after induction, the bacteria pellets were harvested by centrifugation at 2900 x g for 20 min at 4°C. the pellets were resuspended in 200 µl of precooled TES buffer (0.2 M Tris/HCl (pH 8), 0.5 mM EDTA, 0.5 M sucrose) supplemented with 2 mM PMSF and incubated on a shaker for 20 min, 400rpm at 4°C. 300µl of a 0.25x dilution of TES buffer in sterile ddH_2O was added to each well and incubated under

the same conditions for 30 min. Subsequently, the plate was centrifuged at 2900 x g for 20 min at 4°C and the supernatants stored at 4 °C for further analysis.

2.2.2.3 Bacterial cell lysis

Standard lysis of bacteria was performed in binding buffer containing additional DNaseI (1 µg/ml), phenylmethanesulfonylfluoride (PMSF 1 mM), 1x Protease inhibitor mix B and lysozyme (0.1 mg/ml). Continuous sonication was done for 5 min on ice. Thereafter, incubation for 1 h at 4 °C on an end-over end rotor followed by sonication for 5 min on ice. Finally, insoluble components were separated by centrifugation (20 000 x g, 20 min, 4 °C) and supernatants were filtered through a 0.45 µm filter.

2.2.2.4 Protein purification using affinity chromatography

His_6-tagged proteins were purified from supernatants of bacterial cell lysates or cultures of ExpiCHO™ cells by immobilized Ni^{2+} affinity chromatography (IMAC) using an ÄKTA Pure 25 FPLC system. For all purifications, the sample was applied to the chromatographic system using the sample pump. 1 ml HisTrap™ FF columns were equilibrated in 5 column volumes of binding buffer and a flow rate of 1 ml/min was used for the purification run. Bound proteins were eluted in 0.5 ml fractions by gradual increase of imidazole concentrations from 50 mM to 500 mM.

2.2.2.5 Size exclusion chromatography and desalting.

Size exclusion chromatography was performed using the ÄKTA Pure 25 FPLC system and a Superdex 75 or a Superdex 200pg gel filtration column to further increase the purity of proteins. The flow rate through the chromatographic system was 0.5 ml/min. The column was equilibrated using two column volumes of PBS. Peak fractions of the affinity chromatography eluate were pooled and applied to the column. Fractions of the indicated peaks were collected in 0.5 ml fractions. For buffer exchange and concentration of purified proteins, Amicon™ ultracentrifugation filter devices were used according to the manufacturer's instructions.

2.2.2.6 SDS Page analysis of protein and Western blotting

For the size dependent separation and analysis of proteins, denaturing polyacrylamide gel electrophoresis (SDS-PAGE) was performed. Samples, containing 1x SDS sample buffer (0.1 % β-Mercaptoethanol, 0.0005 % Bromophenol blue, 10 % Glycerol, 2 % SDS in ddH_2O) were

denaturated at 95 °C for 10 min. the probes were loaded on gels which were prepared as shown in **Table 9** and **10.** As standard, PageRuler™ plus prestained protein ladder was used.

Table 9*.SDS separating gel*

Component	Final concentration
Acrylamide	8-15% (v/v)
Tris/HCl, pH 8.8	375 mM
SDS	0.1% (w/v)
APS	0.05% (w/v)
TEMED	0.1% (v/v)

Table 10*. SDS stacking gel*

Component	Final concentration
Acrylamide	5% (v/v)
Tris/HCl, pH 6.8	60 mM
SDS	0.1% (w/v)
APS	0.05% (w/v)
TEMED	0.1% (v/v)

Separation using a BioRad electrophoresis system was performed at 150-200 V in running buffer (25 mM Tris/HCl, 1.92 M glycine in ddH_2O).

Subsequently, separated proteins were either stained with Coomassie or transferred from the SDS-gel to a nitrocellulose membrane by Western blotting. For Coomassie staining, the gel was incubated with gentle agitation in InstantBlue® Coomassie Protein stain for 30 min followed by removal of excessive dye by subsequent washing in ddH_2O.

Proteins were transferred from SDS-gels to nitrocellulose membranes by semi-dry blotting system (BioRad) at 2.5 mA/cm^2 for 1.5 - 2 h. After the run, total protein on membranes was stained reversibly with Ponceau S solution (0.5 % Ponceau S, 10 % acetic acid in ddH_2O). For specific protein detection membranes were incubated overnight at 4 °C with primary antibodies (listed in section 2.1.4), diluted in MTBST (5 % non-fat dry milk in TBST) or in 5 % BSA in TBST according to the manufacturer's guidelines. The next day, membranes were washed 3 times with TBST for 5 min followed by incubation with a fluorescently labelled secondary

antibody diluted in MTBST for 1 - 2 h at room temperature. The membranes were washed thrice with TBST for 5 min and dried at room temperature. fluorescent signals were detected on a Typhoon-Trio laser scanning system (using appropriate excitation and emission filter settings) and analysed with the GE Healthcare ImageQuant™ TL software (version 8.1).

2.2.2.7 Affinity measurements by biolayer interferometry (BLI)

The binding kinetics of Nbs identified in this study were determined using the Octet RED96e system according to the manufacturer's recommendations. Briefly, 2 - 10 µg/ml solution of biotinylated Nbs diluted in Octet buffer (25 mM HEPES, 300 mM NaCl, 1mM $MgCl_2$, 0.1% BSA) was used for 40 s to immobilize the Nb on streptavidin coated biosensor tips (SA, Sartorius). In the association step, a dilution series of corresponding target antigen ranging from 4 nM – 1 µM were reacted for 300 s followed by dissociation in Octet buffer for 720 s. Every run was normalized to a reference run using Octet buffer for association. Data were analysed using the Octet Data Analysis HT 12.0 software applying the 1:1 ligand-binding model and global fitting.

2.2.2.8 NHS-ester functionalization of Nbs

Purified Nbs were immobilized on agarose beads or chemically coupled to dyes through their exposed lysine residues using NHS chemistry as previously described (Rothbauer et al. 2008; Maier et al. 2015; Braun et al. 2016). For the immobilization of Nbs on Sepharose beads to generate nanotraps, 2 mg of purified nanobodies at 1 mg/ml concentration in phosphate-buffered saline were coupled to 1 ml NHS-activated Sepharose according to the manufacturer's protocol.

Coupling of purified Nbs to NHS-activated ATTO647 or Alexa Fluor (AF) 647 dyes was performed according to the manufacturer's protocol. Unbound dye was removed using Zeba™ Spin Desalting columns according to the manufacturer's instructions. Labelled Nbs were stored away from light at 4 °C.

2.2.2.9 Sortase labelling of Nbs

For the site-specific functionalization of Nbs, enzymatic labelling using the sortase catalysed transpeptidation reaction was performed as described (Popp and Ploegh 2011). Sortase A pentamutant (eSrtA) was expressed and purified as described (Chen et al. 2011). The substrate peptide H-Gly-Gly-Gly-propyl-azide (sortase substrate) was custom synthesized by Intavis AG. For sortase labelling, 50 µM Nb, 250 µM sortase substrate peptide dissolved in sortase buffer (50 mM Tris, pH 7.5, and 150 mM NaCl) and 10 µM sortase were mixed in

coupling buffer (sortase buffer with 10 mM $CaCl_2$) and incubated for 4 h at 4°C. Uncoupled Nb and sortase were depleted by IMAC. Unbound excess of unreacted peptide was removed using Zeba™ Spin Desalting Columns. Samples were taken before and after the sortase reaction and IMAC depletion for analysis by SDS-PAGE. For conjugation to fluorophores, the resulting azide-coupled Nbs were then labelled by SPAAC (strain-promoted azide-alkyne cycloaddition) click chemistry reaction with two-fold molar excess of Alexa-Fluor conjugated dibenzocyclooctyne (DBCO-AF_{647}, Jena Bioscience) for 2 h at 25°C. Unclicked DBCO-AF_{647} were removed by dialysis against PBS over 48 h with buffer changes every 4h. The dialysis was performed in Gebaflex Midi dialysis tubes which had a molecular weight cut-off of 8 kDa. Samples taken before and after the click chemistry reaction were analysed by SDS-PAGE according to standard protocol.

For the generation of the bivalent nanotraps, 1 mg of azide coupled Nbs were incubated with 0.5 ml DBCO-Agarose (Jena Bioscience) slurry for 4 h at 25 °C. The beads were centrifuged at 2700 x g for 2 min and the supernatant was removed. Samples of the input and flow through fractions were analysed by SDS-PAGE according to standard protocol. The Nb coupled beads were washed thrice with 2.5 ml PBS and stored in 1 ml PBS.

2.2.2.10 Mammalian cell lysis and protein extraction

Mammalian cells were washed 3 times with 1x PBS and harvested from 100 mm cell culture dishes by centrifugation at 300 x g for 5 min. For the analysis of endogenous Miro1 levels in different cell lines, the cells were harvested after 24 h. Subsequently, cells were washed in PBS (pH 7.4) and harvested, snap-frozen in liquid nitrogen and thawed on ice. Cell pellets were resuspended in 200 µl of RIPA lysis buffer (10mM Tris/HCl pH 7.5, 150mM NaCl, 0.5 mM EDTA, 0.1% SDS, 1% Triton X-100, 0.1% sodium deoxycholate) or 200 µl lysis buffer [50 mM Tris/HCl pH 7.5, 150 mM NaCl, 1 mM EDTA,1 mM PMSF, 1 µg/ml DNaseI, 2.5 mM $MgCl_2$, mammalian protease inhibitor cocktail (Serva)] containing either 0.5% NP40 or 1% Triton X-100. Homogenization was achieved by passing the lysate through needles of decreasing gauge and intermittent vortexing for 60 min on ice. Lysates were centrifuged at 18,000 x g for 15 min at 4°C. Protein concentrations of the soluble fractions were determined using Pierce™ BCA Protein Assay kit (Thermo Fisher Scientific) according to manufacturer's protocol.

2.2.2.11 Immunoprecipitation

3 x 10^6 HEK293 cells were seeded in 100 mm culture dishes and cultivated for 24 h. For the pulldown of endogenous Miro1, cells were harvested and lysed after 24 h. For the pulldown of

exogenous proteins, the cells were subjected to plasmid DNA transfection with equal amounts of expression vectors and cultivated for 24 h. Subsequently, cells were washed in PBS (pH 7.4) and harvested, snap-frozen in liquid nitrogen, stored at -20°C or thawed for immediate use. The cells were homogenized as described in section 2.2.2.10 and the supernatant adjusted with dilution buffer (50 mM Tris/HCl ,150 mM NaCl, 0.5 mM EDTA, 1 mM PMSF) to 500 µl. 5 µl (1%) was added to 2 x SDS-containing sample buffer (60 mM Tris/HCl, 2% (w/v) SDS, 5% (v/v) 2-mercaptoethanol, 10% (v/v) glycerol, 0.02% bromphenol blue; referred to as input). For immunoprecipitation, nanotraps were gently redispersed in storage buffer and 40 – 80 µl were added to Low-bind 1.5 ml Eppendorf tubes. The nanotraps were pelleted and the storage buffer discarded. The nanotraps were washed thrice and equilibrated in 500 µl dilution buffer. Subsequently, the protein solution was added to the nanotraps and incubated overnight on an end over end rotor at 4°C. As a positive control, 2.5 µg of rabbit anti-Miro1 or anti-DRP1 antibody was added to the protein solution and incubated under the same conditions. For pulldown of immunocomplexes, 40 µl of an equilibrated mixture of protein A/G-Sepharose (Amersham Biosciences) were added, and incubation continued for 4 h. As a negative control, a non-related nanotrap (PepNb) was used. After centrifugation (2 min, 2700 x g, 4°C), the supernatant was removed, and the bead pellet was washed three times in 500 µl dilution buffer. On the third wash, the beads were transferred to a pre-cooled 1.5 ml tube (Eppendorf), resuspended in 2 x SDS-containing sample buffer and boiled for 10 min at 95 °C. Samples (1% input, 20% bound) were analysed by SDS-PAGE followed by Western blotting according to standard procedures. Immunoblots were probed with primary antibodies specific for the immunoprecipitated target. In this study, anti-GAPDH antibody was used both as a loading control and as negative control to detect unspecific binding to Miro1 and DRP1 nanotraps.

2.2.2.12 Intracellular Immunoprecipitation

3 x 10^6 HEK293 cells were seeded in 100 mm culture dishes and cultivated for 24 h. The cells were transiently transfected with equal amounts of expression vectors encoding DRP1-Cbs (D7 and D63) or the Pep-Cb. The transfection efficiency was monitored the next day by wide field fluorescence microscopy and cells were harvested 24 h after transfection. Cell pellets were lysed as described in section 2.2.2.10 and chromobodies were precipitated using the RFP-Trap. For each Cb construct, 50 µl of RFP-Trap beads were transferred into a 1.5 ml tube, washed thrice and equilibrated in 500 µl dilution buffer. Subsequently, the different soluble fractions were added to the beads and incubated overnight on an end over end rotor at 4 °C. After centrifugation (2 min, 2700 x g, 4 °C), the supernatant was removed, and the bead pellet was washed three times in 500 µl dilution buffer. On the third wash, the beads were transferred

to a pre-cooled 1.5 ml tube (Eppendorf), resuspended in 2x SDS-containing sample buffer and boiled for 10 min at 95°C. Samples (1% input, 1% non-bound fraction and 20% bound) were analysed by SDS-PAGE followed by Western analysis using appropriate antibodies for detection.

2.2.3 Cell culture methods

2.2.3.1 Culturing of mammalian cell lines.

All cell culture techniques were carried out under sterile conditions on a laminar flow hood. Cryopreserved cells (10 % DMSO in culture medium) were thawed in a 37°C water bath. Cells were transferred into fresh culture medium after centrifugation (100 x g, 5 min), and grown at 37 °C, 5 % CO2 and 95 % humidity in T75 or T125 culture flasks. HEK293, HeLa and U2OS cells were cultured in DMEM (4.5 g/L glucose, pyruvate, with GlutaMAX™) supplemented with 10 % FBS and 1% (v/v) penicillin-streptomycin.
Cells with 70 - 90% confluency were passaged every 2 - 3 days using 0.05% Trypsin/EDTA. Cell number was determined by using the Neubauer chamber. All cell lines were tested negative for mycoplasma using the PCR mycoplasma kit Venor GeM Classic (Minerva Biolabs) and the Taq DNA polymerase (Minerva Biolabs). Since this study does not include cell line-specific analysis, all cell lines were used without additional authentication.

2.2.3.2 Cell seeding

For cell seeding all adherent cell lines were detached using 0.05 % trypsin-EDTA and cell number was determined by using the Neubauer chamber. For microscopical analyses 5000 – 10,000 cells were seeded per well into µClear 96-well plates while for biochemical analysis, 3 x 10^6 cells were seeded onto 100 mm culture dishes and were allowed to grow for 24 h under standard conditions.

2.2.3.3 Transfection

Transient transfection of U2OS and HeLa Kyoto cells with Lipofectamine 2000 (Thermo Fisher Scientific) was carried out according to the manufacturer's protocol. Briefly, for each well of a 96-well plate, 100 ng DNA and 0.25 µl Lipofectamine 2000 were diluted in 20 µl OptiMEM, incubated for 15 min at room temperature and added to the cells. Media was changed 6 h after transfection and the cells cultivated for 24 - 48 h at 37°C, 5 % CO_2 and 95 % humidity. HEK293 cells were transfected with PEI working solution (1 mg/ml PEI in PBS, pH 7). Prior to transfection, the cells were allowed to grow to ~70% confluency. DNA-PEI complexes for

transfection in 100mm plates were prepared by diluting 15 µg plasmid DNA in 200 µl OptiMEM and adding the PEI-OptiMEM mix to 70 µl PEI solution in 568 µl OptiMEM, vortexing and incubation at 15 min at room temperature. The complexes were added dropwise to the cells which were incubated for 24 - 48 h under standard conditions.

2.2.3.4 Immunofluorescence

For immunofluorescence staining, HeLa cells were seeded at 1 x 10^4 cells per well in µClear 96 well plates and grown to 70 - 90% confluence. For the exogenous expression of Fbox-Nb constructs and/or target antigens, the cells were transfected with plasmids as described in section 2.2.3.3. 24 h post transfection, the cells were washed twice with PBS and fixed with 4% (w/v) paraformaldehyde (PFA) in PBS for 10 min at RT and blocked with 5% BSA in TBST for 30 min at RT. Incubation with required primary antibodies, Nbs or AF_{647}-labelled Nbs was performed overnight at 4°C. Unbound antibodies or Nbs were removed by three washing steps with TBST. Unlabelled Nbs were detected by addition of a Cy5-conjugated goat anti-alpaca IgG according to manufacturer's guidelines. Appropriate secondary antibodies diluted in 3% BSA in TBST were incubated for 1 h at room temperature. Nuclei were subsequently stained with 4', 6 diamidino-2-phenylindole (DAPI) for 15-30 min at room temperature. The wells were washed thrice with PBST and stored in PBS. Images were acquired immediately afterwards with an ImageXpress™ Micro Confocal High Content Screening system (Molecular Devices) at 40x magnification.

2.2.3.5 Microscopy and time-lapse imaging

8 x 10^3 U2OS or 1 x 10^4 HeLa cells/well were plated in a black µclear 96-well plate. 24 h after plating, cells were transiently transfected with plasmids encoding Miro1- or DRP1-Cbs and the corresponding GFP-tagged antigen. The next day, the medium was replaced by live-cell visualization medium $DMEM^{gfp-2}$ (Evrogen) supplemented with 10% FBS and 2 mM L-glutamine. For live-cell imaging, images were acquired after 10-15 min under standard conditions with the ImageXpress™ Micro Confocal High Content Screening system at 40x magnification. For visualization of mitochondrial dynamics in living cells, U2OS cells transiently expressing GFP-Miro1 and Miro1-Cbs or mito-mKate2 were either treated with 10 µM Sorafenib tosylate (to induce mitochondrial fragmentation) or DMSO (as a control) in live-cell visualization medium and imaged every 15 min for up to 2 h under standard conditions.

2.2.3.6 Automated image segmentation and analysis

For the targeted Miro1 degradation experiments, 8 x 10^3 - 1 x 10^4 wildtype HeLa cells or HeLa cells transiently co-expressing Fbox-Nb-IRES-TagRFP$_{NLS}$ and GFP-Miro1 constructs were fixed and permeabilized in a black µclear 96-well plates. For endogenous Miro1, immunofluorescence staining of Miro1 was performed as described in section 2.2.3.4 and images were acquired immediately with an ImageXpress™ Micro system at 40x magnification. Image analysis was performed with MetaXpress software (64 bit, 6.2.3.733, Molecular Devices). Fluorescence images comprising a statistically relevant number of cells (>500 cells) were acquired for each construct. For quantitative fluorescence analysis, the mean Miro1 fluorescence in the cytosol was determined. Using the Custom Module Editor (version 2.5.13.3) of the MetaXpress software, an image segmentation algorithm that identifies areas of interest based the parameters of size, shape, and fluorescence intensity above local background was set up. The settings identifying the cytosolic compartment with Miro1 fluorescence were (i) an appropriate width between 10 µm and 80 µm and (ii) a minimum intensity of 1000 A.U above local background. Nuclear regions were identified by DAPI staining utilizing the following settings: (i) an appropriate width between 5 µm and 30 µm and (ii) a minimum intensity of 2000 A.U. The algorithm was designed to also quantify Miro1 fluorescence signals specifically in cells transfected with the bicistronic vectors coding for both Fbox-Nb degrons and nuclear localized TagRFP. In such cells, a nuclear TagRFP fluorescence of 2000 A.U above local background was defined as selection criteria for Miro1 quantification. An overlay of the generated masks was then applied to the fluorescence image to identify whole cells. For the determination of background fluorescence, the whole cell segmentation mask identifying all cells in an image was used as a negative marker and the background signal was determined in the remaining region. The average Miro1 fluorescence intensities in whole cells were determined for each image followed by subtraction of background fluorescence. The resulting values from the transfected cells were normalized to the non-transfected control. Standard errors were calculated for three independent replicates and student's t test was used for statistical analysis. An overview of the automated image segmentation for transfected cells and non-transfected cells are shown in **Figure 7A** and **Figure 7B** respectively.

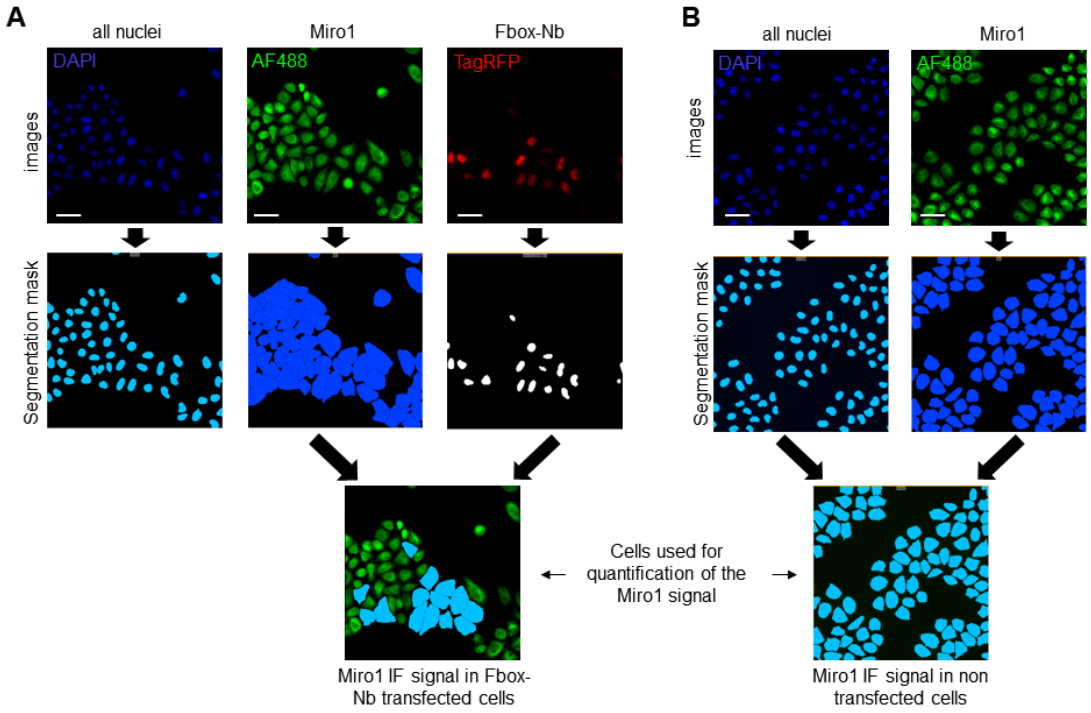

***Figure 7**. Schematic overview of automated image segmentation steps used for quantitative immunofluorescence analysis of GFP-Miro1 or Miro1 signal in (**A**) transfected and (**B**) wild HeLa cells.*

2.2.4 Immunological methods

In this project, Miro1- and DRP1-specific Nbs were selected from libraries generated from immunized alpacas. The alpacas were immunized with recombinantly expressed Miro1 (aa 1-290) or DRP1. The methods used to immunize and monitor the alpacas' immune response are discussed in the following sections.

2.2.4.1 Alpaca immunizations

Animal immunizations were performed after approval by the government of Upper Bavaria (Permit number: 55.2-1-54-2532.0-80-14). Two alpacas (*Vicugna pacos*), Caro and Sora were each immunized with recombinant human Miro1 (aa 1-290) or recombinant human DRP1 respectively. For Caro who was immunized with Miro1, an initial priming dose of 1 mg was administered, the animal then received booster injections of 0.5 mg after the 3rd, 4th, 7th, and 12th week. For Sora, an initial priming dose of 0.48 mg DRP1 was administered. Subsequently, the animal received booster injections of 0.24 mg after the 3rd, 4th, 7th and

12th week. The immune response of both alpacas was enhanced by co-administration of Gerbu Pharma Adjuvant #3003 to ensure a gentler immune reaction. 20 ml serum samples were collected from each alpaca after the 9th and 13th week and analysed for seroconversion.

2.2.4.2 Serum ELISA

In the 9th and 13th week after immunization, 20 ml serum samples were collected from each alpaca and analysed for seroconversion. The blood was drawn by Dr. Stefan Nüske (LMU, Munich) from the external jugular vein (*Vena jugularis externa*) of the alpaca in vacuum bottles (Evozone) pretreated with Heparin (Ratiopharm). Sera were generated by centrifugation of blood (2000 rpm, 10 min and 4°C). For the serum ELISA, 1 µg of the appropriate antigen was coated in a 96-well Maxisorp™ plate and the serum from Caro or Sora was added in serial dilutions and incubated for 4 h at 4 °C. the wells were washed 5 to 6 times with precooled PBS and bound alpaca antibodies were detected with an HRP-conjugated anti-VHH antibody for 1 h at room temperature. The wells were washed thrice and 100 µl substrate solution containing the chromogenic substrate 3,3',5,5'-Tetramethylbenzidin (TMB) was added. Subsequently, a conversion reaction catalyzed by the HRP takes place resulting in a blue coloring of the solution. The reaction was stopped by adding 1 M sulfuric acid resulting in a colour change to yellow. The absorbance was measured at 450 nm in a microplate reader (Infinite M1000, Tecan).

2.2.4.3 B-cell isolation

100 ml of blood was collected from each alpaca and lymphocytes were isolated by Ficoll gradient centrifugation using the Lymphocyte Separation Medium (PAA Laboratories GmbH). ~6×10^7 and ~11×10^7 B cells were obtained from Caro and Sora respectively.

2.2.4.4 cDNA synthesis

The preparation of the cDNAs from isolated mRNA was performed by ChromoTek (Germany). Briefly, total RNA was extracted from ~2×10^7 isolated B cells from each animal using the Nucleospin® RNA II kit according to the manufacturer's instructions. RNA yields up to 34.2 µg was obtained each and was reverse transcribed to cDNA using a First-Strand cDNA Synthesis Kit (GE Healthcare) according to the manufacturer's instructions.

2.2.5 Phage Display methods

2.2.5.1 Construction of Nb-phage library

2.2.5.1.1 Amplification of Nb genes

The Nb repertoire was amplified in 3 subsequent nested PCR reactions. For the first reaction, the cDNAs extracted from isolated B cells were used as template (PCR1,**Table 11**). The PCR1 product was loaded on an agarose gel, the bands of desired size excised and purified (as described under section 2.2.1.3) and used as template for the second PCR (PCR2, **Table 12**). The amplification product was purified using standard protocols and used as template for the third PCR (PCR3, **Table 13**). **Table 14** summarises the amplification programs used for all 3 nested PCRs.

Table 11*. Components of the first PCR (PCR1) amplification of Nb genes*

Component	**Amount**	**Final concentration**
Q5 HotStart® polymerase	0.5 µl	0.02 U/µl
Q5 5× Reaction buffer	10 µl	1×
Q5 5× High GC enhancer	10 µl	1×
Template (cDNA)	5 µl	
dNTP mix	1 µl	0.2 mM/ nucleotide
Forward primer (CALL001)	2 µl	0.4 µM
Reverse primer (CALL002)	2 µl	0.4 µM
Nuclease free H_2O	19.5 µl	

Table 12*.Components of the second PCR (PCR2) amplification of Nb genes*

Component	**Amount**	**Final concentration**
Q5 HotStart® polymerase	0.5 µl	0.02 U/µl
Q5 5× Reaction buffer	10 µl	1×
Q5 5× High GC enhancer	10 µl	1×
Template (PCR1 product)	1 µl	0.2 ng/µl
dNTP mix	1 µl	0.2 mM/ nucleotide
Forward primer (FR1-1, FR1-2, FR1-3, FR1-4)	2.5 µl each	0.5 µM/ primer
Reverse primer (CALL002)	2.5 µl	0.5 µM/primer
Nuclease free H_2O	15 µl	

***Table 13**. Components of the last PCR (PCR3) amplification of Nb genes*

Component	**Amount**	**Final concentration**
Q5 HotStart® polymerase	0.5 µl	0.02 U/µl
Q5 5× Reaction buffer	10 µl	1×
Q5 5× High GC enhancer	10 µl	1×
PCR2 product	1 µl	0.2 ng/µl
dNTP mix	1 µl	0.2 mM/ nucleotide
Forward primers (FR1-ext1, FR1-ext2)	0.5 µl each	1 µM/ primer
Reverse primers (FR4-1, FR4-2, FR4-3, FR4-4)	0.75 µl	1.5 µM/ primer
Nuclease free H_2O	23.5 µl	

***Table 14**. Amplification program for PCR1-3*

Step	**temp (°C)**	**Duration**	**Number of cycles**
Initial denaturation	95	3 min	
Denaturation	95	30 s	20× (PCR1) 15× (PCR2) 15× (PCR3)
Annealing	61 (PCR1) 60 (PCR2) 58 (PCR3)	30 s	
Extension	72	45 s	
Final extension	72	7 min (PCR1) 5 min (PCR2 and 3)	
Hold	4	∞	

2.2.5.1.2 Cloning of Nb genes into phagemid vectors

The PCR3 amplification product was purified by agarose gel electrophoresis according to standard protocols and digested with *SfiI* and *NotI* restriction endonucleases. Restriction digests were performed as described under section 2.2.1.2. In parallel, the phagemid pHEN4 vector was also digested with the same endonucleases to produce compatible overhangs for ligation. Sodium acetate and ethanol precipitation was applied for the purification of the digested phagemid vector. Briefly, 3 M sodium acetate (pH 5.2) was added to the restriction

digest products to a final concentration of 0.3 M. 2.5-fold volume of 95% ethanol was then added and the mixture incubated at -80 °C for 1 h. The mixture was then centrifuged at 20000 × g for 30 min at 4 °C. The pellet was washed with 70 % ethanol, dried in a SpeedVac concentrator and the DNA pellet resolubilized in nuclease free water. 10 ligation reactions were performed using a 1:3 phagemid vector to Nb gene insert ratio according to the protocol described under section 2.2.1.6.

2.2.5.1.3 Transformation of E.coli *TG1* and library generation

For the generation of Nb-phage libraries, electro-competent *E.coli* TG1 cells (Lucigen) were transformed by electroporation with the ligation reactions according to the manufacturer´s protocol. For each library, 5 transformations with controls were performed. The transformed bacteria were plated on 2xYT plates containing 100 µg/ml ampicillin and 2%(w/v) glucose (2xYT-amp+glu plates) and incubated overnight. From these plates 30 single clones were picked randomly per library to determine the diversity of the libraries by sequence analysis. The library size was also determined by counting the single clones on each plate. The colonies were gently scaped off the plates with 10 ml 2xYT medium containing 100 µg/ml ampicillin, 2% (w/v) glucose and 15% glycerol. These stocks were aliquoted into 1 ml cryotubes, flash frozen in liquid N_2 and stored at -80°C as the primary Nb-phage display libraries.

2.2.5.2 Preparation of phage particles

To produce phage particles for Nb selection by phage display (biopanning), *E.coli* TG1 cells containing the primary Nb-phage libraries were inoculated to 1000 ml 2xYT media (with 100 µg/ml AMP and 2 % (w/v) glucose) cultured at 37 °C and 130 rpm until reaching a logarithmic growth phase (OD_{600} ~0.5). 50 ml of the culture was then infected with 5×10^{10} M13K07ΔpIII helper phages (Progen). Incubation was done at 37 °C for 30 min without shaking. The cells were harvested by centrifugation, followed by resuspension of the cell pellet in 100 ml 2xYT medium containing 100 µg/ml ampicillin and 25 µg/ml kanamycin and incubated at 37 °C overnight. Subsequently, the produced phage particles expressing Nb domains on their surface were harvested from the supernatant by precipitation with 20 % polyethylene glycol (PEG) 6000 for 1 h on ice, followed by centrifugation (30 min, 4000 rpm, 4°C). Finally, the phage pellet was resuspended in PBS or HEPES buffer and stored at 4 °C.

2.2.5.3 Solid phase biopanning

Iterative biopanning approaches were used to enrich phage particles expressing Nb domains specific for these antigens from each respective library. For each antigen, 1 x 10^{11} phages, prepared from the respective culture supernatant by PEG precipitation, were used for each panning process. Extensive blocking of antigen and phages was performed in each selection round with 5% milk or BSA in PBST (PBS, 0.05% Tween 20, pH 7.4) as previously described (Pardon et al. 2014).

For the selection process using recombinant Miro1 or DRP1, phages from the indicated library were first applied on immunotubes coated with GFP (10 µg/ml) to deplete non-specific binders and then transferred to immunotubes either coated with Miro1 (10 µg/ml) or DRP1 (10 µg/ml)or GFP (10 µg/ml) as non-related proteins in both cases. Incubation steps were performed at room temperature for 2 h. Washing stringency was increased for each selection round. Bound phages were eluted in 100 mM triethylamine (pH 12.0), followed by immediate neutralization with 1 M Tris/HCl pH 7.4. For the panning process using GFP Miro1, 2 × 10^7 HEK293 cells transiently expressing GFP-Miro1 or GFP were harvested and lysed as previously described under section 2.2.2.10. GFP-Miro1 and GFP were immobilized respectively on GFP-Trap® Multiwell plates according to manufacturer's protocol. To deplete GFP-specific binding molecules, phages were first applied into wells displaying GFP and then transferred into wells with immobilized GFP-Miro1. All incubation steps of three consecutive selection rounds were performed at 4°C for 2 h under constant mixing. Washing and elution steps were carried out equally as described above. After each panning round, exponentially growing *E.coli* TG1 cells were infected with eluted phages and spread on selection plates to rescue the enriched phagemids for the next panning round. Antigen-specific enrichment for each round was monitored by counting colony forming units (CFUs).

2.2.5.4 Phage ELISA

To select Miro1 or DRP1-specific Nb-phage clones from phage clones enriched through biopanning rounds, monoclonal phage ELISA was performed. 100 single TG1 clones from biopanning against Miro1 (purified and GFP-Miro1), and 260 single clones from biopanning against DRP1 were grown in 96-well assay blocks. Phage particles were produced in the supernatants of these cultures as previously described under section 2.2.5.2.

Purified Miro1 or DRP1 were immobilized on MaxiSorp™ plates (10 µg/well) and blocked with 5% MPBS. Purified GFP was used as control antigen for both targets. For GFP-Miro1, 2 × 10^7 HEK293 cells transiently expressing GFP-Miro1 or GFP were harvested and lysed as previously described under section 2.2.2.10. GFP-Miro1 or GFP were immobilized respectively

on GFP-Trap® Multiwell plates according to manufacturer's protocol. Monoclonal phage particles were added and incubated for 2 h at room temperature. Subsequently, plates were washed thrice with PBST (0.05 % Tween in PBS) and thrice with PBS. Detection of specifically bound phages was performed using a HRP-conjugated anti-M13 monoclonal antibody (GE-Healthcare) and Thermo Scientific™1-Step™ Ultra TMB solution.

2.2.5.5 Preparation of libraries for Next Generation Sequencing

For the mining of the Miro1 Nb library and panning sub-libraries by NGS, the Nb sequences in the Miro1 unpanned library (MUL), the sub-library of enriched phagemids after the first and second panning rounds (MFL1 and MFL2) were amplified and barcoded with Illumina adapter primers by PCR. First, glycerol stocks of each library were inoculated into 2YT media containing 100µg/ml AMP and 2%(w/v) glucose and cultivated until OD_{600} was greater than 2. Plasmid Miniprep extraction was then carried out using 10 ml of each culture. Standard PCR reactions in triplicates were then set up using primers, Adaptor-phagemid-for and Adaptor-phagemid-rev at 61 °C annealing temperature. The PCR products were pooled and purified by agarose gel electrophoresis as described in section 2.2.1.3. The purified amplicons were then sent for NGS sequencing using the Amplicon EZ service provided by Genewiz GmbH (Leipzig, Germany).

3 RESULTS

This section details the multiple steps taken for the (i) generation, (ii) selection, (iii) characterization and (iv) application of Miro1 and DRP1-specific nanobodies (Nbs) as outlined in **Figure 8**. First, the antigens, Miro1 and DRP1, were recombinantly expressed and purified for immunization and Nb screening (1). Following the immunization (2), Nb phagemid libraries were generated for each antigen (3). These libraries were used for Nb screening by iterative rounds of phage display followed by subsequent phage ELISAs to identify antigen specific Nbs (4). Selected Nbs were characterized in biochemical and cell biological assays and functionalized (5) and used for different research applications (6).

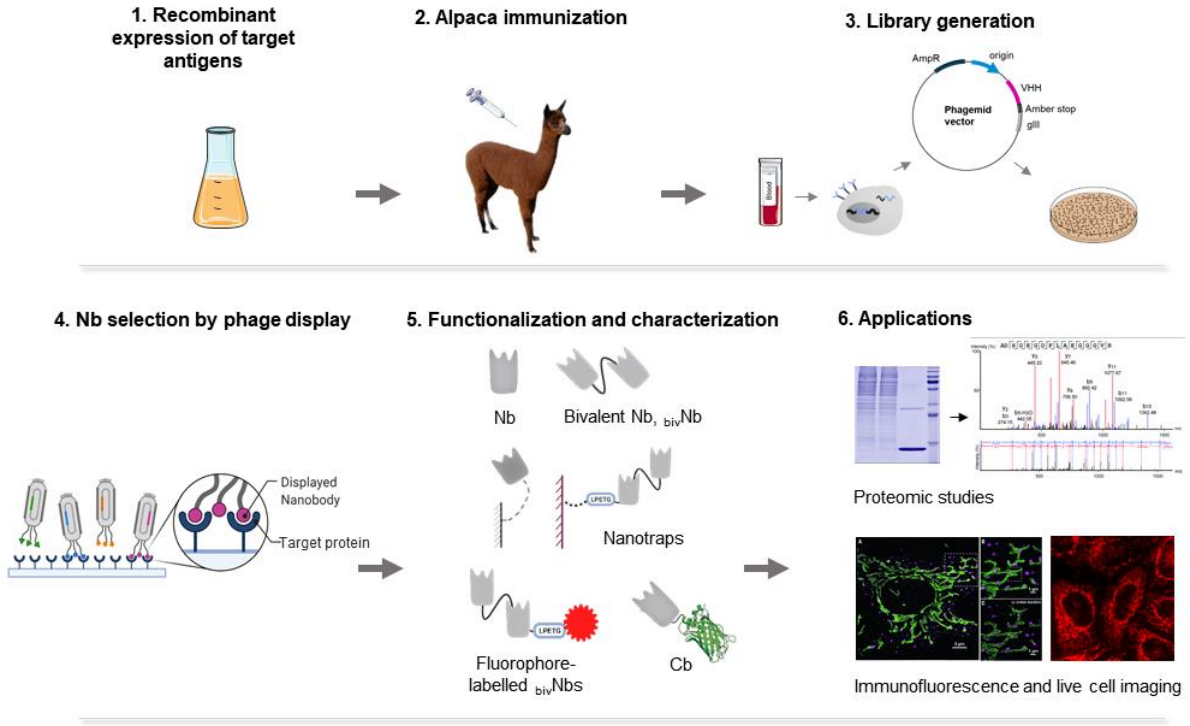

Figure 8. *Graphical illustration of the workflow used for the generation and characterization of Miro1- and DRP1-specific Nbs*

3.1 Nanobody library construction

3.1.1 Target protein expression and purification

To generate specific Nbs, recombinantly expressed and purified antigens were required for alpaca immunization and Nb selection steps. For the development and selection of Miro1-specific Nbs, three antigen constructs (depicted in **Figure 9A**) were produced in different hosts and used in this study. Human Miro1 (aa 1-290) comprising the N-terminal GTPase and EF1 domains fused to a C-terminal hexahistidine tag (His_6-tag) was expressed, purified and utilized for immunization. For Nb selection and characterization, purified human Miro1 (aa 1-592) expressed in High Five™ insect cells were provided by Natascha Bartlick (University of Tübingen, Germany) was used. SDS-PAGE analysis of purified Miro1 (aa 1-290) and Miro1 (aa 1-592) followed by Coomassie staining is shown in **Figure 9B**. Nbs were also selected using GFP-Miro1 expressed in mammalian cells. **Figure 9C** shows an immunoblot of the soluble and pellet fraction of lysed GFP-Miro1 expressing HEK293 cells.

For the generation and selection of DRP1 specific Nbs, recombinant human DRP1, was expressed in *E.coli* BL21 RIPL cells and purified by anion exchange chromatography (provided by Andreas Jenner, University of Cologne, Germany). This protein was used throughout this study for all purposes requiring purified DRP1 unless otherwise stated. A SDS-PAGE analysis of the provided protein followed by Coomassie staining is shown in **Figure 9D**.

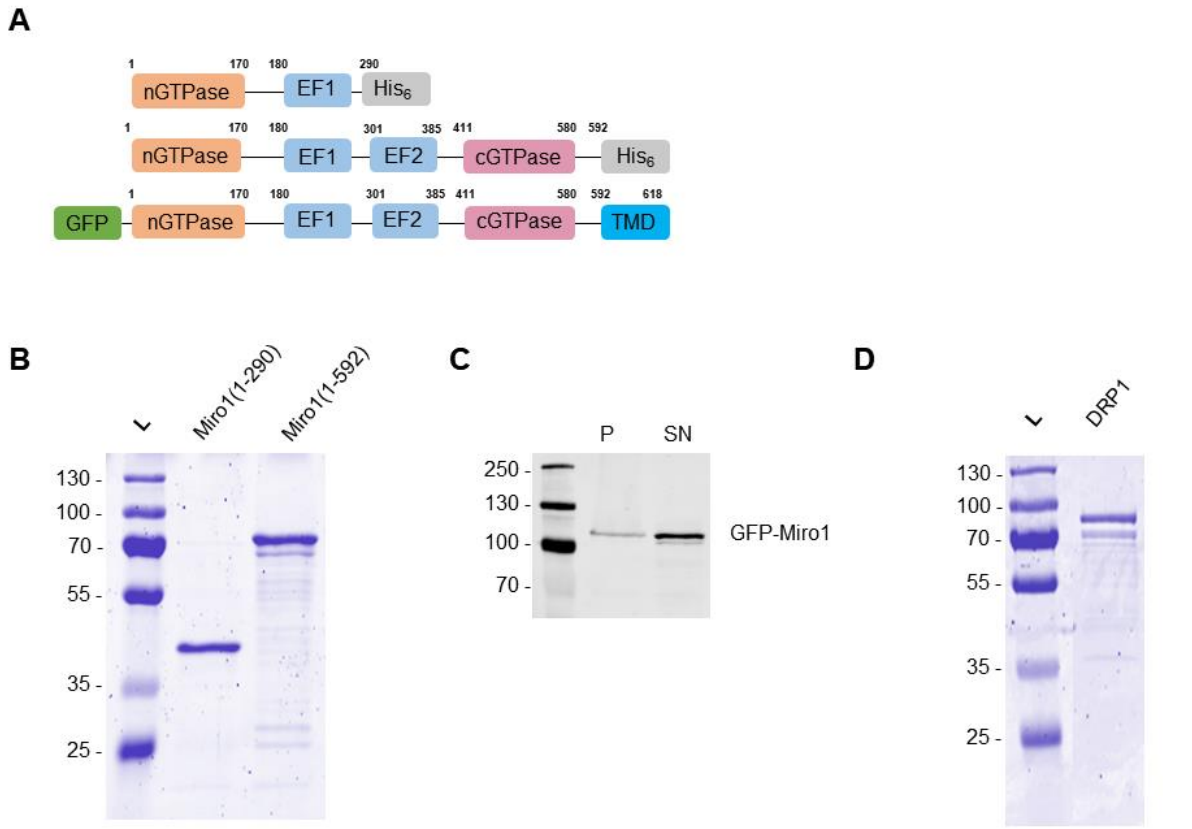

***Figure 9**. Recombinant antigens used in this study. (**A**) Schematic illustration of Miro1 constructs used for immunization (aa 1-290); for Nb screening, selection, and characterization (aa 1-592) and GFP-Miro1 (aa 1-618). (**B**) Coomassie stained gel of 1 µg each of purified Miro1 (aa 1-290) and Miro1 (aa 1-592) (**C**) Western blot analysis of 10 µg of soluble (SN) and insoluble/pellet (P) protein fractions of lysed HEK293 cells transiently expressing GFP-Miro1. Detection of GFP-Miro1 was with an anti-GFP antibody (**D**) Coomassie stained gel of 1 µg of purified DRP1*

3.1.2 Alpaca immunization

For Nb generation, two alpacas were immunized following the schedule shown in **Figure 10A**. The humoral immune response to Miro1 or DRP1 was investigated in each alpaca after 9 and 13 weeks. 20 ml of blood was collected per animal and the presence of Miro1- or DRP1-specific hcAbs in the alpaca's sera was analysed by ELISA (performed by Andrea Buchfellner, ChromoTek). **Figure 10B** and **10C** shows the concentration-dependent detection of the antigens by hcAbs derived from the alpacas' sera. After detection of a positive immune response 100 ml of blood was collected from each animal on the fourth day after the last booster dose was administered.

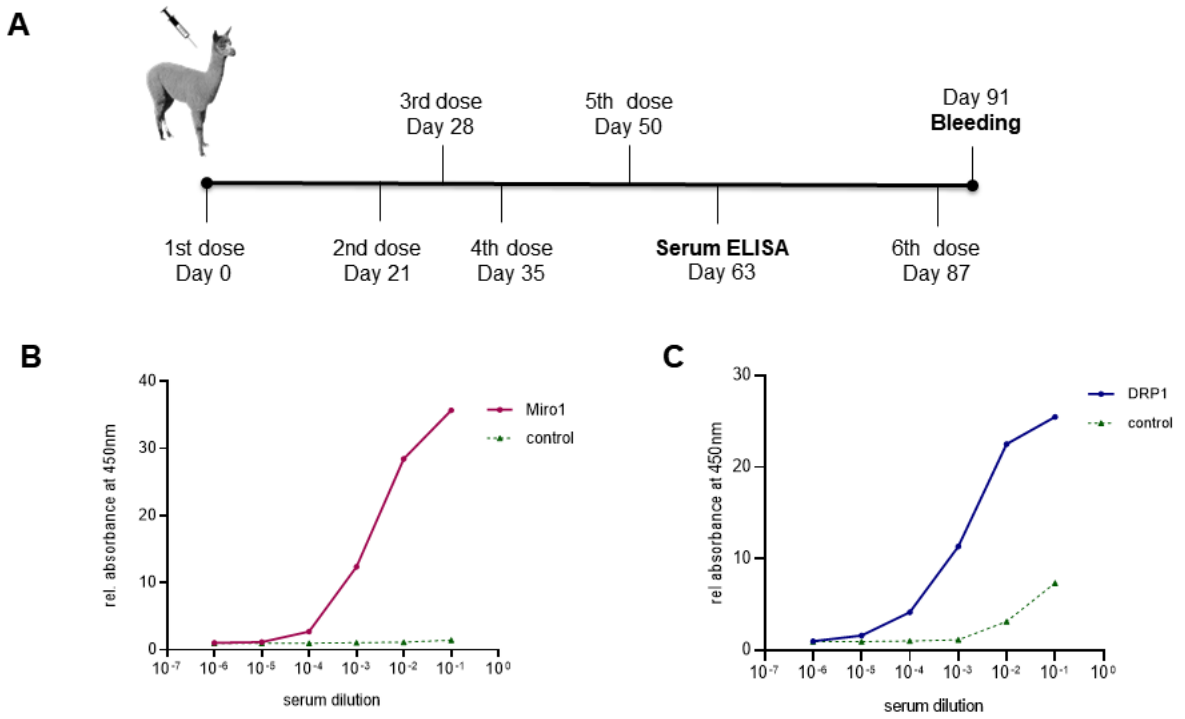

***Figure 10**. Animal immunization and analysis of seroconversion. (**A**) Immunization schedule of an alpaca with Miro1 (aa 1-290) or DRP1. For Miro1 immunization, a 1 mg start dose on Day 0 followed by five 0.5 mg booster doses were administered to alpaca named Caro. For DRP1 immunization, an 0.5 mg start dose followed by five 0.25 mg booster doses were administered to the alpaca Sora. Presence of (**B**) Miro1-specific hcAbs or (**C**) DRP1-specific hcAbs by the animal was measured in a serum ELISA at indicated dilutions in multiwell plates either coated with the respective antigen or BSA as negative control. Bound antibodies were detected using an anti-alpaca hcAb secondary antibody labelled with horse radish peroxidase.*

3.1.3 Generation of Nanobody phage libraries.

From ~1 x 10^8 PBMCs obtained from each alpaca's blood sample, mRNAs were extracted, and reverse transcribed into cDNA (performed by ChromoTek). The cDNA comprised the whole immune repertoire of each animal. In order to generate Nb-phage libraries for the phage display-based selection of Miro1- or DRP1-specific Nbs, the V_HH gene fragments were amplified from the cDNAs in three consecutive PCRs and cloned into pHEN4 phagemid vectors (**Figure 11A**).

In the first PCR, both VH and VHH gene fragments were successfully amplified with primers CALL001 and CALL002. The amplicons were separated by agarose gel electrophoresis and the bands corresponding to the VHH genes (~700bp) were excised and purified. The purification product served as the template for the second nested PCR reaction in which the forward primer set FR1-1, FR1-2, FR1-3, FR1-4 and reverse primer, CALL002 were used to amplify the VHH genes from their framework 1 region to the CH2 domain (lower than 700bp in size). The amplicons were purified by agarose gel electrophoresis and used as the template in the final nested PCR step. Using forward primers FR1-ext1 and FR1-ext2; and reverse primer set FR4-1, FR4-2, FR4-3, FR4-4, FR4-5 and FR4-6, the VHH genes were amplified from the framework 1 to the framework 4 regions with insertion of *SfiI* and *NotI* restriction sites upstream and downstream of the gene fragments respectively. The resulting amplicons (~400bp) were purified by agarose gel electrophoresis followed by digestion with *SfiI* and *NotI*. The digestion products were ligated into *SfiI/NotI* digested pHEN4 phagemid vector and transformed into *E.coli* TG1 cells by electroporation to generate either the Miro1 or DRP1 Nb-phage library. **Figure 11B** shows a representation of the pHEN phagemid vector with inserted Nb gene.

The size and quality of the Nb-phage libraries were further investigated by first plating out dilution series of the TG1 transformants. Next, the number of single clones obtained was used to determine the corresponding library size. The Miro1- and DRP1 Nb-phage libraries were found to encompass ~1.5 x 10^7 and 2.3 x 10^7 Nb-phages respectively (**Table 15**). 20 random clones were picked from each library and VHH inserts were checked by colony PCR. In both libraries, all screened colonies possessed successfully inserted VHH genes. This was confirmed by agarose gel analysis shown in **Figure 11C**. However, on determination of the complexity of both libraries by sequencing of 30 random clones (also shown in **Table 15**), 87% and only 57% of the Nb sequences from the Miro1 and DRP1 Nb-phage libraries respectively were found to be unique.

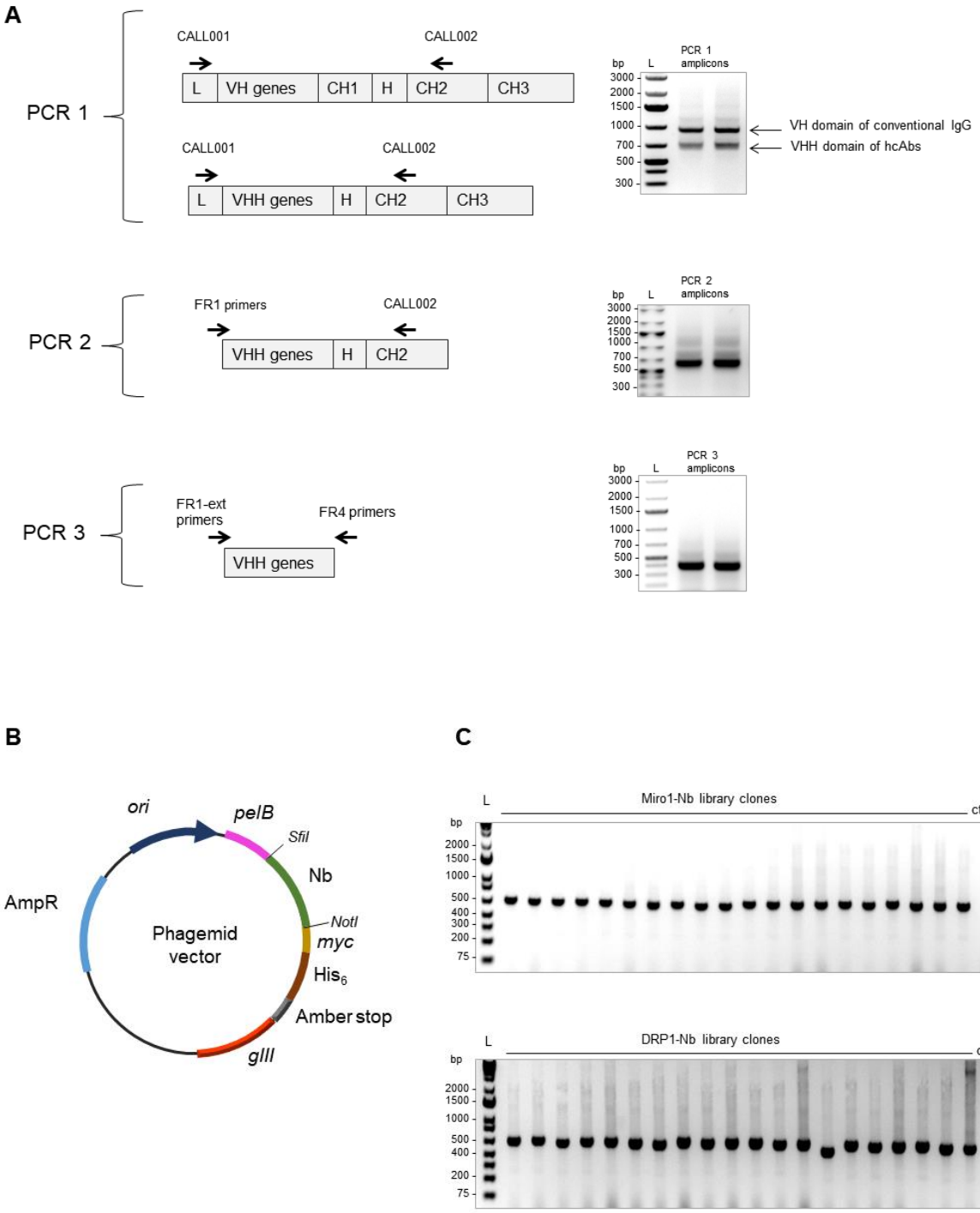

Figure 11. *Generation of Nb-phage libraries (**A**) Nested PCR amplification of VHH genes from the mRNA derived cDNA isolated from PBMCs of Miro1- and DRP1-immunized alpacas using the indicated primer sets. Amplified V_HH repertoire was digested and ligated into pHEN4C phagemid vector (**B**) Schematic illustration of pHEN4C phagemid vector with pelB; signal peptide for periplasm-targeted expression, SfiI and NotI restriction sites; a VHH insert with myc and hexahistidine tags, an amber stop codon (TAG), gIII; M13 pIII phage coat protein and*

*AmpR; Ampicillin resistance gene. (**C**) Agarose gel analysis of colony PCRs to check VHH inserts in Miro1 and DRP1 Nb-phage libraries using primers, p4-NMI_for and p4-NMI_rev.*

***Table 15**. Sizes and complexities of Miro1 and DRP1 Nb-phage libraries*

Library	Size (titer)	Complexity (per 30 sequences)
Miro1	1.5×10^7	83%
DRP1	2.3×10^7	57%

3.2 Miro1-specific Nbs

One of the aims of this thesis was the identification and application of Nbs as tools to characterize the mitochondrial GTPase, Miro1. To accomplish this aim, the generated Miro1 Nb-phage library was panned, specific Miro1-binding Nbs were selected, characterized, and used for different applications. This section describes the steps taken and the results obtained.

3.2.1 Phage display based selection of Miro1-specific Nbs.

After establishing a Miro1 specific Nb-phage library, it was screened for antigen specific Nbs specifically by biopanning and single Nb-phage clones were identified by phage ELISA. Therefore, phage particles displaying Nbs in combination with the pIII coat protein on their tip were produced from the library and two rounds of biopanning using either recombinant Miro1 (aa 1-592) or GFP-Miro1 from HEK293 cells were performed. In the first approach, phage were first panned against purified GFP immobilized on immunotubes to obtain a preblocked phage solution. Subsequently the preblocked phages were panned against purified Miro1 (aa 1-592). In total, two consecutive biopannings were performed using this setup. After the first panning round, over 10-fold enrichment of bound phages relative to GFP as control was observed which increased to 3000-fold by the end of the second panning round as detailed in **Table 16**.

***Table 16**. Enrichment of Miro1 Nb-phages during biopanning against Miro1 (aa 1-592).*

Panning round	Phage input	Eluted phages (Miro1 (aa 1-592))	Eluted phages (control)
1	1.0×10^{11}	1.0×10^{5}	1.3×10^{4}
2	5.0×10^{11}	5.5×10^{6}	3.3×10^{3}

In the second approach, HEK293 cells transiently expressing GFP-Miro1 (depicted in **Figure 9A**) or GFP were lysed, and the GFP-tagged antigens were captured on GFP-Trap™ plates for panning against pre-blocked phages. Three iterative biopanning rounds were done with two preclearing steps included in each round to deplete non-specific binding phages by panning the library against non-transfected HEK293 cell lysates followed by two more preclearing steps using cell lysates from GFP-transfected cells. A 10-fold enrichment of bound phages relative to the control was observed after the first panning round. Though there was an increase in bound phages over subsequent panning rounds, there was less than 10-fold enrichment of phages binding to GFP-Miro1 compared to GFP. **Table 17** shows the phage titers obtained during each panning round.

Table 17. Enrichment of Miro1 Nb-phages during biopanning against GFP-Miro1 expressed in HEK293 cells.

Panning round	Phage input	Eluted phages (GFP-Miro1)	Eluted phages (control)
1	1.0×10^{11}	1.3×10^{6}	2.0×10^{5}
2	8.5×10^{11}	1.7×10^{6}	2.3×10^{5}
3	2.1×10^{11}	1.5×10^{9}	1.8×10^{8}

After an enrichment of Miro1-bound phages compared to the non-specific binding phages in both biopanning strategies was observed, individual Nb-phage clones were then analysed from the last panning sub-library by phage ELISA. Therefore, phage supernatants from 100 clones were produced which were subsequently screened against purified Miro1 (aa 1-592) or GFP-Miro1 in a phage ELISA format. As negative control GFP was used. Binding of monoclonal phages was detected using a HRP-conjugated anti-M13 antibody (**Figure 12**).

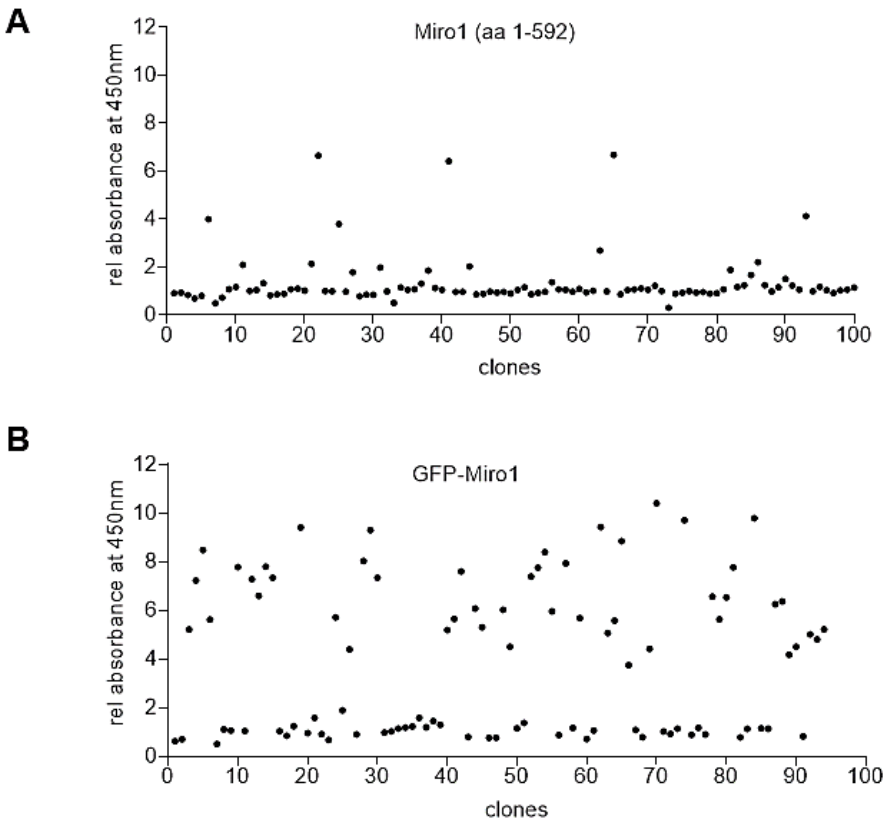

***Figure 12**. Phage ELISA profile of 100 eluted phage clones tested for binding to (A) Miro1 (aa 1-592) and (B) GFP-Miro1. Signal intensities were normalized to the signal obtained for binding to the control antigen.*

In total, phage ELISA revealed 15 and 42 positive binding Nb-phages against Miro1 (aa 1-592) and GFP-Miro1, respectively. Subsequently plasmid preparations were carried out for all selected clones and subjected to Sanger sequencing.

3.2.2 Sequence characterisation of Miro1-specific Nbs

In total genetic sequence analysis revealed seven unique Nbs sequences. Four Nbs were derived from panning against purified Miro1 (M11, M25, M41 and M85) and 3 Nbs derived from the panning against GFP-Miro1 (M114. M119 and M189). Many recurring sequences were identified from each panning sub-library which was expected and due to the enrichment of identical Nbs during this process. Notably, the Nb candidate, M41 was selected against both bacterial and HEK293 expressed Miro1. All seven Miro1-Nbs were aligned according to the

Kabat numbering system (Kabat and Wu 1991) for comparison of their framework and hypervariable regions. (**Figure 13A**).

All selected Nbs showed high sequence homologies in their framework regions. However, distinct variations were in the hallmark residues within the FR2 region at positions 37, 44, 45 and 47 (in red letters). Here, hydrophobic amino acids were found at the hallmark positions 37, 44 and 45 in the sequences of M11 and M41 which are more characteristic for conventional VH domains compared to VHHs (Muyldermans et al. 1994; Harmsen et al. 2000). Notably, M114 and M189 originated from the same germline as they have the same CDR1 and CDR2 regions and differ only in their CDR3 indicative of a different VDJ recombination or extensive somatic hypermutation. The CDR3 regions of the Nbs show different lengths ranging between 9 and 25 amino acids. M85 and M119 showed the most extended CDR3s displaying 19 or 25 amino acids respectively. Apart from the extended CDR3, both Nbs possessed additional cysteine residues in their FR2 and CDR3. It has been reported that Nbs can compensate for the lack of a light chain by extended CDR3 loops which are stabilized by an additional disulphide bridge formed between additional cysteines in the CDR1 or FR2 and CDR3 (Desmyter et al. 1996; Muyldermans et al. 2001; Conrath et al. 2003).

In addition to the genetic characterisation of the Miro1-Nbs selected by conventional panning approaches, Next Generation Sequencing (NGS) was applied to further validate the enrichment of Nbs over each consecutive panning round. The large number of sequencing reads obtained by NGS enables rapid library quality control and can also evaluate the binding potential of Nb repertoires (Deschaght et al. 2017). The Miro1 Nb-phage library and the sub-libraries after each panning round against Miro1 (aa 1-592) were subjected to Illumina® Amplicon EZ sequencing. The sequencing and NGS data processing services were provided by Genewiz Germany GmbH, Leipzig. From the ~50,000 reads obtained per library, the diversity of the parental Miro1 Nb-phage library as well as the enrichment of specific Nb families over each consecutive panning round could be traced. Nb clusters were generated based on sequence similarity and CDR3 residues as previously described (Ravn et al. 2010; Henry et al. 2016; Yaari and Kleinstein 2015). The occurrence of sequences in Nb families identified from panning with Miro1(aa 1-592) are shown in **Figure 13B**. Nb sequences having the same CDR3 and over 70% sequence similarity with M25 were found to be the most abundant after the second panning round. Though some Nbs could not be detected in the parental Miro1 Nb-phage library due to the low read-to-library size ratio, the gradual enrichment of these Nb families over the next panning rounds was apparent. Therefore, the NGS data obtained further supports the Nb selection method by conventional biopanning.

A

```
                FR1                  CDR1      FR2              CDR2                FR3                                  CDR3              FR4
M11   QVQLVESGGGSVQPGGSLRLSCAASG FSFSSNVMS WARQAPGKGLEWVSG IYVDG--------R THYADSVKGRFTISRDNAKNTVYLQMNSLKPEDTAVYYC AAAGDLSG-----YS--FSPYDYDY WGQGTQVTVSS 124
M25   HVQLVESGGGLVQPGGSLRLSCIASG FTFSDVGMA WYRQIPGKERDMVAS ITSFG-------DQ TSYAHSVKGRFTISRDNAKNTVYLQMNTLIPDDTAMYYC ------TT----------VLGRERR WGQGTPVTVSS 116
M41   EVQLVESGGGLVHPGGSLRISCAASG FSFNSSAMS WARQAPGKGLEWVSG IQADG--------T TGYAHSVKGRFNISRDNAKNIVYLQMSSLKPEDSAVYYC AKEGWSTV----------VFGSRDY WGQGTQVTVSS 121
M85   DVQLVESGGGKVQSGGSLRLSCAASG SKLDDYSIG WFRQAPGKGREGISC ITMKT-------GS FEYVDSVKGRFTISADNAKNTVHLQMNNLKPEDTGIYYC AALRSRGL-----FC-VTSPYEYDL WGQGSPVTVSS 126
M114  EVQLQESGGGLVQPGGSLRLSCTASG FPVSSAAMS WARQSPGKELEWVSG IYTDG--------S ADYADSLKGRFTISRDDVENTINLQMNSLKPEDTAVYYC KTDWWAGP----------SGYVAV WGQGTLVTVSS 120
M119  DVQLVESGGGLVQPGGSLRLSCATSG FPLDNYAIG WFRQAPGSEREGVSC ISSSGSYFPGSGSR THYAHSVKGRFTISRDGAKNTVYLQMDNLKPEDTAVYYC AAVPVPSIRTAETMCVRGSLSEFIS WGQGSQVTVSS 139
M189  EVQLVESGGGLVQPGGSLRLSCTASG FPVSSAAMS WARQSPGKELEWVSG IYTDG--------S ADYADSLKGRFTISRDDVENTINLQMNNLKPEDTAIYYC NANFFEG----------SWYDY WGQGSPVTVSS 118
      .*** ***** *: *****:** :**   ...  :. * ** **.  : ::  *              *..*:****.** *..:* : ***..* *:*:.:***                    ****: *****
```

B

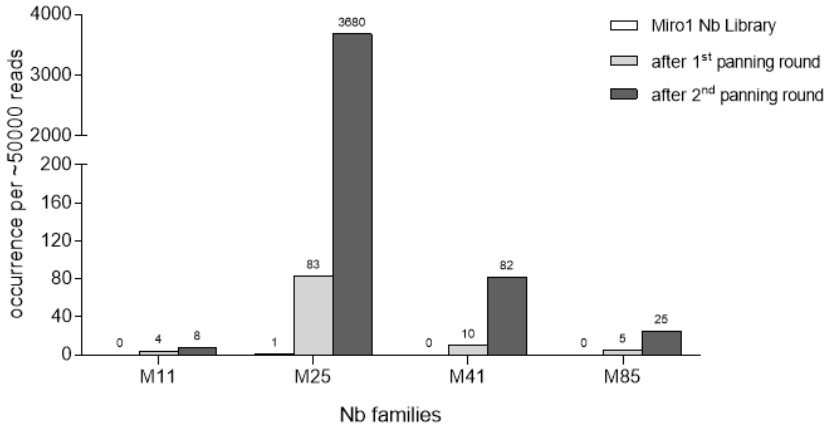

***Figure 13**. Sequence characteristics of Miro1- Nbs. (**A**) Amino acid sequence alignment of selected Miro1-Nbs showing residues in the framework regions (FR) and the CDRs. The hallmark residues characteristic of V_HH or VH sequences are highlighted in red. * (asterisk) indicates positions which*

*have a fully conserved residue, : (colon) indicates positions with residues possessing similar properties, .(dot) indicates positions with residues with weakly similar properties.(**B**) Enrichment of selected Nbs after biopanning rounds against Miro1 (aa 1-592), as determined by NGS.*

3.2.3 Validation of selected Miro1-Nbs by Protein ELISA

In a next step, selected Miro1-Nbs were tested for antigen binding in a protein ELISA. To express them as isolated Nbs in the absence of the pIII fusion the coding sequences were shuttled from the pHEN4C phagemid vector into the pHEN6C vector. Here, different variants of the pHEN6C vector either comprising either a C-terminal tri-lysine peptide or a Sortase recognition motif (LPETG) followed by a hexahistidine tag were used. After sequencing to ensure correct insertion and sequence integrity, the constructs were transformed into *E.coli* XL1 and periplasmic extracts (PPE) were prepared. For the protein ELISA a 1:5 dilution of the PPE were analysed for binding of the Nb to their respective antigen or control protein (**Figure 14**). All Nbs demonstrated more than two-fold signal intensity from binding interactions with Miro1 (aa 1-592) or GFP-Miro1 compared with GFP as control. These results further confirmed the specificity of the selected Miro1-Nbs at the protein level.

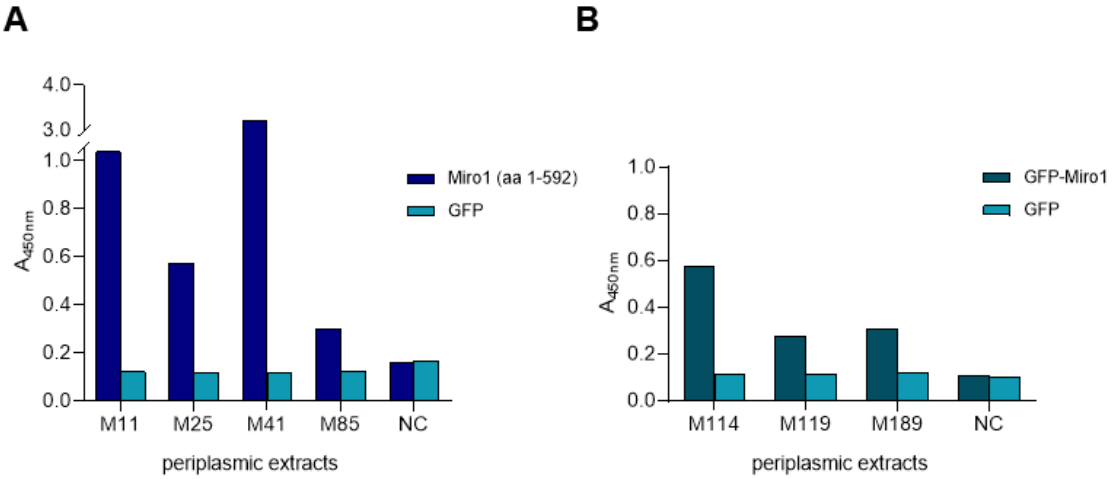

***Figure 14**. Results of a protein ELISA to screen for reactivities of selected Nbs derived from a periplasmic E.coli extract against (A) Miro1 (aa 1-592) and (B) GFP-Miro1. Bound Nbs were detected using an anti-VHH antibody labelled with horse radish peroxidase, (*n=*1).*

3.2.4 Expression and purification of selected Miro1-Nbs

For further analysis and proposed applications, all seven Miro1-Nbs were expressed in *E.coli* and purified via immobilized metal ion affinity chromatography (IMAC). For a second purification step size exclusion chromatography (SEC) was performed and the purified Nbs were concentrated by ultrafiltration. As a representative example of the purification steps of all Nbs described in this project, the chromatograms of the M11 purification by IMAC and SEC are shown in **Figure 15A** and **15C** respectively. After SEC, the Nbs were concentrated, and a final purity assessment was done by SDS analysis of 2 µg of each Nb (**Figure 15E**). Nb yields of up to 16 mg were obtained from 1L expression culture.

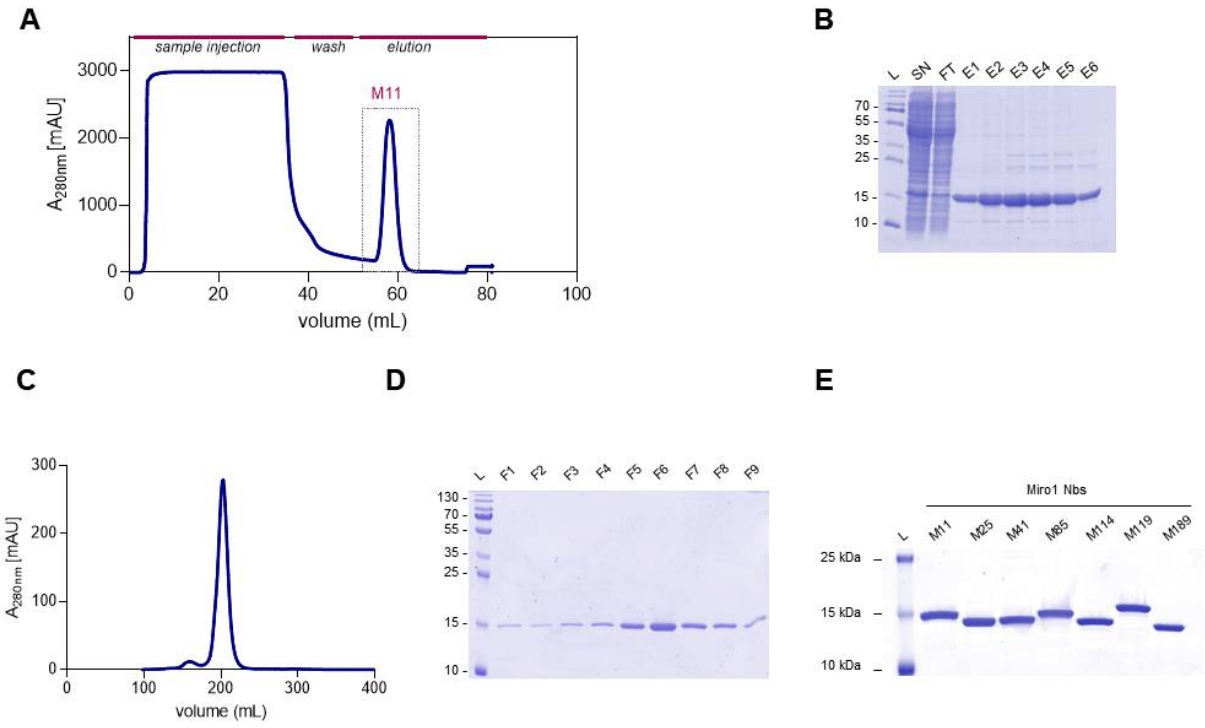

***Figure 15**. Recombinant expression and purification of Miro1-Nbs. (**A**) Chromatogram of IMAC purification of M11 with the eluted Nb peak highlighted with dotted lines.(**B**) SDS-Page analyses of the soluble fraction after cell lysis (SN), flow through fraction (FT), the fractions from the eluted protein peak (E1-E6). A protein molecular weight marker (L) was included in the first lane as size standard.(**C**) size exclusion chromatogram of M11. (**D**) SDS-Page analyses of all fractions corresponding to the eluted protein peak. (F1-F6) (**E**) Coomassie stained gel showing 2 µg of purified Miro1-Nbs.*

3.2.5 Biochemical characterization of Miro1-Nbs

For application of Nbs as tools to study Miro1, there is a need for a comprehensive characterization of the nature of the binding interactions between Miro1 and each selected Nb. In this section, the kinetics of Nb binding to Miro1, the functionality of each Nb in biochemical assays (functional characterization) and the domains being targeted by each Nb will be elucidated.

3.2.5.1 Binding affinity measurements

For further characterization binding affinities of the selected Nbs were determined by biolayer interferometry (BLI). BLI is a label-free method which measures the interference pattern of white light reflected from a layer of immobilized protein on a biosensor tip and an internal reference layer. It is based on the principle that binding between the immobilized ligand and another molecule in an analyte solution produces a change in optical thickness at the biosensor tip which results in a wavelength shift which is proportional to binding. With this method, the equilibrium binding constant (K_D) and kinetic rates of association (k_{ON}) and dissociation (k_{OFF}) can be measured using nanomolar quantities of sample (Sultana and Lee 2015).

For BLI measurements purified Nbs were biotinylated and immobilized on streptavidin biosensors. The binding kinetics were then quantified by loading different concentrations of Miro1 (aa 1-592). The data obtained were analysed using a 1:1 ligand-binding model and global fitting. The association and dissociation profiles as well as the fitted curves of the seven selected Miro1-Nbs with the respective Miro1 concentrations are represented as sensograms in **Figure 16A-G**. M41 demonstrated the highest affinity for Miro1 at ~ 1.96 nM while M25 showed the least affinity even with higher concentrations of Miro1 tested. M41 had the quickest association rate of 3×10^5 M^{-1} s^{-1} with Miro1 commensurate with its steep association profile (**Figure 16C**). Compared with the other Miro1-Nbs, the interactions between Miro1 and Nbs M41, M114 and M1189 showed relatively slower dissociation rates. Association and dissociation rate constants calculated for M25 were not considered due to the little or no interaction observed. The quantified kinetic parameters with their corresponding coefficients of determination are summarized in **Table 18**.

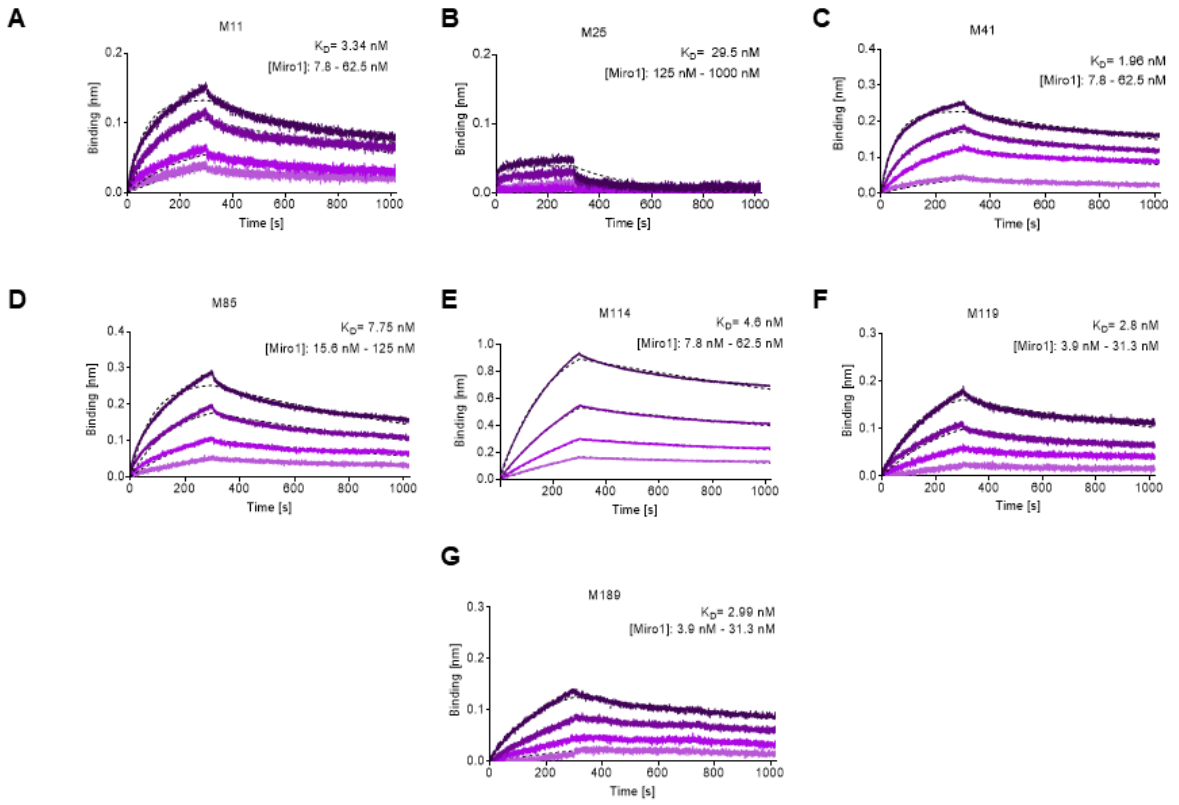

***Figure 16**. Binding affinities of Miro1 specific Nbs. Affinity measurements by BLI of Miro1 at indicated concentrations on immobilized (**A**) M11 (**B**) M25 (**C**)M41 (**D**)M85 (**E**) M114 (**F**) M119 and (**G**) M189. The different concentrations of Miro1 ranging from 3.9 nM to 1 µM are illustrated with increasingly darker shades and the global 1:1 fits are represented as dashed lines.*

***Table 18**. Summary of affinities (K_D), association (k_{ON}) and dissociation constants (k_{OFF}) and the coefficient of determination (R^2) determined for Miro1-Nbs by biolayer interferometry.*

Nanobody	K_D (nM)	k_{ON} (10^5 M^{-1} s^{-1})	k_{OFF} (10^{-4} s^{-1})	R^2
M11	3.34	2.55 ± 0.02	8.54 ± 0.03	0.97
M25	29.50	1.36 ± 0.04	0.40 ± 0.28	0.80
M41	1.96	3.01 ± 0.01	5.89 ± 0.02	0.99
M85	7.75	1.00 ± 0.01	7.79 ± 0.02	0.99
M114	4.61	0.88 ± 0.01	4.04 ± 0.01	0.99
M119	2.80	2.25 ± 0.01	6.31 ± 0.02	0.99
M189	2.99	1.70 ± 0.01	5.07 ± 0.02	0.98

Overall, the results showed that all seven Nbs bind Miro1 with high affinities in the low nanomolar range.

3.2.5.2 Functional characterization of Miro1-Nbs

Nbs are versatile binding molecules that have been used for various applications (Hassanzadeh-Ghassabeh et al. 2013). They can be covalently immobilized to solid matrices such as agarose particles and have been previously applied as effective pulldown reagents to capture their antigens (Rothbauer et al. 2008; Maier et al. 2015; Braun et al. 2016; Buchfellner et al. 2016). To determine the functionality of the selected Miro1-Nbs for immunoprecipitation, purified Nbs were covalently coupled to N-hydroxysuccinimide (NHS)-activated agarose particles thereby generating Miro1-nanotraps. As a first step, the capacity of the nanotraps to specifically immunoprecipitate GFP-Miro1 was tested. HEK293 cells expressing GFP-Miro1 were lysed and a soluble fraction of the total cell lysate obtained by centrifugation. The soluble fractions were then subjected to immunoprecipitation with the Miro1 nanotraps. Immunoblot analysis of input and bound fractions revealed that all Miro1-nanotraps except M11 and M85 efficiently precipitated GFP-Miro1, with M114 and M119 exhibiting the highest pulldown efficiencies comparable to the positive control, a commercially available high-affinity GFP nanotrap (Rothbauer et al. 2008) (ChromoTek). Notably, none of the Miro1 nanotraps showed unspecific binding to GFP or GAPDH used as an endogenous control (**Figure 17A-B**).

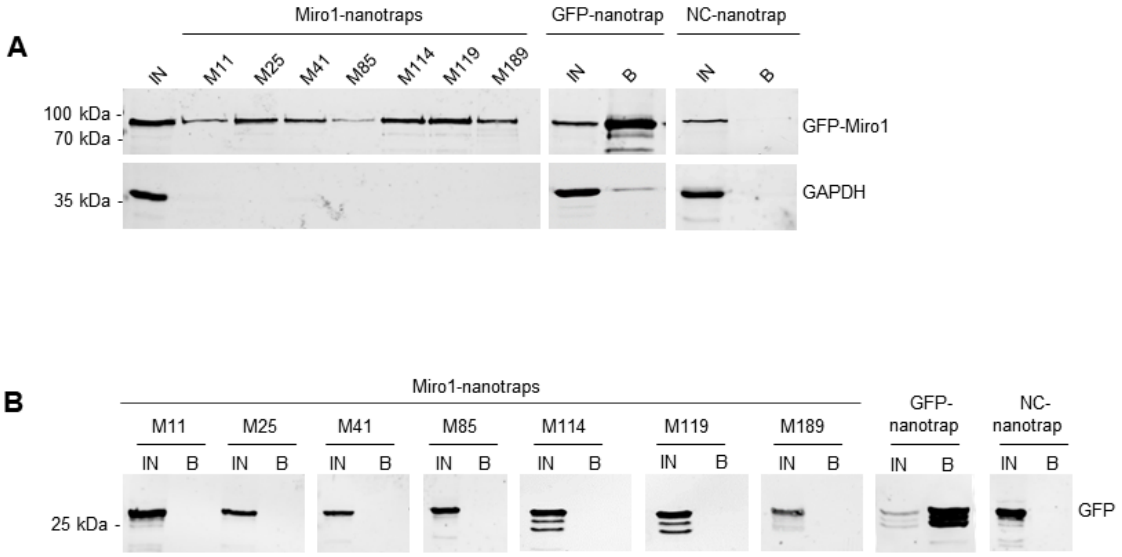

Figure 17. *Immobilized Miro1-Nbs (nanotraps) specifically bind Miro1. For immunoprecipitation with immobilized Nbs (nanotraps), soluble protein fraction of HEK293 cells transiently expressing GFP-Miro1 (**A**) or GFP as control (**B**), was adjusted to 2 mg/ml and incubated with equal amounts of nanotraps. Input (IN, 1% of total) and bound (B, 20% of total) fractions were subjected to SDS-PAGE followed by immunoblot analysis using antibodies specific for GFP (upper panel) and GAPDH (lower panel). As positive control GFP-nanotrap and as negative a non-specific (NC) nanotrap were used.*

After confirming the potential of the immobilized Nbs to enrich exogenously expressed Miro1, the nanotraps were further tested to bind endogenous Miro1. In initial experiments, it was observed that the levels of Miro1 in the soluble protein fraction were rather low. Therefore different cell types and lysis conditions were tested in order to find more optimal conditions for transferring endogenous Miro1 to the soluble protein fraction. However, results from these experiments showed that even upon lysis with the partially denaturing RIPA buffer only minor fractions of endogenous Miro1 were transferred to the soluble protein fraction (**Figure 18A-C**). Nonetheless, for the intended pulldown studies HEK293 cells were chosen because of the relatively higher levels of Miro1 detectable in these cells. Also, the non-denaturing TritonX-100 lysis condition was used as standard protocol for the preparation of cell lysates for endogenous Miro1 immunoprecipitation.

Using this method, the soluble fractions were then subjected to immunoprecipitation with Miro1 nanotraps. Immunoblot analysis revealed Miro1 in the bound fractions of M41, M114, M119 and M189. The levels of precipitated Miro1 were comparable or slightly higher to those

obtained with a conventional anti-Miro1 antibody. Also, no unspecific binding of endogenous GAPDH to any of the Miro1 nanotraps was detected (**Figure 18D**). These findings indicated that at least four of the selected Miro1-Nbs are able to bind epitopes within endogenous Miro1.

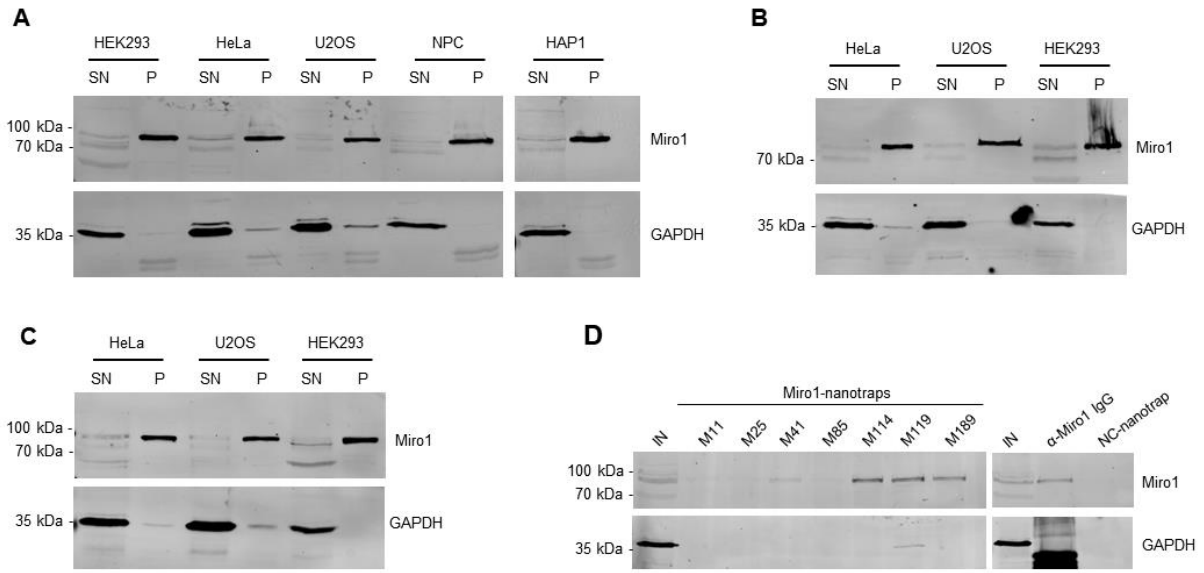

***Figure 18**. Immunoprecipitation of endogenous Miro1**.** Endogenous Miro1 retains in the insoluble protein fraction in different cell lines**.** Representative western blot analysis of 20 µg of soluble (SN) and insoluble/pellet (P) fractions of indicated cells after addition of (**A**) 0.5% NP-40 or (**B**) 1% Triton X-100 in the lysis buffer or (**C**) upon lysis in denaturing radioimmunoprecipitation assay (RIPA) buffer. (**D**) Soluble protein fraction of HEK293 cells prepared as described in (B), was adjusted to 2 mg/ml and incubated with equal amounts of Miro1 nanotraps. Input (IN, 1% of total) and bound (B, 20% of total) fractions were subjected to SDS-PAGE followed by immunoblot analysis. As positive control anti-Miro1 IgG immobilized on Protein A/G sepharose and as negative control a non-specific (NC) nanotrap was used. Upper parts of the blots were detected with anti-Miro1 antibody. Detection of GAPDH with an anti-GAPDH antibody was used as lysis and loading control.*

Next the performance of Miro1-Nbs in immunofluorescence (IF) was investigated. In a first step, the Nbs were applied as primary binding molecules in combination with fluorescently labelled anti-VHH antibodies in fixed and permeabilized HeLa cells transiently expressing GFP-Miro1. Interestingly, Nbs M11 and M25, which did not enrich endogenous Miro1 by immunoprecipitation showed a clear co-localization with GFP-Miro1 at mitochondrial structures. This result suggests that these Nbs recognize epitopes that were not accessible or

structurally altered under the lysis conditions used for immunoprecipitation. With both functionality tests, the applicability of M41 for both IP and IF assays was demonstrated. (**Figure 19**).

Notably, none of the selected Miro1-Nbs seems to recognize endogenous Miro1, as there was no clear detection of Miro1 resembling ani-Miro1 antibody staining (data not shown). This did not change after testing of different fixation or permeabilization methods. At this point, it could be only speculated whether the epitopes of endogenous Miro1 are blocked by binding partners or thatstructural changes occurred during fixation and permeabilization of the cells which prevented the detection of endogenous Miro1. It is also conceivable that the binding kinetics of the Miro1-Nbs were not optimal for their functionality as primary binding molecules in immunofluorescence.

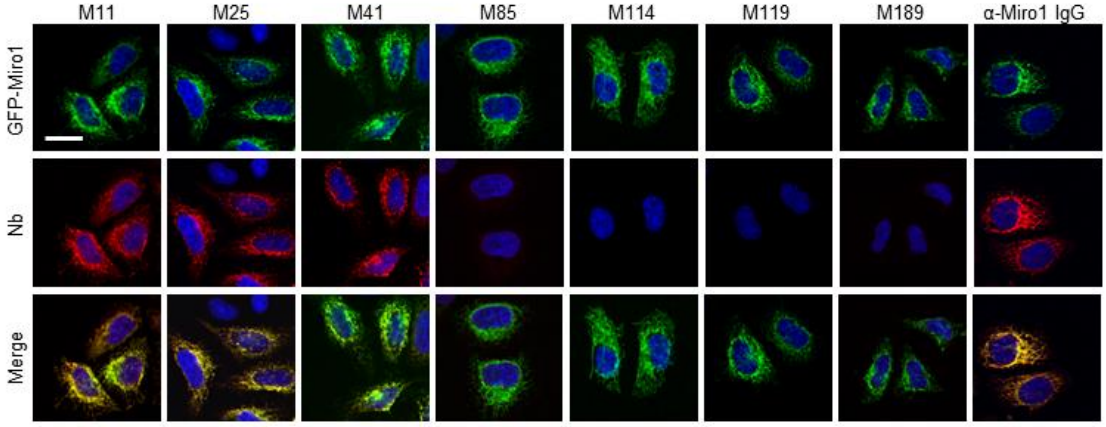

***Figure 19**. Functional characterization of Miro1-Nbs in IF staining. Immunofluorescence (IF) detection of GFP-Miro1 in fixed and permeabilized HeLa cells after staining with Miro1-Nbs as primary labelling probes. Representative confocal laser scanning (CLSM) images are shown of each individual Nb detected with anti-VHH antibody labelled with Cy5 (middle row). As positive control, transfected cells were stained with anti-Miro1 antibody followed by detection with a Cy5-labelled secondary antibody. Nuclei were counterstained with DAPI. Scale bar 20 µm.*

3.2.5.3 Domain binding characteristics of Miro1-Nbs

To generate well-characterized binders, detailed knowledge of their recognized epitopes or domains is imperative. The knowledge of the epitope of a Nb aids in the prediction of the possible effects of its binding to its target protein. Considering that Nbs preferentially bind conformational epitopes (De Genst et al. 2006; Pardon et al. 2014) and that Miro1 domains

play different roles in its molecular functions (Smith et al. 2020), domain mapping was performed to identify the binding regions recognized by Miro1-Nbs. To accomplish this, a series of Miro1 domain deletion constructs fused C-terminally to GFP were generated (**Figure 20A**). After successful sequence analysis, the deletion constructs were transiently expressed in HEK293. Using the Miro1 nanotraps, pull down studies were performed according to previously stated protocol. Analysis of the bound fractions revealed that M11, M41, M85, M114 and M189 specifically recognize epitopes within the C-terminal GTPase domain while M25 addresses an epitope spanning the N-terminal GTPase in combination with the EF-hand domains. For M119, interactions involving regions of the EF hands as well as the C-terminal GTPase domains were observed (**Figure 20B**).

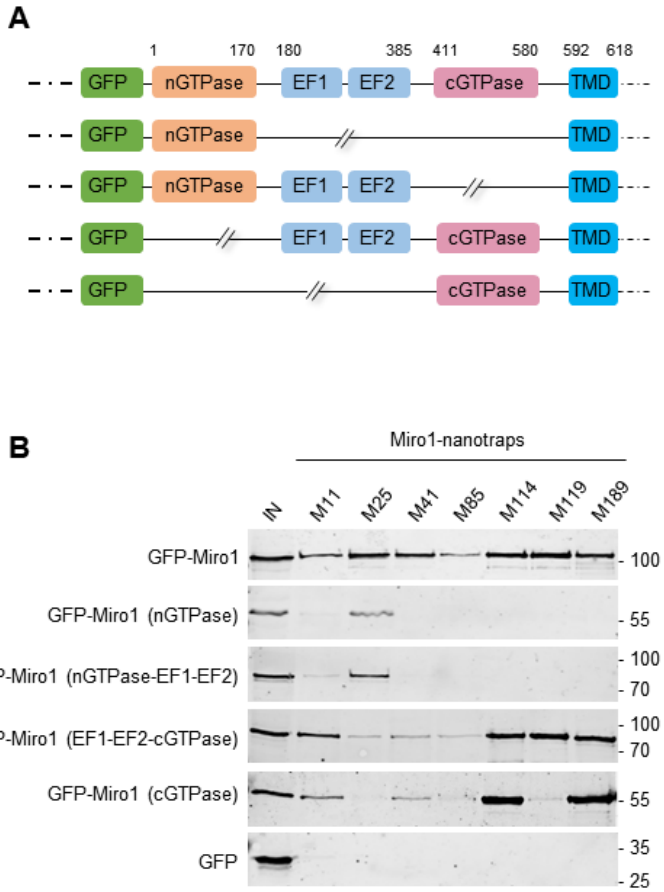

***Figure 20**. Domain mapping of Miro1-Nbs. (**A**) Schematic illustration of GFP-labelled Miro1 deletion constructs and domains used for domain specific binding studies. (**B**) Soluble protein fractions of HEK293 cells transiently expressing indicated Miro1 deletion constructs or GFP (as control) were subjected to immunoprecipitation with selected Miro1 nanotraps followed by*

western blot analysis of input (IN) and bound fractions with an anti-GFP antibody. Data were obtained with the contribution of Grace Jarjour (University of Tübingen, Germany).

3.2.6 Generation of bivalent Miro1-Nbs as optimized binding agents

As shown by immunoprecipitation and immunofluorescence studies, selected Miro1-Nbs bind only minor levels of endogenous Miro1. Thus in a next step, bivalent formats of two Nbs were generated to improve their binding performance. For these, M41-Nb and M114-Nb were selected based on their performance after functional characterization studies. First, M41-Nb showing a high affinity for Miro1 in the BLI assay, could enrich both endogenous and exogenous Miro1 in IP studies. In IF, M41-Nb also effected crisp detection of GFP-Miro1 in fixed and permeabilized HeLa cells. Secondly, M114-Nb was selected based on its immunoprecipitation of exogenous and endogenous Miro1 at comparable levels with commercially available binding molecules.

Therefore, the coding sequences of two M41- or two M114-Nbs were genetically fused head-to-tail, bridged by a flexible Gly-Ser linker ($(G_4S)_4$) of 20 amino acids to generate a bivalent M41-Nb ($_{biv}$M41) and a bivalent M114-Nb ($_{biv}$M114). The bivalent Nbs were produced in mammalian cells and subsequently purified (see **Figure 21A**). The different running behaviour observed with $_{biv}$M41 is due to N-glycosylation of $_{biv}$M41 during its mammalian expression (MS analysis performed by Anne Zeck, NMI Reutlingen) .

The binding kinetics of both bivalent Nbs with purified full length Miro1were analyzed by BLI. The association and dissociation profiles of $_{biv}$M41 and $_{biv}$M114 and the fitted curves with the respective Miro1 concentrations are represented as sensorgrams in **Figure 21B-C**. $_{biv}$M41 demonstrated a similar affinity as its monovalent format showing a K_D oft ~1.8 nM. Other kinetic parameters also remained similar in both formats. However, for $_{biv}$M114 an improved affinity compared with its monovalent format was observed. Especially the bivalent format shows a twofold decreased dissociation rate. The quantified kinetic parameters of both bivalent Miro1-Nbs including their corresponding coefficients of determination are summarized in **Table 19**.

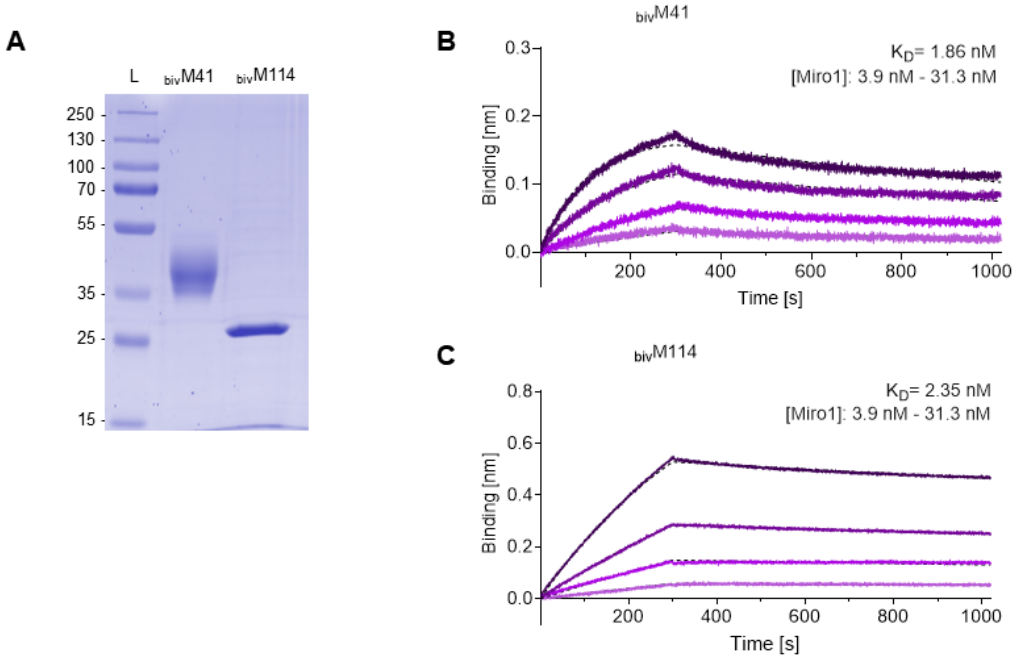

Figure 21. *Recombinant expression, purification, and affinity determination of bivalent M41- and M114-Nbs. (**A**) Coomassie stained SDS-PAGE of 2 µg $_{biv}$M41 and $_{biv}$M114 purified from ExpiCHO™ cells is shown. (**B**) Affinities of the bivalent Miro1-Nbs were analysed by biolayer interferometry (BLI) based affinity measurements. Bivalent Nbs were biotinylated and immobilized on streptavidin sensors. Kinetic measurements were performed by using four concentrations of hMiro1 ranging from 3.9 nM – 31.3 nM (illustrated with increasing concentrations in darker shades). The sensograms of purified Miro1 on $_{biv}$M41-Nb (top) and $_{biv}$M114-Nb (bottom) are shown and global 1:1 fits are illustrated as dashed lines. The table summarizes affinities (K_D), association (k_{ON}) and dissociation constants (k_{OFF}), and coefficient of determination (R^2) determined for both bivalent Nbs.*

Table 19*. Summary of affinities (K_D), association (k_{ON}) and dissociation constants (k_{OFF}) and the coefficient of determination (R^2) determined for bivalent Miro1-Nbs by biolayer interferometry.*

	K_D (nM)	**k_{ON} (10^5 M^{-1} s^{-1})**	**k_{OFF} (10^{-4} s^{-1})**	**R^2**
$_{biv}$M41	1.86	3.19 ± 0.02	5.95 ± 0.02	0.99
$_{biv}$M114	2.35	0.78 ± 0.00	1.83 ± 0.01	0.99

Following biochemical characterization of bivalent Miro1-Nbs, they were functionalized for further applications. As shown previously monovalent Miro1-Nbs were formatted into nanotraps by NHS-based chemical conjugation. This method, which involves the reaction of NHS-ester groups with exposed lysine residues on the Nb could however be random and excessive, leading to loss of Nb functionality (Pleiner et al. 2015; Cheloha et al. 2020). Therefore, for the bivalent Nbs, a site-specific functionalization strategy was used to avoid potential interference with binding by NHS-based modification of lysine residues. Chemoenzymatic functionalization mediated by the Sortase A enzyme was utilized. Sortase A recognizes an 'LPXTG' peptide motif at the C-terminus of the Nb and cleaves between the threonine and glycine residue to yield a reactive thioacyl intermediate. The enzyme then catalyses the formation of a new peptide bond between the thioacyl intermediate and any moiety bearing an N-terminal polyglycine (Popp and Ploegh 2011; Virant et al. 2018; Cheloha et al. 2020). Using this approach, a propyl azide-modified peptide was first introduced at the C-terminus of $_{biv}$M41 and $_{biv}$M114. Immobilization on agarose beads or conjugation to fluorophores was thereafter achieved by click-chemistry addition of a dibenzocyclooctyne (DBCO) derivate (Jewett and Bertozzi 2010). With this two-step approach, the bivalent Nbs were converted into nanotraps and fluorescently labeled imaging probes as summarized in **Figure 22.**

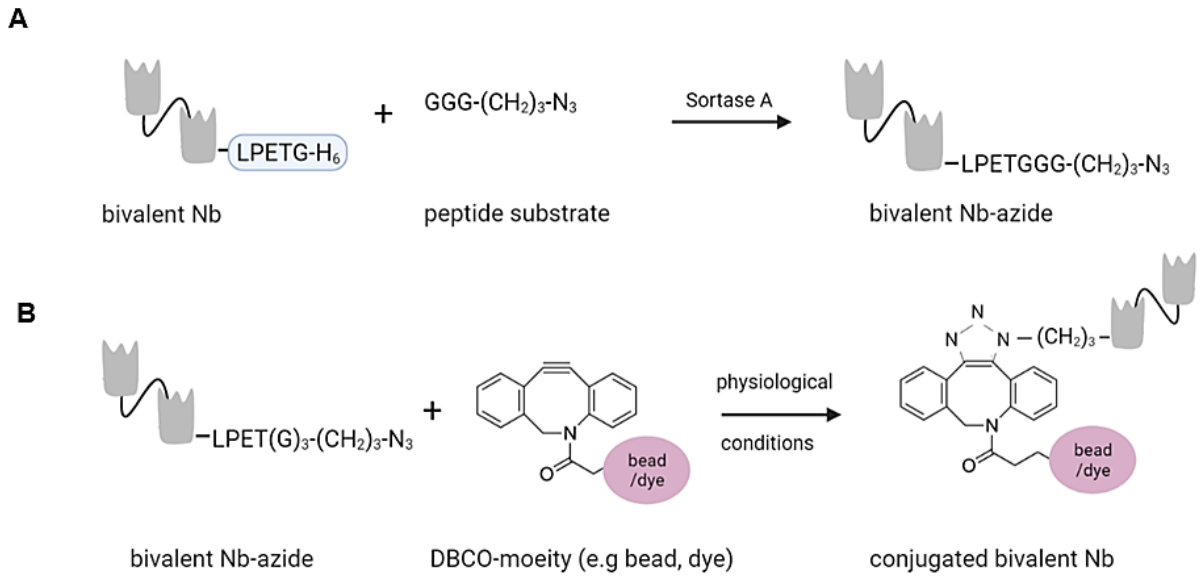

***Figure 22**. Site-specific approach for Nb functionalization starting with (**A**) Sortase mediated conjugation of a propyl azide moiety and subsequent (**B**) click chemistry-based reaction with a dibenzocycloctyne activated dye or sepharose. Adapted from (Jewett and Bertozzi 2010).*

3.2.7 Application of bivalent Nbs for IF detection of Miro1

Previous studies showed that fluorophore conjugated-Nbs can successfully replace conventional antibodies in IF applications (Hassanzadeh-Ghassabeh et al. 2013; Virant et al. 2018). Nanometer spatial resolution of microtubules (Ries et al. 2012) and the nuclear pore complex (Pleiner et al. 2015) were achieved with the use of Nbs labelled with organic dyes in super resolution microscopy. Accordingly, one of the main objectives of this thesis was to generate Miro1-Nbs as novel and reliable fluorescent imaging probes for advanced IF studies of Miro1.

Therefore, monovalent and bivalent formats of M41- and M114 were functionalized for the immunofluorence detection of Miro1 at mitochondrial structures. The monovalent Nbs were chemically coupled by NHS chemistry to AF_{647} or $ATTO_{647}$ ($M41_{647\_NHS}$; $M114_{647\_NHS}$). Apart from the previously stated disadvantages of NHS conjugation, lower signal to noise ratios were reported with the use of Nbs labelled with fluorophores by NHS chemistry (Pleiner et al. 2015). To avoid these drawbacks, the bivalent formats were C-terminally conjugated by sortagging and click chemistry, as mentioned above to AF_{647} ($_{biv}M41_{647\_sort}$; $_{biv}M114_{647\_sort}$). The AF_{647} coupled mono- and bivalent Nbs were then utilized at different concentrations for the staining of untransfected HeLa cells or HeLa cells transiently expressing GFP-Miro1. Notably, the IF detection of GFP-Miro1 was not as efficient with $M41_{647\_NHS}$ compared to indirect IF staining with M41-Nb (see **Figure 19**). This partial loss of functionality may be due to altered specificity of the Nb because of NHS modification.

Moreover, at the same concentration, a significantly improved staining and crisp overlap of the GFP-Miro1 and $_{biv}M41_{647\_sort}$ signal at mitochondrial structures was observed compared to the monovalent version. A detection of GFP-Miro1 was possible with $_{biv}M114_{647\_sort}$, but not its monovalent, NHS-functionalized format with which unspecific and high background staining was observed. Notably, when tested for detection of endogenous Miro1 in HeLa cells, only $_{biv}M114_{647\_sort}$ showed a strong Miro1 staining at mitochondrial structures (**Figure 23**).

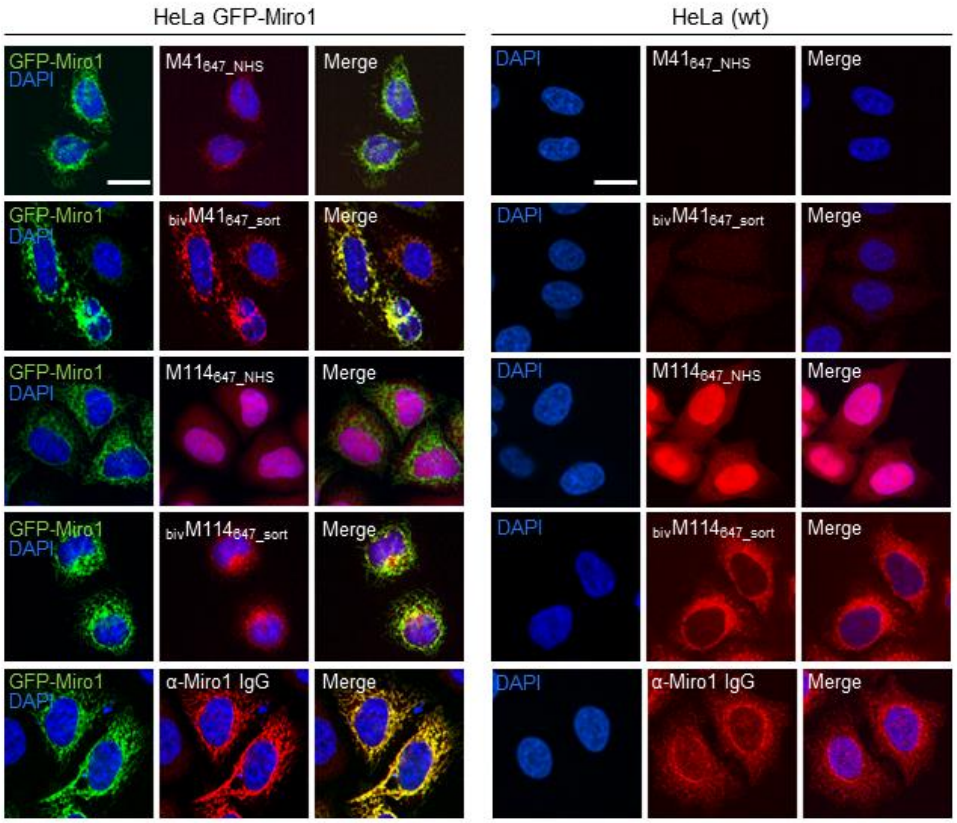

Figure 23. *Comparison of monovalent and site specifically conjugated bivalent M41- and M114-Nbs in immunofluorescence. For comparable IF analysis HeLa cell transiently expressing GFP-Miro1 (left panel) or wildtype (wt) HeLa cells (right panel) were fixed and stained with the mono- or bivalent Nbs conjugated either chemically ($M41_{647\_NHS}$, $M114_{647\_NHS}$) or site-specifically via sortagging ($_{biv}M41_{647\_sort}$, $_{biv}M114_{647\_sort}$) to AF_{647}). As positive control respective cells were stained with an anti-Miro1 IgG followed by detection with a secondary antibody conjugated to AF_{647} (bottom row. Nuclei were counterstained with DAPI. Scale bar 20 µm.*

The crisp IF detection of Miro1 observed with the $_{biv}M41_{647\_sort}$ and $_{biv}M114_{647\_sort}$ further highlight the influence of labeling strategies on Nb functionality.

3.2.8 Application of bivalent nanotraps for immunoprecipitation of Miro1

The capture efficiency of the bivalent Miro1 nanotraps for Miro1 was analysed. Endogenous Miro1 was immunoprecipitated from cell lysates using either the chemically immobilized monovalent nanotraps ($M41_{NHS}$; $M114_{NHS}$) or the site-directed modified versions ($_{biv}M41_{sort}$;

$_{biv}$M114$_{sort}$). Since more soluble Miro1 had been obtained from HEK293 cells lysed with 1% Triton X-100 buffer (**Figure 18B**), the same conditions were followed.

Immunoblot analysis revealed a significant increase of endogenous Miro1 pulldown with $_{biv}$M41$_{sort}$ and slightly higher enrichment with $_{biv}$M114$_{sort}$. Notably, with both bivalent nanotraps, the amount of precipitated Miro1 was higher compared with the conventional Miro1 antibody used as a positive control (**Figure 24A**).

Further analysis of the IP profile of mono- and bivalent nanotraps (M41$_{NHS}$; M114$_{NHS}$ and $_{biv}$M41$_{sort}$; $_{biv}$M114$_{sort}$) and their potential use for the proteomic characterization of Miro1 by mass-spectrometry analysis was explored. The IP of endogenous Miro1 as previously stated above were performed in three technical replicates, with equal cell number as input material, which allowed for the application of label-free quantification. The mass spectrometry experiment and data analysis were performed by Katharina Zittlau (IFIZ, University of Tuebingen).

After initial validation of the reproducibility between replicates the efficiency of each nanotrap to capture endogenous Miro1 was analysed. Sequence alignment analysis of the eight annotated Miro1 isoforms showed a high level of sequence identity between isoforms (data not shown). In total, 31 “razor” peptides were identified for Miro1 isoform 3 and 30 peptides, including one unique peptide, for isoform 2 (**Figure 24B**). Both bivalent nanotraps, as well as the M114$_{NHS}$ nanotrap, were able to capture isoform 2 in addition to isoform 3. Notably, more Miro1 peptides were identified with a higher sequence coverage in IPs with the bivalent nanotraps compared to their monovalent formats (**Figure 24C**). The enrichment efficiency of Miro1 capture by IP was validated based on intensity based absolute quantification (iBAQ) (**Figure 24D**). Here, the non-specific interaction of about 1760 proteins with bivalent nanotraps was detected which was also observed in the control nanotraps. The high background is suggestive of interactions with the agarose matrix on which the Nbs were immobilized and may be addressed by blocking and stringent washing during the IP experiment. Despite the high background, the highest level of Miro1 isoform 2 and 3 was detected for both bivalent nanotraps. While the M41$_{NHS}$ nanotrap showed low levels of Miro1 enrichment as the controls, M114$_{NHS}$ as well as the bivalent nanotraps demonstrated increased Miro1 capture. Finally, known Miro1 interactors (based on STRING database annotation) were classified by their direct or indirect interaction with Miro1 in combination with the observed confidence score. While all nanotraps showed a clear enrichment of Miro1 compared with the control nanotraps, only the $_{biv}$M114$_{sort}$ allowed for the enrichment of class 1 interactors such as MFN2 or FKBP8 (**Figure 24E**). Notably, none of the known Miro1 interactors in mitochondrial motility or mitophagy were enriched by any of the mono-and bivalent nanotraps.

In summary, these results further reinforce how the performance of Nbs as capture and detection tools can be improved by generating bivalent binding molecules in combination with site-specific functionalization.

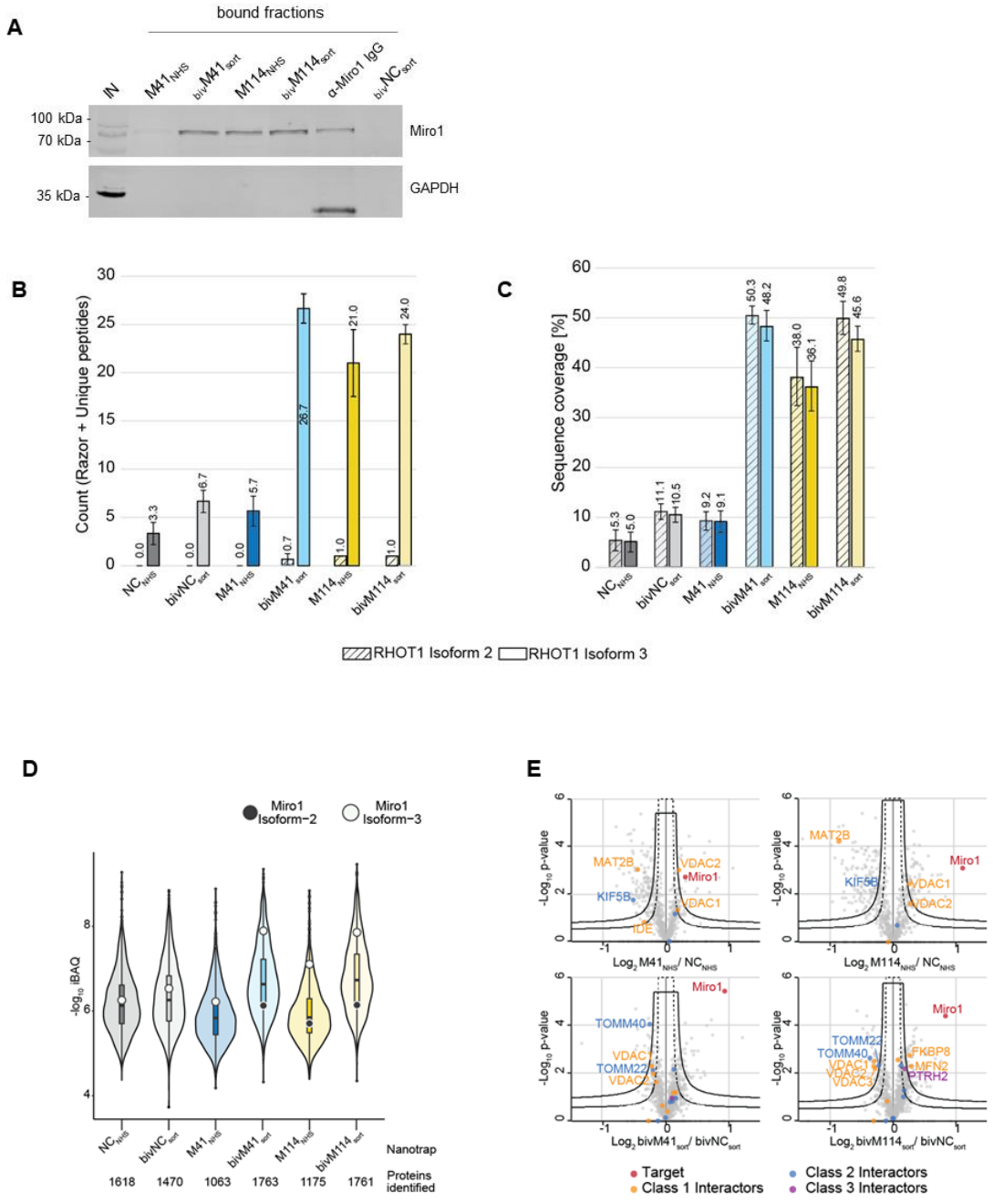

Figure 24. *Proteomic analysis of Miro1 enrichment by Miro1 nanotraps (**A**) For comparable immunoprecipitation soluble protein fraction of HEK293 cells were incubated either with monovalent Nbs either chemically coupled to NHS sepharose ($M41_{NHS}$, $M114_{NHS}$) or the bivalent formats, which were site specifically conjugated to agarose particles by sortagging*

*and click chemistry (bivM41$_{sort}$, bivM114$_{sort}$). Input and bound fractions were analysed with an anti-Miro1 antibody. As positive control anti-Miro1 IgG immobilized on Protein A/G sepharose and as negative control a non-specific bivalent and site specifically conjugated nanotrap ($_{biv}$NC$_{sort}$) was used. Shown is a representative immunoblot stained with an anti-Miro1 antibody. (**B**) Identification of Miro1 (gene name: RHOT1) specific peptides (razor and unique) for both Miro1 isoforms. (**C**) Averaged sequence coverage of Miro1 (gene name: RHOT1) after precipitation with indicated nanotraps. Shown in (**B and C**) are the results from three technical replicates (n = 3) ± S.D. (**D**) Capture efficiency by mono- and bivalent nanotraps. Averaged iBAQ (intensity based absolute quantification) values for Miro1 isoform 2 (white circles) and isoform 3 (black circles) of three biological replicates are shown. (**E**) Classification of Miro1 interactor based on STRING database. Class 1: direct interactor, confidence score >0.9; Class 2: direct interactor, confidence score <0.9; Class 3: indirect interactor, confidence score >0.9. Results from the mass spectrometric analysis were provided by Katharina Zittlau (IFIZ, Tübingen)*

3.2.9 Intracellular characterization of Miro1 Cbs

Cbs are chimeric expression constructs comprising a Nb genetically fused to a fluorescent protein. Their unique advantage is that they can visualize dynamic redistribution and expression levels of endogenous antigens within living cells with spatial and temporal resolution [reviewed in (Wagner and Rothbauer 2021). To analyse the functionality of selected Miro1-Nbs for intracellular targeting and tracing of Miro1 in living cells, they were formatted as Cbs. The Nb-coding sequences were fused via a flexible GS linker to TagRFP in a mammalian expression vector under the control of the CMV promoter (**Figure 25A**). The Cb constructs were transiently expressed either alone or in combination with GFP-Miro1 in HeLa cells. 24 h after transfection the different fluorescent signals derived from the antigen (GFP channel) and of the Cbs (TagRFP channel) were visualized by live-cell fluorescence imaging.

Image analysis revealed a clear relocalization of the M41- , M85- and M114-Cb signals to mitochondrial networks in the presence of GFP-Miro1. All other Miro1-Cbs seem not to bind GFP-Miro1 (**Figure 25B**).

To check for specificity, M41-, M85-, and M114-Cbs were also co-expressed with a control antigen, GFP-PCNA, which is a DNA-binding protein and therefore accumulates strongly in the nucleus (**Figure 25C**). As no enhanced Cb signal was observed in the nucleus upon coexpression of this protein, it can be concluded that the Miro1 Cbs bind neither to GFP nor nonspecifically to the PCNA moiety.

However, in the absence of the exogenously expressed GFP-Miro1 the Cb signals only showed a diffuse cellular distribution and no characteristic mitochondrial structures were seen as they were observed upon an anti-Miro1 antibody staining of Cb expressing cells (**Figure 25D**). These findings suggested that none of the Miro1-Cbs is capable to bind endogenous Miro1.

Additionally, the intracellular binding capacity of M41-, M85- and M114-Cb to the previously identified domains of Miro1 was investigated. The Miro1 domain deletion constructs described previously (**Figure 20A**) were expressed along with the Cb constructs in HeLa cells. Subsequent cellular imaging showed that coexpression with the C-terminal GTPase domain of Miro1 resulted in specific relocalization of M41-, M85- and M114-Cb to the mitochondrial network, confirming the results obtained from pulldown domain mapping for these Cbs. (**Figure 26A-C**).

A

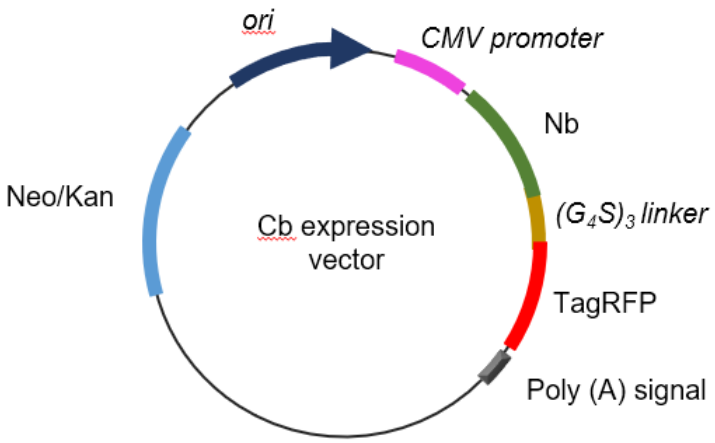

B

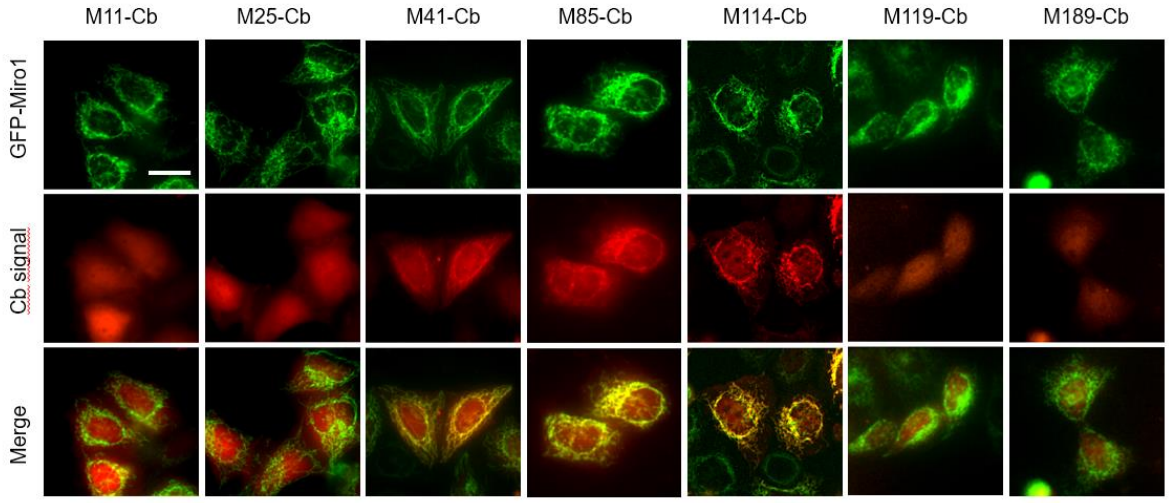

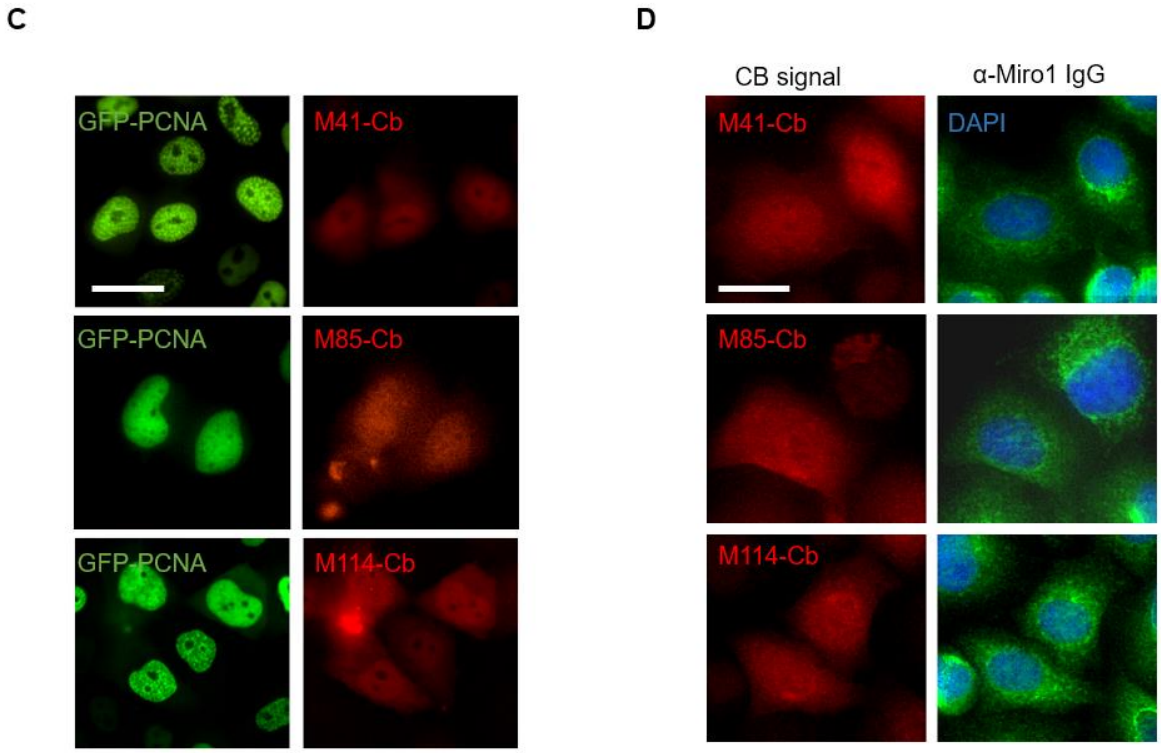

***Figure 25**. Intracellular characterization of Miro1-Cbs (**A**) Vector map of a mammalian Cb expression plasmid (**B**) Representative fluorescence images of living HeLa cells transiently expressing GFP-Miro1 (top row) in combination with red fluorescently labelled (TagRFP) Miro1-Cbs (middle row). Scale bars 20 µm.(**C**) Representative images of living HeLa cells transiently expressing GFP-PCNA (left column) in combination with red fluorescently labelled (TagRFP) M41-,M85- and M114-Cbs (right column) (**D**) Immunofluorescence detection of endogenous Miro1 in HeLa cells expressing M41-, M85- and M114-Cb (left panel) using an anti-Miro1 antibody (right panel). Scale bar 25 µm.*

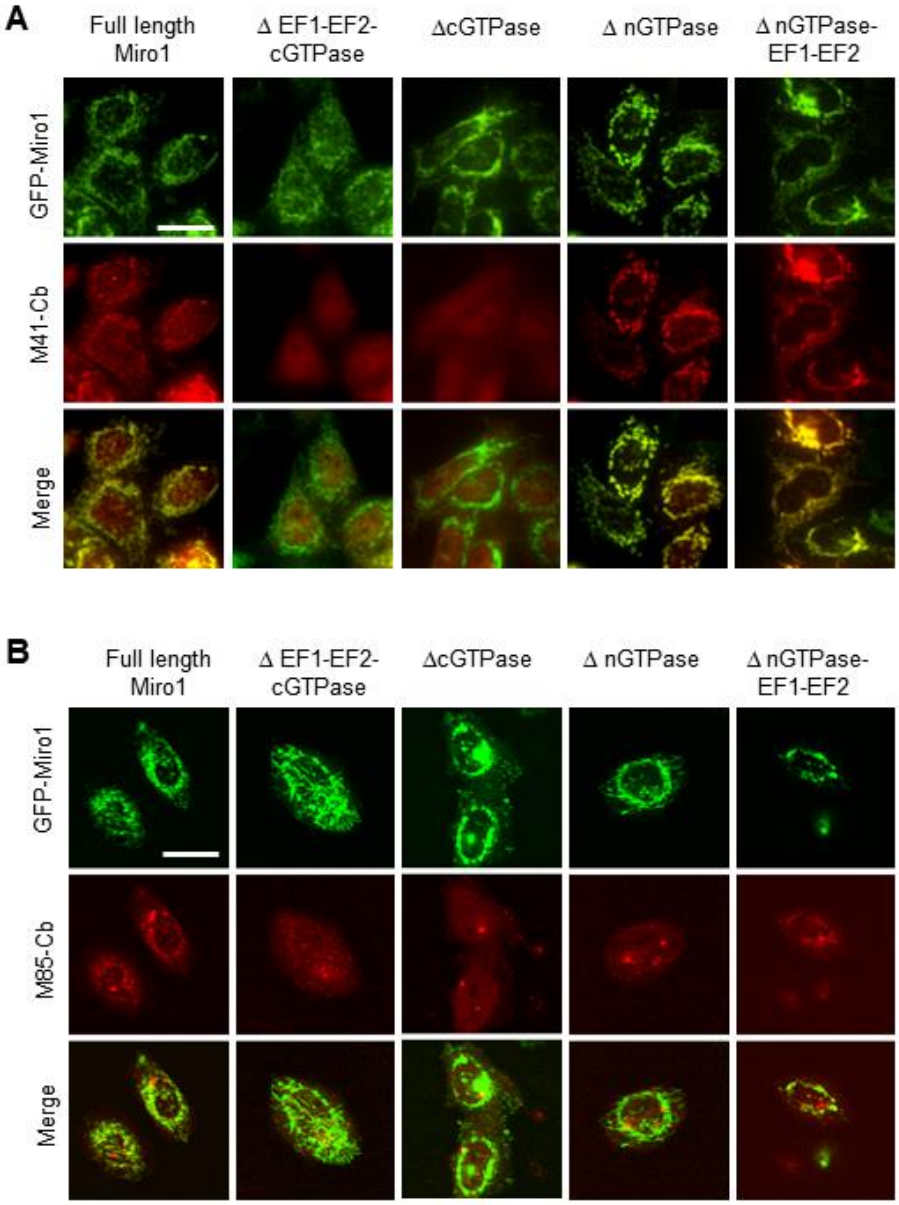
A
Full length Miro1
Δ EF1-EF2-cGTPase
ΔcGTPase
Δ nGTPase
Δ nGTPase-EF1-EF2
GFP-Miro1
M41-Cb
Merge
B
Full length Miro1
Δ EF1-EF2-cGTPase
ΔcGTPase
Δ nGTPase
Δ nGTPase-EF1-EF2
GFP-Miro1
M85-Cb
Merge

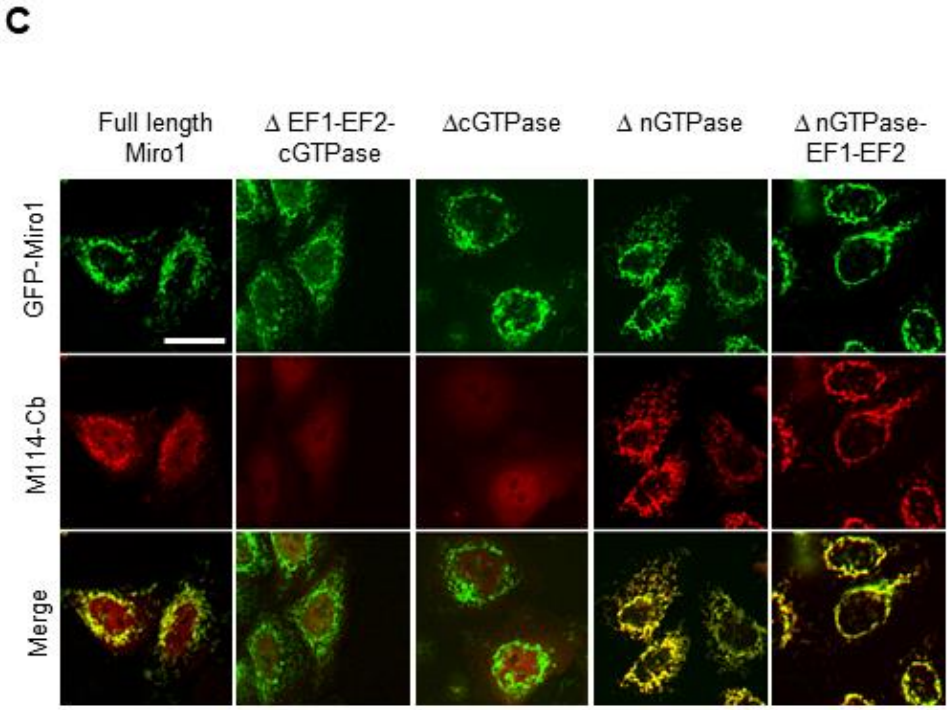

***Figure 26**. Intracellular characterization of domain specific binding of selected Miro1 Cbs. Representative fluorescent images of live HeLa cells transiently expressing GFP-Miro1 and indicated GFP-tagged Miro1 domain deletion constructs (top row) in combination with TagRFP-labelled M41-Cb (**A**), M85-Cb (**B**) or M114-Cb (**C**)*

3.2.10 Miro1-Cbs as biosensors of compound-induced mitochondrial dynamics

From the live cell imaging of HeLa cells expressing Miro1-Cbs, it was observed that M114-Cb shows a slightly better intracellular binding compared to M41- and M85-Cb. Thus, the M114-Cb was selected to further analyse the potential of Cbs to visualize changes in mitochondrial morphology in living cells. To monitor such changes in a targeted approach U2OS cells transiently co-expressing the M114-Cb and GFP-Miro1 were treated with 10 µM Sorafenib or DMSO as control. Sorafenib was previously shown to induce mitochondrial fragmentation and apoptosis in a time-dependent manner (Zhao et al. 2013; Zhang et al. 2017). Using time-lapse imaging, the changes in mitochondrial morphology within single cells were traced over a 2 h period with an imaging interval of 30 min. After the initial 30 min of Sorafenib treatment, images revealed the collapse of the mitochondrial network reflected by gradual disappearance of elongated mitochondria. After 90 min, condensed mitochondrial networks were visible in most treated cells. Both, the Sorafenib induced mitochondrial morphological transitions as well as

normal shape changes observable in the DMSO control were successfully visualized by the M114-Cb (**Figure 27**).

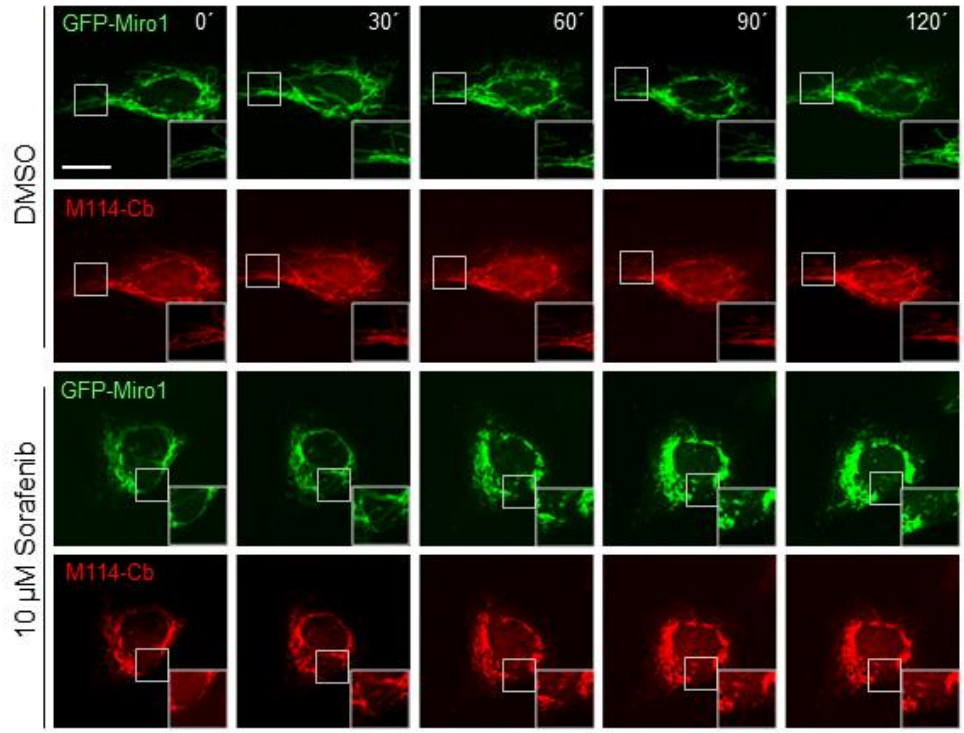

Figure 27*. Visualization of compound-induced mitochondrial dynamics in live cells**. Time-lapse microscopy of U2OS cells transiently expressing GFP-Miro1 in combination with M114-Cb. To visually track morphological mitochondrial changes, cells were treated with either DMSO as a control (top two rows) or 10 µM Sorafenib (bottom two rows) followed by time-lapse imaging over a 2-hour period. Shown are representative images of three independent replicates. Scale bar 25 µm. Squares at the bottom right represent enlargements of the selected image section.*

3.2.11 Selective degradation of Miro1 in living cells

It was previously reported that the depletion of Miro1 in PD patient-derived neurons by induced by treatment with an undisclosed small molecule or genetic silencing rescues mitophagy activation (Hsieh et al. 2019). In recent years, strategies involving the use of Nbs fused with ubiquitin ligases have been applied to induce selective protein knockdown within cells or organisms (Kuo et al. 2011; Bery et al. 2019; Caussinus et al. 2011; Baudisch et al. 2018; Chen et al. 2021). To test whether the selected Miro1-Nbs could also be used to induce targeted degradation of Miro1 in living cells, genetically encoded Miro1-specific degrons were engineered. Therefore the cDNAs encoding for the intracellularly functional Nbs, M41- and M114-, or the GFP-Nb (GBP) used as a non-related Nb for control, were C-terminally fused to

the Fbox protein domain(Bai et al. 1996). For cellular expression these genetically encoded Fbox-Nb constructs were cloned into mammalian expression vectors containing an independently transcribed nuclear TagRFP ($TagRFP_{NLS}$) to facilitate the identification of transfected cells in cellular imaging analysis. In line with previous findings (Caussinus et al. 2011; Moutel et al. 2016; Bery et al. 2019), it was hypothesized that expression and subsequent interaction of Nb degrons at Miro1 would generate a specific loading platform for endogenous components of the mammalian E3 ligase complex, namely SKP1 and Cul1 (**Figure 28**).

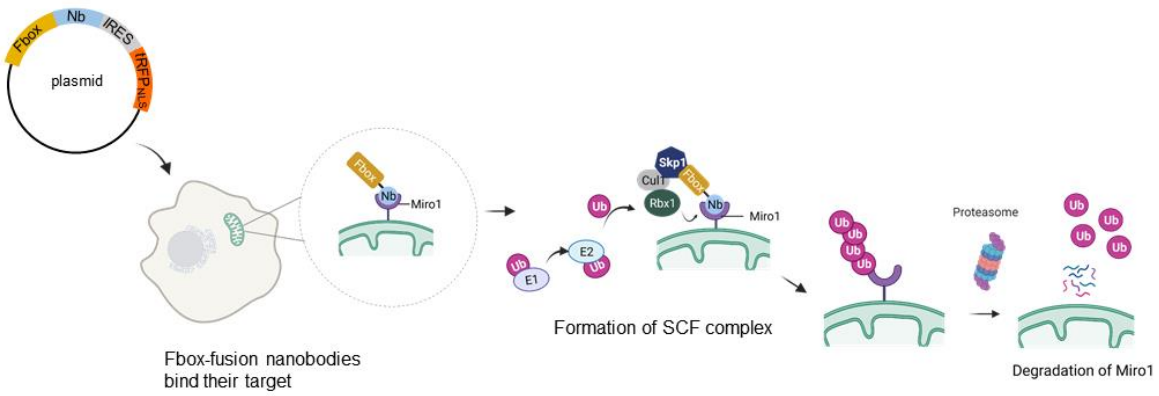

Figure 28. *Targeted intracellular degradation of Miro1 by Fbox-Nbs. Schematic illustration of the targeted degradation of Miro1 mediated by Miro1-Nb degrons. The specific interaction between Fbox-Nbs and Miro1 triggers the recruitment of other components of the SCF E3 ligase complex (Skp1 and Cul1) which mediate the subsequent ubiquitination and proteasomal degradation of the target, Miro1.*

The functionality of the generated Fbox-GBP, Fbox-M41, and Fbox-M114 was first evaluated by examining their binding to transiently co-expressed GFP-Miro1 in HeLa cells. A clear overlap of the Fbox-Nb signal with GFP-Miro1 after IF staining using an anti-V_HH antibody showed that N-terminal fusion of the Fbox domain did not affect intracellular binding of the Nbs (**Figure 29A**). Next, the effects of Fbox-Nb degron expression on cellular Miro1 levels was analysed by quantitative fluorescence microscopy. To quantify the GFP-Miro1 signal in Fbox-Nb expressing cells, an image auto segmentation algorithm was applied as described in section 2.2.3.6 and **Figure 7**. During the image auto segmentation, cells with fluorescence in the far-red channel (Fbox-Nb degron staining) were selected and the corresponding GFP-Miro1 fluorescence levels measured within these cells. Filters were also applied to eliminate

incompletely imaged (e.g., cells at the edge of the imaging field) and dying/dead cells from the quantification. Measurement of the fluorescence intensity of GFP-Miro1 in cells co-expressing the Fbox-Nb constructs revealed ~80% reduction of the GFP signal in cells expressing Fbox-M114, ~50% in cells expressing Fbox-M41, and ~50% in cells expressing Fbox-GBP, respectively. The co-expression of a nonspecific Fbox-Nb (Fbox-NR) resulted only in a non-significant reduction in GFP-Miro1 (**Figure 29B-D**).

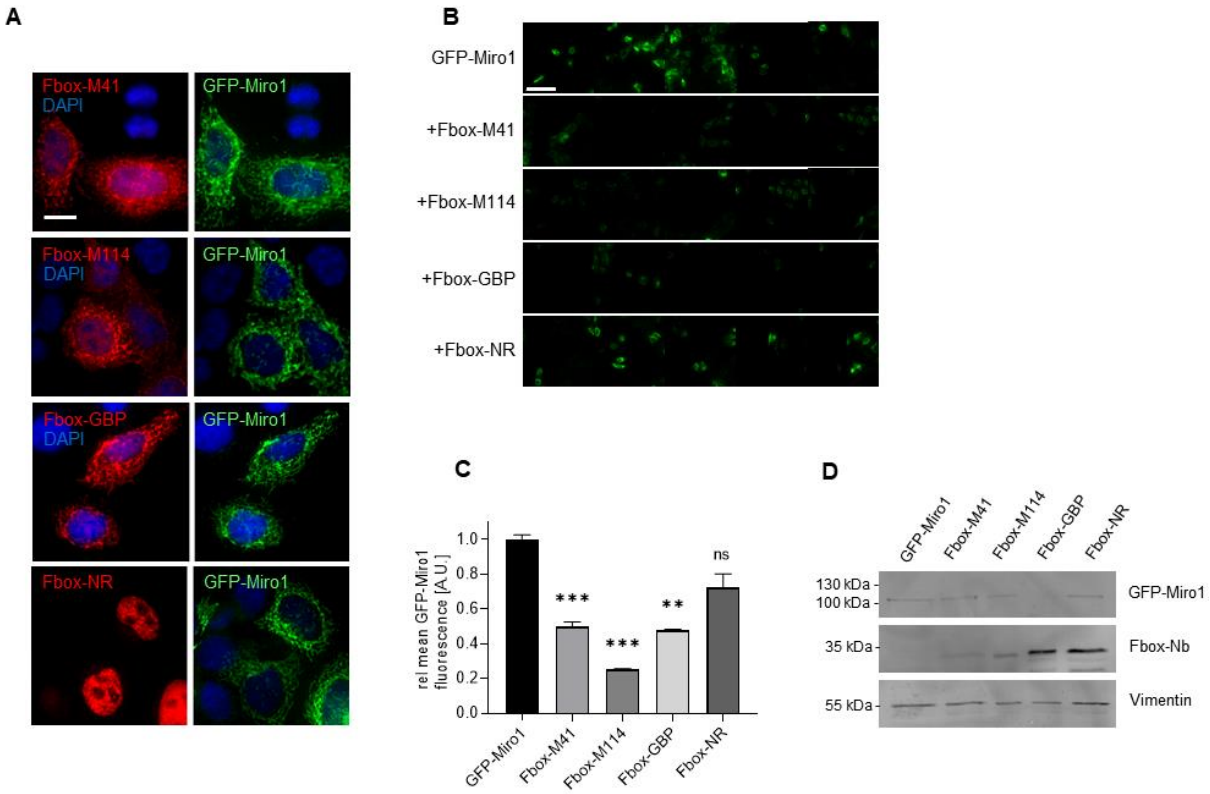

Figure 29. *Targeted degradation of GFP-Miro1 by Fbox-Nb-based degrons in live cells. (A) Representative confocal images of HeLa cells transiently co-expressing GFP-Miro1 and indicated Miro1-specific Fbox-Nbs (Fbox-M41, Fbox-M114) or a non-related Fbox-Nb (Fbox-NR) construct are shown. For quantitative IF analysis, cells were fixed and permeabilized 24 h after transfection followed by staining with Cy5 conjugated anti-VHH antibody and DAPI. Scale bar 20 µm. (B) Representative fluorescence images of HeLa cells coexpressing GFP-Miro1 and Fbox-Nb constructs. Scale bar 100 µm. (C) Mean GFP-Miro1 fluorescence intensity from HeLa cells co-expressing GFP-Miro1 and Fbox-Nbs constructs were determined by quantitative fluorescence imaging. Fluorescence intensity values were calculated from three samples (n= 3; >500 cells) and normalized to the GFP-Miro1 signal intensity (set to 1). Positive control; GFP-specific Fbox-Nb (Fbox-GBP), negative control; non-related Fbox-Nb construct*

*(Fbox-NR). Data are represented as mean ± SEM. For statistical analysis, student's t-test was performed, **p < 0.01, ***p < 0.001. (D) Representative western blot of lysates of HeLa cells expressing either GFP-Miro1 alone or in combination with the indicated Fbox-Nb constructs. For analysis 10 µg of the soluble fractions were subjected to SDS-PAGE and immunoblotting followed by detection using an anti-GFP antibody (GFP-Miro1) and an anti-VHH antibody (Fbox-Nb constructs). As loading control, endogenous vimentin was detected using an anti-Vimentin antibody.*

Although clear relocalization of intracellularly functional Miro1-Nbs (in Cb format) to endogenous Miro1 has not been demonstrated in live cell imaging experiments, the potential of Fbox-Nb degrons to degrade endogenous Miro1 has been investigated. To this end, HeLa cells were transfected with Fbox-Nb constructs and cellular levels of Miro1 after 24 h of expression were determined by quantitative IF imaging using an anti-Miro1 antibody in cells displaying a nuclear TagRFP signal. While image analysis showed characteristic Miro1 staining at mitochondrial structures (**Figure 30A**), quantification of the antibody signals in a statistically relevant number of cells (n>500) showed a ~16% and ~30% decrease in the IF signal upon expression of Fbox-M41 and Fbox-M114, respectively. Notably, expression of the nonspecific Fbox-NR resulted only in a minor reduction of less than ~4% of the Miro1 signal (**Figure 30B**).

Additionally, the role of the proteasome in the Fbox-Nb degron mediated degradation of endogenous Miro1 was investigated. HeLa cells transfected with the Fbox-Nbs were treated with the proteasome inhibitor, MG132 or DMSO as negative control for 16 h. Quantification of Miro1 signaling in cells treated with DMSO showed a repeated decrease in IF signaling of 14% and 31% for Fbox-M41 and Fbox-M114 expression, respectively. These levels are in the same range as previously observed. However, quantified Miro1 fluorescence signals in MG132-treated cells remained at similar levels as untransfected cells (**Figure 30C**), indicating that the proteasome is indeed involved in Nb-degron mediated cellular depletion of Miro1.

Taken together, these findings indicate that both Nb-degrons, Fbox-M41 and Fbox-M114, address endogenous Miro1 in live cells and induce targeted degradation of their antigen through the proteasome.

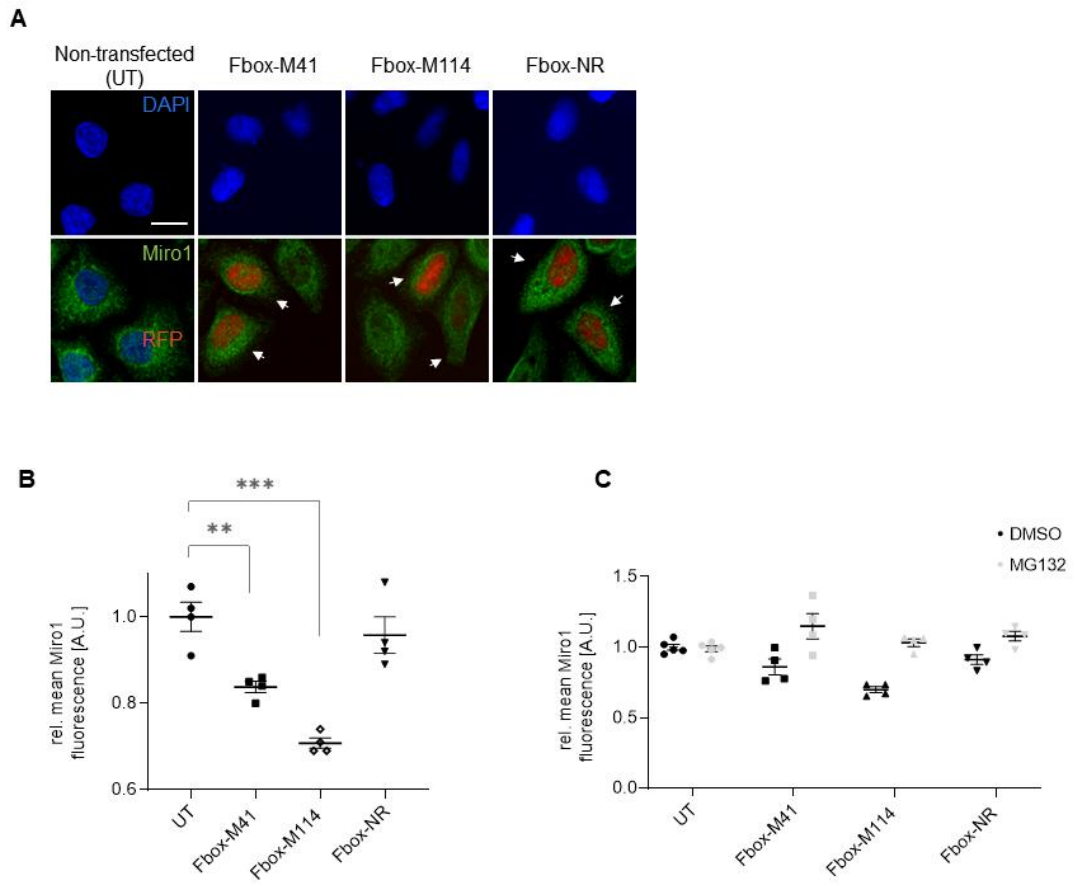

Figure 30. *Targeted intracellular degradation of endogenous Miro1 by Fbox-Nb-based degrons. (**A**) Representative confocal images of HeLa cells transiently expressing indicated Miro1-specific Fbox-Nbs (Fbox-M41, Fbox-M114) or a non-related Fbox-Nb (Fbox-NR) construct. For quantitative IF analysis, cells were fixed and permeabilized 24 h after transfection followed by detection of endogenous Miro1 with Miro1 antibody (shown in green). Fbox-Nb expressing cells were identified by a nuclear TagRFP signal subjected to automated image analysis and quantification as described in section 2.2.3.6. Scale bar 20 µm. (**B**) Mean Miro1 fluorescence intensity from HeLa cells expressing Fbox-Nbs determined by quantitative fluorescence imaging. Mean Miro1 fluorescence was calculated from four samples (N = 4;n > 500 cells) and normalized to untransfected cells, UT (set to 1). As control, a non-related Fbox-Nb construct (Fbox-NR) was used. Data are represented as mean ± SEM. For statistical analysis, student's t-test was performed, **p < 0.01, ***p < 0.001. (**C**) Mean Miro1 fluorescence intensity from HeLa cells expressing Fbox-Nbs or non-related control, Fbox-NR after 16 h treatment with DMSO or 150 nM MG132 determined by quantitative fluorescence imaging. Mean Miro1 fluorescence was calculated and normalized to untransfected cells, UT (set to 1).*

3.3 DRP1-specific Nbs

Unlike Miro1 which is anchored in the MOM, the second protein of interest in this study, DRP1 is cytosolic and only recruited to mitochondria at the initiation of fission. The key roles played by DRP1 in mitochondrial fission and apoptosis as well as its implication in neurodegenerative disorders (detailed in Chapter 1) warrant further study. Therefore, the second part of this thesis is aimed at the selection and application of Nbs as research tools to address the mechanoenzyme, DRP1. To accomplish this aim, the generated DRP1 Nb-phage library (from section 3.1.3) was subjected to iterative biopanning, specific DRP1-binding Nbs were selected, characterized and used for different applications. This section describes the steps taken and the results obtained.

3.3.1 Selection of DRP1-specific Nbs by phage display.

DRP1-Nb-phage library was generated as previously described for the Miro1-Nb phage library For biopanning, phage particles expressing Nbs as pIII fusions were produced from the library and screened against purified DRP1 or GFP as a control antigen. Applying the same protocol as for Miro1, two iterative biopanning rounds were performed. In each round, 4 preclearing steps to deplete non-specific binding phages were included by panning the phages against purified GFP. After the first panning round, 96-fold enrichment of bound phages relative to the control was observed which increased to 323-fold by the end of the second panning round as shown in **Table 20**.

***Table 20**. Enrichment of DRP1 Nb-phages during biopanning against purified DRP1*

Panning round	Phage input	Eluted phages(DRP1)	Eluted phages (control)
1	1.0×10^{12}	5.3×10^{3}	5.5×10^{1}
2	1.0×10^{11}	5.5×10^{7}	1.7×10^{5}

Despite the high titers of phages binding nonspecifically to GFP in the second round of biopanning, the increased enrichment ratio of DRP1-binding phages was sufficient to proceed to the next screening step. The specificities of enriched Nb-phage clones from the second panning sub-library were then tested by phage ELISA.

In total, 260 single clones were selected from the plated sub-library and monoclonal phage supernatants produced in 96 deep-well plates. Purified DRP1 and GFP were passively adsorbed on 96-well MaxiSorp™ plates and the binding of monoclonal phages detected with

a HRP-conjugated anti-M13 antibody. Phages binding to DRP1 with greater than 200% signal intensity than the control antigen were identified (**Figure 31**).

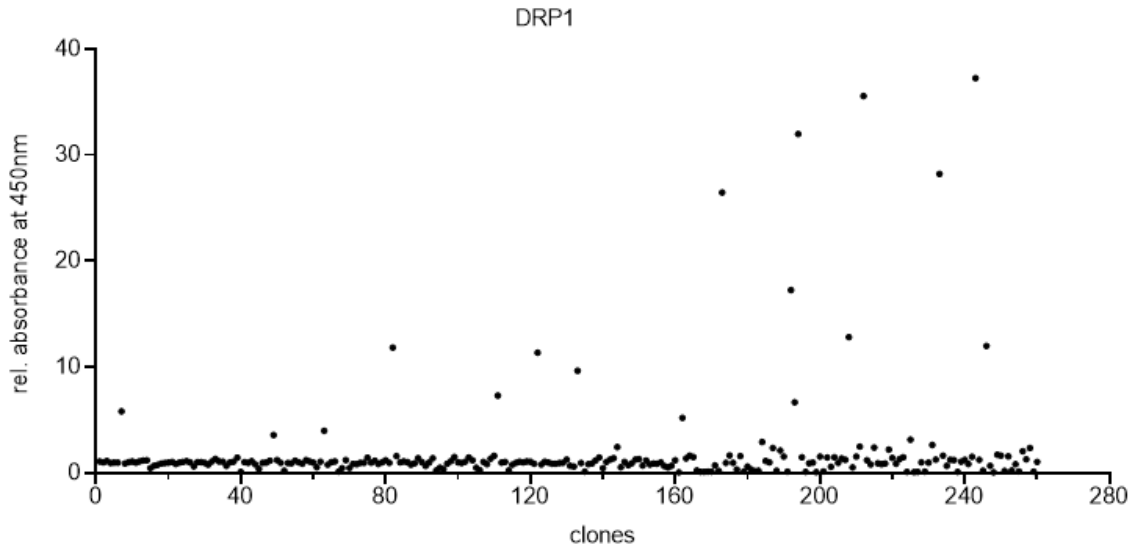

Figure 31*. Phage ELISA profile of phage clones tested for binding to DRP1. Signal intensities were normalized to the signal obtained for binding to the control antigen, GFP.*

In total, 27 positive binding Nb-phages were selected from the phage ELISA. Subsequently plasmid preparations were carried out for all selected clones and subjected to Sanger sequencing

3.3.2 Sequence characterisation of DRP1-specific Nbs

Genetic sequence analysis of the 27 positive binders was performed and eight unique Nbs named D7, D49. D63, D187. D193, D219, D246 and D258, were identified. Redundant sequences were identified from the panning sub-library which could be attributed to the enrichment of identical Nbs during this process and to a lesser extent, the complexity of the DRP1 library (see **Table 15**). All eight DRP1-Nbs were aligned according to the Kabat numbering system (Kabat and Wu 1991) for comparison of their framework and hypervariable regions. (**Figure 32**). As expected, the Nbs possessed high sequence similarity in their framework regions. The Nbs however showed variations in their hallmark residues within the FR2 region at positions 37, 44, 45 and 47 (in red letters). Here, hydrophobic amino acids were found at the hallmark positions 44 and 45 in the sequences of D49 and D219 which are characteristic of conventional V_H domains.

Variations were observed in the CDRs with CDR3 loops ranging between 11 and 15 amino acids in length. Apart from the conserved cysteine residues in the FR1 and FR3 regions, no additional cysteine residues were present in the CDRs.

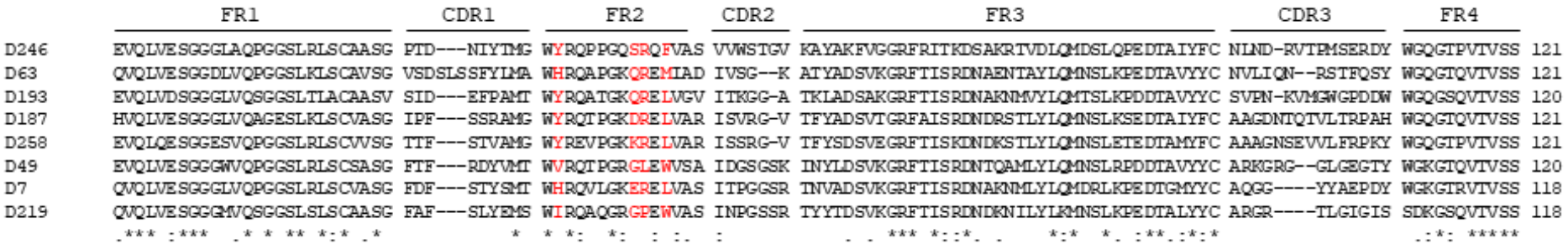

Figure 32. *Genetic characterization of DRP1-Nbs. Amino acid sequence alignment of DRP1-Nbs showing residues in the framework regions (FR) and the CDRs. The hallmark residues characteristic of V_HH or VH sequences are highlighted in red. * (asterisk) indicates positions which have a fully conserved residue, : (colon) indicates positions with residues possessing similar properties, .(dot) indicates positions with residues with weakly similar properties.*

3.3.3 Nb screening by Protein ELISA

Next, the selected DRP1-Nbs were screened for binding by protein ELISA. For expression without the pIII phage coat protein,the Nb coding sequences were shuttled from the pHEN4C phagemid vector into the pHEN6C vector by restriction cloning for efficient periplasmic expression in *E.coli* XL1 cells. After sequencing to ensure correct insertion and sequence integrity, the plasmids were transformed into *E.coli* XL1, cultured and periplasmic extracts (PPE) were prepared. The Nbs in a 1:5 dilution of the PPE were analysed for binding to DRP1 or a control antigen (**Figure 33**). Only D7 and D63 demonstrated significant binding to DRP1 compared with the control, GFP. The non-interaction of the other selected Nbs with DRP1 in this screen is suggestive of a possible involvement of the phage coat pIII protein in the conformation and exposure of the Nb paratope to DRP1. Therefore, only D7 and D63 were further characterized.

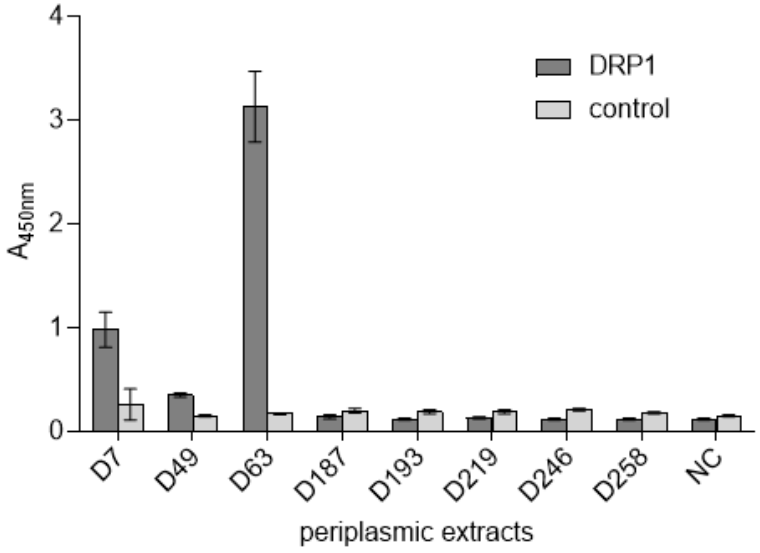

Figure 33. *Protein ELISA screen for reactivities of selected Nbs derived from E.coli XL1 periplasmic extracts against DRP1 (1 µg/ well). Bound Nbs were detected using an anti-VHH antibody labelled with horse radish peroxidase (N=3).*

3.3.4 Expression and purification of D7 and D63-Nbs

For further characterization and proposed applications, D7 and D63-Nbs were expressed in *E.coli* and purified using the workflow for the production of Miro1-Nbs as reported in section 3.2.4. After SEC, the Nbs were concentrated, and a final purity assessment was done by SDS

analysis of 2 µg of each Nb (**Figure 34**). Yields of ~13 mg and ~17 mg were obtained from 1L expression cultures of D7 and D63 respectively.

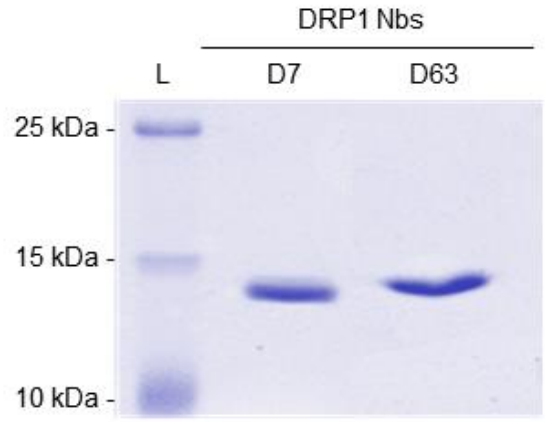

***Figure 34**. Recombinant expression and purification of DRP1-Nbs. SDS-PAGE analysis of 2 µg of purified D7- and D63-Nbs.*

3.3.5 Biochemical characterization of DRP1-Nbs

For the study and targeting of DRP1 using D7- and D63-Nbs as effective tools, there is a need for a comprehensive characterization of the nature of the binding interactions between both ligands and their target. In this section, the kinetics of their interaction with DRP1, the functionality of both Nbs for the immunoprecipitation of DRP1 and the domains being targeted by each Nb and will be elucidated.

3.3.5.1 Binding affinity measurements

The binding affinities of the selected DRP1-Nbs were determined by biolayer interferometry (BLI) applying the similar protocols as used for Miro1-Nbs. Briefly, DRP1-Nbs were biotinylated and immobilized on streptavidin biosensors. The binding kinetics were then quantified by loading different concentrations of DRP1. The data were analysed using a 1:1 ligand-binding model and global fitting. The association and dissociation profiles of D7 and D63 with concentrations of DRP1 as well as the fitted curves are represented as sensorgrams in **Figure 35A** and **35B** respectively. Both Nbs demonstrated high affinity for DRP1 in the low nanomolar range with K_D values of 3.5 nM and 1.8 nM measured for D7 and D63 respectively. Though a faster association rate of 1.25×10^5 M^{-1} s^{-1} was determined for D63, its interaction with DRP1

also showed the faster dissociation rate of the two Nbs. The quantified kinetic parameters with their corresponding coefficients of determination are summarized in **Table 21**

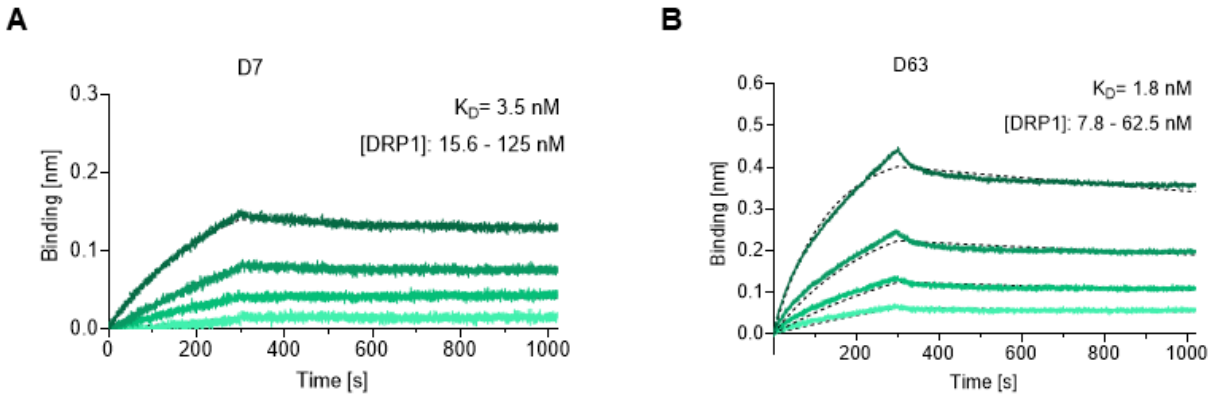

***Figure 35**. Binding affinities of DRP1 specific Nbs. Affinity measurements by BLI of DRP1 at concentrations ranging from 7.8 nM to 125 nM on immobilized (A) D7 (B) D63. The concentrations of DRP1 (from low to high) are illustrated with increasingly darker shades and the global 1:1 fits are illustrated as dashed lines. The binding affinity measurements for D7 and D63 were performed by Teresa Wagner (NMI, Reutlingen).*

***Table 21**. Summary of affinities (K_D), association (k_{ON}) and dissociation constants (k_{OFF}) and the coefficient of determination (R^2) determined for D7- and D63-Nb by biolayer interferometry.*

	K_D (nM)	**k_{ON} (10^5 M^{-1} s^{-1})**	**k_{OFF} (10^{-4} s^{-1})**	**R^2**
D7	3.5	0.34 ± 0.00	1.17 ± 0.02	0.99
D63	1.8	1.25 ± 0.01	2.27 ± 0.01	0.99

In summary, the results from the binding affinity measurements revealed that D7 and D63 bind their target antigen with high affinities in the low nanomolar range.

3.3.5.2 Functional characterization of DRP1-Nbs

One of the significant aims of this project involves the investigation of the role of DRP1 and its interaction partners during apoptosis using immunoprecipitation and immunofluorescence studies. To determine the functionality of the selected DRP1-Nbs for immunoprecipitation, the

purified Nbs were covalently coupled to N-hydroxysuccinimide (NHS)-activated agarose particles thereby generating DRP1-nanotraps.

The capacity of the nanotraps to specifically immunoprecipitate DRP1 was directly tested. HEK293 cells were lysed, and a soluble fraction of the total cell lysate obtained by centrifugation. The soluble fractions were then subjected to immunoprecipitation with D7 and D63 nanotraps. Immunoblot analysis of input, non-bound and bound fractions revealed that both nanotraps efficiently precipitated endogenous DRP1 exhibiting pulldown efficiencies which were comparable to those obtained with a conventional anti-DRP1 antibody. Notably, DRP1 was detectable in the unbound fractions of both DRP1 nanotraps and the positive control. This could be attributed to a saturation of all immobilized Nb or conventional antibody molecules. DRP1 enrichment could be improved by using more of the nanotraps or antibody immunocomplexes for IP. No unspecific binding of endogenous GAPDH to any of the DRP1 nanotraps was detected. The specificity of the nanotraps for DRP1 was further confirmed by the non-interaction of a non-related nanotrap (NC) with DRP1 (**Figure 36**). These findings showed, that both D7 and D63 can bind their epitopes within endogenous DRP1.

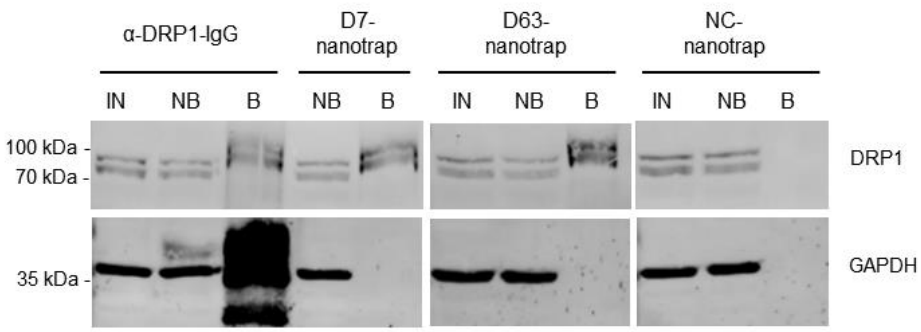

***Figure 36**. Immunoprecipitation of endogenous DRP1**.** After lysis, the soluble protein fraction of HEK293 cells was adjusted to 2 mg/ml and incubated with equal amounts of DRP1 nanotraps. Input (IN, 1% of total), Non-bound(NB, 1% of total) and bound (B, 20% of total) fractions were subjected to SDS-PAGE followed by immunoblot analysis. As positive control anti-DRP1 IgG immobilized on Protein A/G sepharose and as negative control a non-specific (NC) nanotrap was used. Upper parts of the blots were detected with anti-DRP1 antibody. Detection of GAPDH with an anti-GAPDH antibody was used as lysis and loading control. The thick band visible in the bound fraction of the anti-DRP1 IgG is IgG shedding from Protein A/G beads.*

When the selected DRP1-Nbs were applied for immunofluorescence staining of both endogenous and GFP-DRP1 in fixed and permeabilized cells, there was no detection of DRP1 (data not shown) despite testing different fixation or permeabilization methods. These observations suggest that the epitopes of DRP1 may not be accessible to the Nbs under fixation conditions. It was also possible that the binding characteristics of both D7 and D63 were not optimal for their use as affinity detection reagents in immunofluorescence.

3.3.5.3 Domain binding characteristics of DRP1-Nbs

The results obtained from the binding affinity and IP studies so far demonstrate that DRP1-Nbs bind to both recombinant and endogenous DRP1. These data however do not provide information on which domains of DRP1 are involved in the interactions with D7 and D63-Nbs. Domain mapping studies were therefore done by generating DRP1 domain deletion constructs fused C-terminally to GFP (**Figure 37A**). After sequence validation, the deletion constructs were transiently expressed in HEK293 cells. Using the DRP1 nanotraps, pull down studies were performed according to previously stated protocol. Analysis of the bound fractions revealed that both D7 and D63 specifically recognize epitopes within the GTPase effector domain (GED) (**Figure 37B**). The low levels of GFP-tagged GED enriched by the traps may be indicative of the effect of conformational stability of the domain on exposed epitopes when expressed alone.

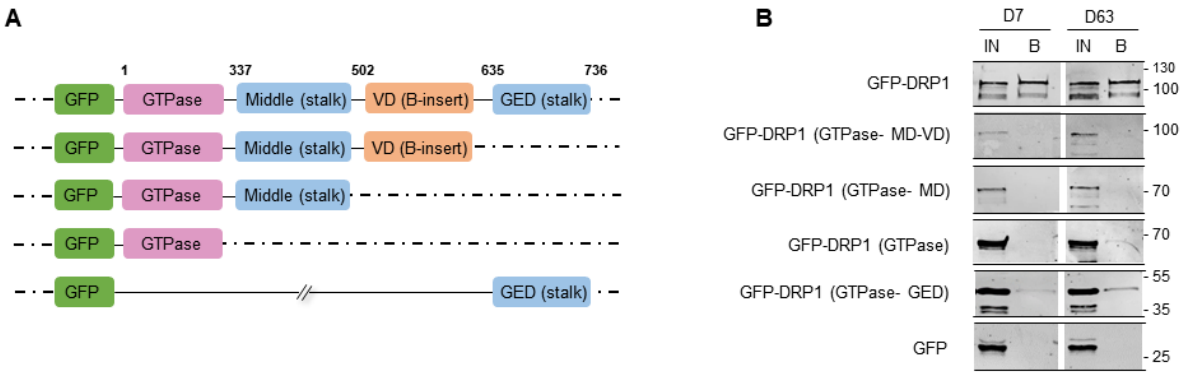

***Figure 37**. Domain mapping of DRP1-Nbs. (**A**) Schematic illustration of GFP-labelled DRP1 deletion constructs and domains used for domain specific binding studies. (**B**) Soluble protein fractions of HEK293 cells transiently expressing constructs in (A) were subjected to immunoprecipitation with D7 and D63 nanotraps followed by western blot analysis of input (IN) and bound fractions with an anti-GFP antibody.*

3.3.6 Intracellular characterization of DRP1-Cbs

Though DRP1 is primarily localized in the cytosol, it translocates to mitochondria and peroxisomes to mediate fission. DRP1-Nbs were formatted as Cbs in a bid to develop intracellular biosensors of DRP1-mediated fission events. D7 and D63 sequences were therefore fused N-terminally to TagRFP in the mammalian expression vector shown in **Figure 25A**. To investigate the intracellular expression and binding of the generated constructs, HeLa cells were transiently transfected with D7-Cb or D63-Cb alone or with GFP-DRP1. When expressed alone, both Cbs were well expressed and distributed throughout the entire cell including the nucleus (**Figure 38A,** left panel). The distribution pattern of both Cbs were not similar to endogenous DRP1 localization obtained with anti-DRP1 antibody staining (**Figure 38A**. bottom row). With GFP-DRP1 coexpression, image analysis revealed that the Cb signals did not relocalize to the cytosol along with their ectopically expressed target (**Figure 38B**, right panel). Based on the results obtained, it was difficult to prove the existence of affinity interactions between the Cbs and DRP1 within the intracellular environment.

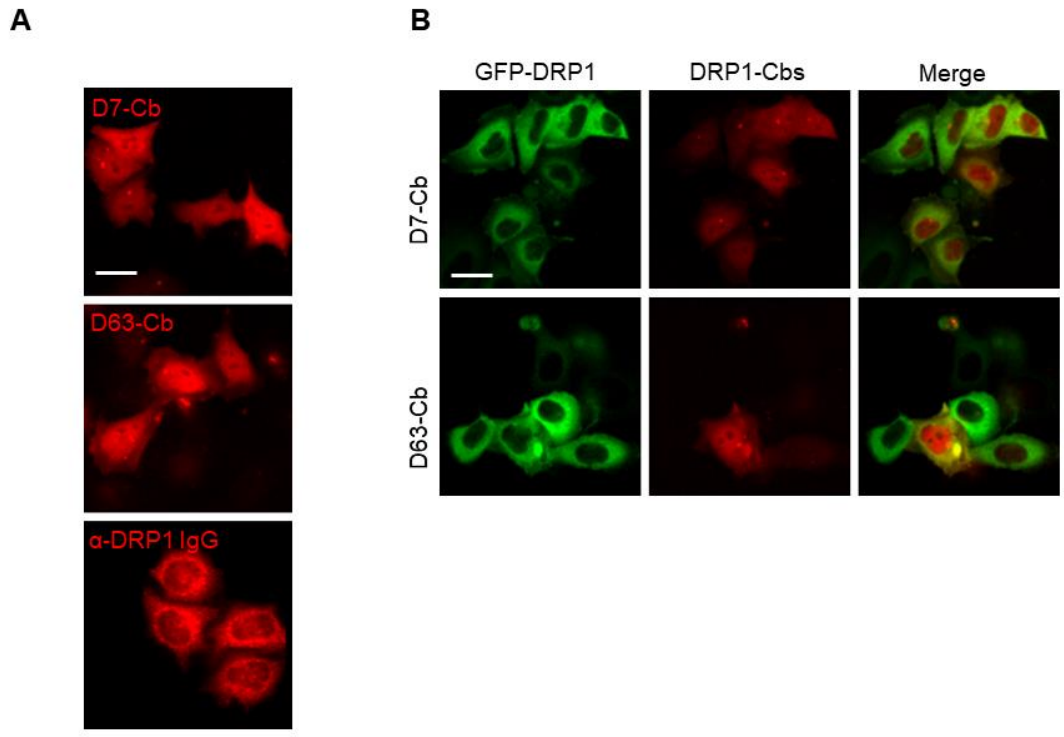

***Figure 38**. Intracellular characterization of DRP1-Cbs. Representative fluorescence images of living HeLa cells transiently expressing DRP1-Cbs (left column) alone (**A**) or in combination with GFP-DRP1 (**B**). Immunofluorescence detection of endogenous DRP1 in HeLa cells (bottom row) using an anti-DRP1 antibody. Scale bars 20 µm.*

To investigate whether the D7 and D63-Cbs recognize and bind DRP1, an additional biochemical assay was utilized. In this previously described assay termed intracellular immunoprecipitation (IC-IP)(Traenkle et al. 2020), the Cbs were expressed in HEK293 cells, and the cells were lysed using non-denaturing buffer conditions. The Cbs were then immunoprecipitated using its fluorescent moiety, TagRFP as an affinity tag. Interactions with the intracellular target was investigated by Western blot analysis of the bound fractions using both Cb and target-specific antibodies. **Figure 39** shows the analyses of the input, non-bound and bound fractions of the IC-IP of D7, D63 and a non-related Cb (NC) after immunoblotting with antibodies against DRP1, TagRFP and GAPDH. The enrichment of endogenous DRP1 in the bound fractions along with D7 and D63-Cbs demonstrate that both Cbs bind to DRP1 in live cells. The non-interaction of both Cbs with endogenous GAPDH further confirmed their specificity for DRP1.

Nonetheless, since the D7- and D63-Cbs could not visualize endogenous or exogenous DRP1 in live cells, they were unsuitable for further live cell imaging applications.

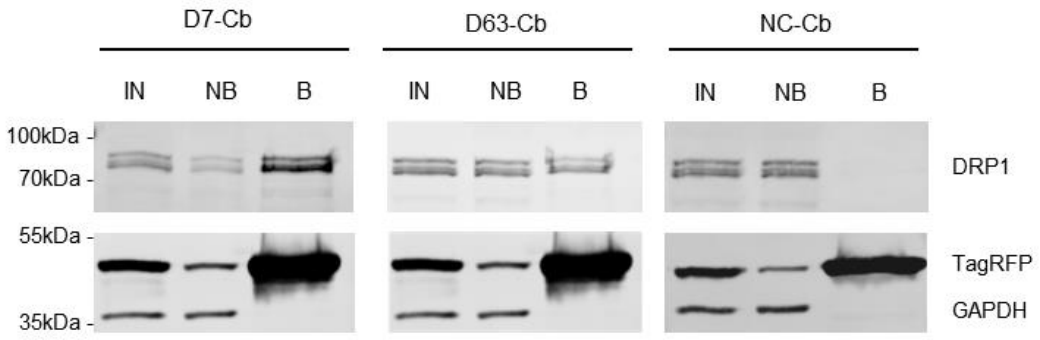

***Figure 39**. Intracellular immunoprecipitation of endogenous DRP1 with DRP1-Cbs. Soluble fractions from lysates of HEK293 cells expressing D7-Cb, D63-Cb and a non-related Cb (NC) were subjected to immunoprecipitation using the TagRFP-Trap™. Input (IN, 1% of total), Non-bound (NB, 1% of total) and bound (B, 20% of total) fractions were subjected to SDS-PAGE followed by immunoblot analysis. Upper parts of the blots were detected with anti-DRP1 antibody. Lower parts of the blots were detected with anti-TagRFP and anti-GAPDH antibodies.*

4 DISCUSSION

Mitochondria associated proteins involved in mitophagy, and mitochondrial fission are critical for the regulation of cellular homeostasis. The characterization of such proteins has many potential benefits in understanding mitochondrial functions as well as the development of novel therapies addressing mitochondria-related disorders.

The role played by Miro1 in the development and progression of Parkinson's disease and amyotrophic lateral sclerosis has been continuously investigated (Zhang et al. 2015; Nguyen et al. 2021; López-Doménech et al. 2021). Extensive research has suggested the possible involvement of DRP1 in abnormal mitochondrial dynamics in neurodegenerative diseases such as Huntington's, Alzheimer's, and Multiple Sclerosis (Reddy et al. 2011; Luo et al. 2017; Roe and Qi 2018; Oliver and Reddy 2019). The pathological significance of both Miro1 and DRP1 in these neurological disorders further underscores the need for new methods and tools to study them in detail at the molecular level.

Over the years, different approaches to study and modulate mitochondrial proteins and processes have been established. For visualization of mitochondrial morphology and dynamics, mitochondrial dyes and stains are often used (Glancy 2020). Recently, the labelling of mitochondrial proteins using photocatalytic reactions in live cells was reported (Wang et al. 2021). However, such approaches could be cytotoxic and involve a risk of off-target effects due to their lack of substrate specificity. These limitations may be avoided by using target-specific reagents. A significant class of such binders are antibodies and antibody domains. Single domain antibodies, also known as nanobodies, are the variable antigen binding domains of heavy chain-only antibodies found in camelids. The characteristics of Nbs such as their relatively small size (~15 kDa), physicochemical stability and high solubility (Arbabi Ghahroudi et al. 1997) make them worthy alternatives to conventional antibodies. These characteristics further enhance the versatility of Nbs which makes them useful tools for applications in diverse research settings.

In this dissertation, nanobodies against the MOM-proteins, Miro1 and DRP1 were generated as affinity tools for the study and characterization of their targets in biochemical assays and intracellular applications. Two Nb libraries encoding the immune repertoire of two alpacas were constructed who were either immunized with Miro1 or DRP1 respectively. The libraries were cloned into phagemid vectors for phage display-based screening and selection. 7 Miro1- and 2 DRP1-specific Nbs were identified and produced with high yields in bacteria. These Nbs demonstrated high binding affinity in the lower nanomolar range and could recognize distinct domains within their targets.

To test the applicability of the Miro1-Nbs, they were screened for their performance as affinity capture tools and as labelling probes for fluorescence imaging. The initial observation that the Miro1-Nbs in their monovalent format were not suitable as primary probes for the visualization and immunoprecipitation of endogenous Miro1 led to the reformatting of two of the promising candidates, M41 and M114 into bivalent Nbs. For these optimized binding molecules, site-specific functionalization strategies via sortase tagging in combination with click chemistry was used which resulted in improved capture and detection of Miro1 in proteomic and IF experiments. For the intracellular visualization and monitoring of Miro1 in live cells, the intracellular functionality of the Nbs after genetic functionalization as Cbs, were tested. Despite the lack of visualization of endogenous Miro1 by M41- and M114-Cbs, M114-Cb showed functionality as an intracellular biosensor of mitochondrial shape transitions due to its interaction with GFP-Miro1 in live cells. The intracellular functionality of M41 and M114-Nbs as led to the generation of Miro1 degrons by fusion to Fbox protein domains with which the targeted degradation of Miro1 in live cells was performed.
The selected DRP1-specific Nbs, D7 and D63 when reformatted as nanotraps, demonstrated functionality as affinity capture tools for endogenous DRP1. However, despite their high affinity and potential for the proteomic characterization of endogenous DRP1, D7 and D63 were not applicable for immunofluorescence or live cell imaging studies of DRP1.

The results obtained from this study and implications for the structural and functional characterization of Miro1 and DRP1 will be discussed in the following sections.

4.1 Selection of Miro1- and DRP1-specific Nbs

Highly functional Nbs have been selected from naïve, synthetic and immune libraries. Despite the high sequence diversity obtainable with naïve libraries, a high affinity target-specific binder may not be found. Also, the construction and validation of synthetic libraries can be time consuming and expensive (Muyldermans 2021). To avoid these challenges, immune Nb libraries were constructed in this study. This choice was based on the knowledge that Nbs raised *in vivo* by immunization with properly folded proteins tend to recognize conformational epitopes on their antigens making them ideal tools for diverse applications (Pardon et al. 2014).

The presentation of Miro1 and DRP1 in an antigenic format successfully produced a hcAb-specific immune response after 13 weeks of immunization. On cloning the immune repertoire of both animals into phage display vectors, Miro1 and DRP1 Nb-phage libraries comprising 1.5×10^7 and 2.3×10^7 clones were established respectively. The sizes of these libraries fell within

prescribed limits (Pardon et al. 2014; Muyldermans 2021). Though quality checks by colony PCR showed 100% insertion rate of Nb sequences in the randomly selected clones from both libraries, there were only 83% and 57% unique and intact Nb sequences in the selected clones from the Miro1 and DRP1 libraries respectively. For the DRP1 library, repetitive sequences were common and to a lesser extent, frame shifts, and mid-sequence stop codons accounted for truncated Nb sequences. It is significant to note here that only 30 clones were sequenced from each library which represented a negligible fraction of the total population. A better alternative would be next generation sequencing (NGS) which is a rapid and efficient method to assess library diversity and quality. The large number of sequencing reads obtainable can provide insight into the robustness of the library construction protocol (Deschaght et al. 2017).

The Nbs described in this thesis were selected from the generated libraries by phage display technology. Over the years, parameters used in phage display-based screens such as antigen and antigen presentation methods, have been optimized to increase the propensity of enriching more affine binders (Colazet and Chames 2018). Passive antigen adsorption which was used for the Miro1 and DRP1 panning rounds is straightforward and does not rely on protein modification. However, it requires the exposure of hydrophobic interfaces within the antigen towards the polystyrene surface of the immunotubes which can lead to conformational changes. Consequently, some binders selected on adsorbed proteins may not be able to bind the soluble conformation of the antigen (Butler et al. 1992; Colazet and Chames 2018) which may explain the non-recognition of endogenous Miro1 and DRP1 by some of the selected Nbs. Therefore, in the second year of this project, the Miro1 library was rescreened for binders using a different antigen source and immobilization strategy. GFP-Miro1 expressed in HEK293T cells was used for biopanning and subsequent selection steps. Affinity based immobilization was used to tether the GFP moiety in the protein to a ligand covalently attached to polystyrene. With this approach, the challenges arising due to the unstable nature of purified full length Miro1 were avoided. Also, within the context of the project, there was a need to select Nbs which could bind the natively folded antigen. 3 biopanning rounds were performed which yielded low enrichment ratios of positive to non-specific binding phages. Unfortunately, extensive preclearing with lysates containing host cell proteins or over-expressed GFP seemed minimal in preventing the enrichment of nonspecific binders (see **Table 17**). The poor enrichment ratios between positive and non-binders when using crude antigens for biopanning is however not unusual (Schmidthals 2013; Lim et al. 2019).

Recently, the benefits of Nb library screening by biopanning in combination with NGS approaches have been highlighted (Deschaght et al. 2017). In addition to the *in-silico* identification of potential binders which may not be experimentally enriched for reasons such

as error in Nb-pIII assembly, display of Nbs toxic to *E. coli* or other reasons limiting the packaging of potential specific Nb-phages during iterative biopanning rounds, NGS screening of Nb-phage libraries can also validate the biopanning protocol used. In this study, the Miro1 Nb phage library as well as the sub-libraries after each biopanning round against Miro1 (1-592) were subjected to high-throughput sequencing. The increase in sequence frequency of the 4 selected Nbs after each biopanning round attested to their expected enrichment as bound phages. Notably, other Nbs were identified from the NGS results which demonstrated better enrichment over the panning rounds but were not picked as clones during selection. If no functional Miro1-specific Nb had been identified by conventional biopanning, these Nbs would have been further investigated.

4.2 Functional tests for the characterization of selected Nbs

Initial screening of the selected Nbs using *E.coli* periplasmic extracts helped to save time and purification costs whilst identifying the non-functional Nbs at the protein level. In the case of the DRP1-Nbs, only the D7 and D63 which retained their binding after pIII cleavage. Further biochemical characterization of Miro1 and DRP1-Nbs after purification revealed a collection of high affinity Nbs.

Considering the overall aim of generating specific Nbs which could function as tools for the structural and functional characterization of the antigens in relevant settings, functional tests were of utmost significance.

4.2.1 Functional characteristics of Miro1-Nbs

Initial screens for the performance of Miro1-Nbs as affinity capture tools for proteomics were performed. The results however drew attention to the disparities in binding of the Nbs to ectopic and endogenous Miro1. For instance, M11, 25 and M85 could enrich ectopic Miro1 but not the endogenous protein. A deciding factor may be the relatively low levels of soluble endogenous Miro1. However, considering that other Nbs M114, M119 and M189 could pull down both ectopic and endogenous Miro1, it can be hypothesized that the binding properties of M11, M25 and M85 under the test conditions may not have been optimal for enrichment of endogenous Miro1 by IP.

Further functional tests to assess the utility of Miro1-Nbs as primary binding molecules in IF revealed no detection of endogenous Miro1 although M11, M25 and M41 showed binding to the ectopic antigen in these assays. Since fixation and permeabilization methods may affect the accessibility of Miro1 epitopes for binding (Im et al. 2019) by the Nbs, different fixation methods and non-permeabilization of the cells was attempted which did not facilitate the detection of Miro1 by the tested Nbs. Though conventional anti-Miro1 antibodies are

commercially available and were utilized for Miro1 staining in this project, the benefits of Nbs over conventional IgGs as proximal affinity labels for super resolution microscopy justifies the rationale for Miro1-specific Nbs applicable for IF detection (Pleiner et al. 2015; Ries et al. 2012; Virant et al. 2018).

In the pursuance of developing functional Nbs as affinity tools applicable for the proteomic characterization and IF detection of Miro1, bivalent formats of the two best performing candidates, M41 and M114 were generated. At this point, it was necessary to consider the implications of the methods previously used for Nb conjugation. With the bivalent Nbs, an advanced labelling strategy using sortase mediated site-specific conjugation combined with click chemistry was therefore used. The application of the modified bivalent Miro1 nanotraps in IP-LC-MS studies indicated that they capture different isoforms of Miro1 and are potential tools for mapping the Miro1 interactome. In previous Miro1 research utilizing IP-LC-MS approaches, tagged Miro1 was immunoprecipitated using the GFP-Trap (Modi et al. 2019) or epitope tag-specific antibodies such as anti-myc (Fatiga et al. 2021) and anti-FLAG antibodies (Kanfer et al. 2015; Castro et al. 2018; Nemani et al. 2018). Since the exogenous expression of Miro1 has been shown to have effects on mitochondrial morphology and transport (Fransson et al. 2006), the normal endogenous conditions may be misrepresented and this introduces bias into proteomic data. Though the specificity of $_{biv}$M41 and $_{biv}$M114 nanotraps for the IP of endogenous Miro1 are clear advantages over existing approaches, the absence of co-immunoprecipitated TRAK1/2, PINK1 and Parkin in their application requires further investigation.

A major highpoint of this thesis was the observation that endogenous Miro1 detection was possible by the application of a fluorophore labelled $_{biv}$M114. In line with previous findings, this confirms the significance of Nb functionalization methods for the generation of efficient binding molecules that enable one-step detection of their antigens (Pleiner et al., 2018; Virant et al., 2018; Götzke et al., 2019). A directly labelled bivalent nanobody can bring the fluorophore closer to the target structure compared to conventional primary and secondary antibody staining (Massa et al. 2016).

The possibility of expressing Nbs in the reducing milieu of living cells makes them applicable intracellular tools for the visualization and modulation of their targets (Rothbauer et al. 2006; Kaiser et al. 2014; Maier et al. 2015; Keller et al. 2018; Wagner and Rothbauer 2020). For the first time, the Nbs M41, M85 and M114 when reformatted as Cbs, enabled the visualization of ectopic Miro1, in living cells. Once more, endogenous Miro1 was not detectable by these Cbs probably due to low levels and a disperse localization of different endogenous isoforms of Miro1. Nonetheless, the Cbs are applicable for the visualization of the dynamics of exogenous

Miro1 as evidenced by their ability to trace normal and Sorafenib-induced mitochondrial shape transitions. Moreover, the Cbs are unaffected by changes in the mitochondrial membrane potential and stably bind their antigen after fixation. This offers a superior advantage compared with established tools for mitochondrial visualization e.g., the MitoTracker series, which bind to thiol groups within mitochondria and can be sensitive to changes in the membrane potential (Chazotte 2011).

Finally, pivoting on the intracellular functionalities of M41 and M114, they were applied as specific substrate recognition components of the SKP1-Cul1-Fbox complex, an artificial ubiquitin-ligase system, to mediate the selective degradation of endogenous and exogenous Miro1. Though relatively low levels of endogenous Miro1 were degraded, the effect of these Fbox-Nb degrons was replicable and non-existent in the absence of the Fbox protein or when the ubiquitin proteasomal system was blocked by MG132 treatment. It is probable that the insufficient binding of M41 and M114 to endogenous Miro1 might be responsible for the minimal depletion of Miro1 observed. Alternatively, Miro1 Nb degrons based on other ubiquitin ligase components such as SPOP (Ju Shin et al. 2015) or TRIM21 (Clift et al. 2018; Chen et al. 2021) might perform better for the depletion of endogenous Miro1.

4.2.2 Functional characteristics of DRP1-Nbs

One of the aims of the project included the use of Nbs as proteomic tools to characterize the molecular interactions of DRP1. Nbs, D7 and D63 were applied in the nanotrap format for the immunoprecipitation of endogenous DRP1. The efficient pull down of endogenous DRP1 isoforms by both nanotraps indicate their potential for use as tools for the proteomic characterization of the DRP1 interactome. Previously, the interactions of DRP1 with MOM-anchored adapters Fis1, Mff and MiD49/51 to mediate mitochondrial fission had been traced using co-immunoprecipitation and cell biological assays (Wells et al. 2007; Loson et al. 2013). More recently, the interplay of DRP1 and BAX in apoptosis was demonstrated using intracellular protein dimerization and single molecule localization microscopy (SMLM) (Jenner et al. 2022). The information provided by these studies on the interactions of DRP1 under the investigated contexts might be further validated using D7 and D63 nanotraps for IP-LC-MS applications.

The subcellular location of DRP1 warrant strategic approaches in the application of DRP1-Nbs as tools for its characterization. Unlike Miro1 whose mitochondrial localization is clearly apparent, in-depth characterization of DRP1 localization may require high resolution microscopy such as SMLM and STORM. Unfortunately, preliminary IF studies of DRP1 were

not successful in this project as D7 and D63 were not functional as affinity detection reagents. Notably, both Nbs were found to bind epitopes in the GED domain of DRP1 which is known to prefer intramolecular interaction with the N-terminal GTPase domain (Zhu et al. 2004). It could be speculated that during fixation, the helical GED domain is locked in its bound state and epitopes are rendered inaccessible to the Nbs for binding. Since different fixation methods were already tested, epitope retrieval may be an alternative approach (Im et al. 2019).

In the line with the aims of this thesis, the possibility of monitoring intracellular DRP1 dynamics was explored. DRP1-Nbs, D7 and D63 formatted as Cbs for intracellular expression. Though expression levels were high, both Cbs did not clearly relocalize to the cytosol or colocalize with ectopically expressed DRP1 (**see Figure 39**). At first, the non-overlap of the Cb and GFP-DRP1 signals were first alluded to the high expression levels of the Cbs and the tendency of unbound Cbs to diffuse through nuclear pores into the nucleus thereby masking any clear colocalization signal. Using a previously described Antigen Mediated Chromobody Stabilization approach (AMCBS) (Keller et al. 2018) which utilized N-terminal ubiquitin fusions increase Cb turnover, so-called turnover-accelerated versions of D7- and D63-Cbs were generated. However, despite lower Cbs levels, intracellular binding could not be verified by microscopy (data not shown). Intracellular interactions between DRP1 Cbs and endogenous DRP1 was then demonstrated by IC-IP followed by western blotting. This observation suggests that the intracellular interactions between DRP1 Cbs and their antigen may be reduced by the intramolecular interactions of the involved DRP1 domains or by interactions with other proteins. This hypothesis is further supported by the clear binding interactions observed after cell lysis with detergents in the IC-IP experiment. Therefore, further tests e.g., fluorescence-two-hybrid (F2H) assay (Zolghadr et al. 2008) are needed to confirm intracellular interactions between DRP1 Cbs and their antigen.

4.3 Relevance of Miro1 and DRP1-Nbs for mitochondrial research.

Currently, the roles played by the different Miro1 domains and how they interact with other proteins to carry out relevant functions are not fully understood. Due to the proven ability of nanobodies to stabilize their antigen, they have been utilized as crystallization chaperones (De Genst et al. 2010; Duhoo et al. 2017; Sigoillot et al. 2019). Though, the crystal structures of individual Miro1 domains, the N-terminal GTPase domain (Smith et al. 2020) and the truncated EF-cGTPase (Klosowiak et al. 2016) have been elucidated, structural information about the intact Miro1 protein is still lacking. The possibility that Miro1-Nbs which bind to epitopes in the N- or C-terminal GTPase domain of Miro1 might be applicable for stabilizing the full-length

protein in structural studies therefore exists. Also, the binding of these Cbs to their specific Miro1 domains in live cells, shows their potential for use in the intracellular characterization of the C-terminal GTPase domain which is not as well studied as its N-terminal counterpart (Kay et al. 2018).

The mitochondrial transport machinery is vital in many neurodegenerative disorders. Tools targeted towards endogenous proteins involved in this process are therefore valuable. Since other Nb-based imaging probes had been applied for the detection of other intracellular proteins using stochastic optical reconstruction microscopy (STORM) (Traenkle and Rothbauer 2017; Virant et al. 2018), the fluorophore conjugated $_{biv}$M114 can be similarly applied in PD studies for advanced imaging of Miro1. Nb-based Ca^{2+} sensors have been applied for monitoring cytosolic and mitochondrial calcium signaling (Prole and Taylor 2019) providing a proof of principle for the application of intracellularly functional Nbs as tools to test the role of Miro1 in Ca^{2+} signalling.

The targeted degradation of Miro1 holds great benefit since it has been shown that molecular failure in Miro1 clearance hampers mitophagy and is implicated in familial and sporadic Parkinson's disease (Hsieh et al. 2016). Currently, CRISPR and RNAi approaches are employed to knock down endogenous Miro1 in loss-of-function studies. However, apart from the inherent limitations of each approach, both methods lead to complete loss of Miro1 thereby disrupting mitochondrial homeostasis (López-Doménech et al. 2016; López-Doménech et al. 2021). For this reason, the Nb-based degrons are alternative tools for targeted Miro1 depletion and they could also be engineered for inducible expression.

Though the DRP1-Nbs selected in this study require more extensive study and optimization, the data obtained from their initial applications indicate that they are effective tools for the proteomic study of DRP1. In addition to the available structural data on DRP1 domains (Fröhlich et al. 2013), the influence of the interactions between DRP1-Nbs and the GED domain on DRP1 self-assembly need to be explored by *in vitro* and intracellular assays. The s-nitrosylation of DRP1 at a residue in the GED domain (Cys644) has been linked to damage in Huntington's disease patient-derived neurons (Haun et al. 2013). Therefore, the selected DRP1-Nbs targeting this domain are potential tools useful for further investigations .

4.4 Conclusions and Outlook

In this dissertation, 7 Miro1-specific and 2 DRP1-specific Nbs have been generated. Biochemical and functional characterization of these novel Nbs revealed high affinity binding in the nanomolar range as well as domain-specific binding within their respective antigens. The Nbs were functionalized as affinity reagents using chemical and site-specific chemo-enzymatic labelling approaches for IP and IF applications. As a further step to optimize binding and functionality, bivalent Miro1-Nbs were developed which showed improved performance compared to their monovalent formats in IP-LC-MS and IF applications. Intracellularly functional Miro1 and DRP1-Nbs were reformatted into Cbs for live cell imaging, however, they were not applicable for the tracing of their endogenous targets. Lastly, the selected degradation of endogenous and exogenous Miro1 was demonstrated using Miro1 Nb-based degrons developed in this study.

Since DRP1 nanotraps were identified as potential tools for the characterization of the DRP1 interactome in this dissertation, they could be further applied for the MS-based investigation of DRP1 interactors in relevant disease models especially during apoptosis.

One major aim that was not achieved in this dissertation was the visualization of endogenous Miro1 and DRP1 using Cbs. In the case of Miro1, the selected monovalent Miro1 Cbs did not clearly colocalize with endogenous Miro1 at mitochondrial structures. Therefore, the application of bivalent Miro1 Cbs might show improved intracellular binding to the endogenous antigen. For the visualization of endogenous DRP1 using Cbs, it might be advantageous to design a new biopanning campaign to screen the DRP1 Nb-phage library for Nbs which can clearly localize to DRP1 within the cellular environment. Such studies have been documented (Matz et al. 2014; Bery et al. 2019).

Further applications of the fluorescently labelled $_{biv}$M114 as an affinity detection reagent for the super resolution imaging of Miro1 in relevant neurodegenerative disease models are also indicated. Additionally, it could also serve as a useful probe in the study of Miro1 functions in the intercellular mitochondrial transport occurring in stressed and damaged tissues (Liu et al. 2021).

5 REFERENCES

1. Ahmad T, Mukherjee S, Pattnaik B, Kumar M, Singh S, Kumar M, Rehman R, Tiwari BK, Jha KA, Barhanpurkar AP, Wani MR, Roy SS, Mabalirajan U, Ghosh B, Agrawal A (2014) Miro1 regulates intercellular mitochondrial transport & enhances mesenchymal stem cell rescue efficacy. The EMBO Journal 33 (9):994-1010. doi:10.1002/EMBJ.201386030
2. Alexander C, Votruba M, Pesch UE, Thiselton DL, Mayer S, Moore A, Rodriguez M, Kellner U, Leo-Kottler B, Auburger G, Bhattacharya SS, Wissinger B (2000) OPA1, encoding a dynamin-related GTPase, is mutated in autosomal dominant optic atrophy linked to chromosome 3q28. Nat Genet 26 (2):211-215. doi:10.1038/79944
3. Arbabi Ghahroudi M, Desmyter A, Wyns L, Hamers R, Muyldermans S (1997) Selection and identification of single domain antibody fragments from camel heavy-chain antibodies. FEBS Letters 414 (3):521-526. doi:https://doi.org/10.1016/S0014-5793(97)01062-4
4. Asaadi Y, Jouneghani FF, Janani S, Rahbarizadeh F (2021) A comprehensive comparison between camelid nanobodies and single chain variable fragments. Biomark Res 9 (1):87. doi:10.1186/s40364-021-00332-6
5. Babenko V, Silachev D, Popkov V, Zorova L, Pevzner I, Plotnikov E, Sukhikh G, Zorov D, Babenko VA, Silachev DN, Popkov VA, Zorova LD, Pevzner IB, Plotnikov EY, Sukhikh GT, Zorov DB (2018) Miro1 Enhances Mitochondria Transfer from Multipotent Mesenchymal Stem Cells (MMSC) to Neural Cells and Improves the Efficacy of Cell Recovery. Molecules 23 (3):687-687. doi:10.3390/molecules23030687
6. Bai C, Sen P, Hofmann K, Ma L, Goebl M, Harper JW, Elledge SJ (1996) SKP1 Connects Cell Cycle Regulators to the Ubiquitin Proteolysis Machinery through a Novel Motif, the F-Box. Cell 86 (2):263-274. doi:10.1016/S0092-8674(00)80098-7
7. Baker BM, Haynes CM (2011) Mitochondrial protein quality control during biogenesis and aging. Trends in biochemical sciences 36 (5):254-261. doi:10.1016/j.tibs.2011.01.004
8. Baudisch B, Pfort I, Sorge E, Conrad U (2018) Nanobody-Directed Specific Degradation of Proteins by the 26S-Proteasome in Plants. doi:10.3389/fpls.2018.00130
9. Beerli RR, Wels W, Hynes NE (1994a) Autocrine inhibition of the epidermal growth factor receptor by intracellular expression of a single-chain antibody. Biochem Biophys Res Commun 204 (2):666-672. doi:10.1006/bbrc.1994.2511
10. Beerli RR, Wels W, Hynes NE (1994b) Intracellular expression of single chain antibodies reverts ErbB-2 transformation. J Biol Chem 269 (39):23931-23936

11. Beghein E, Gettemans J (2017) Nanobody Technology: A Versatile Toolkit for Microscopic Imaging, Protein-Protein Interaction Analysis, and Protein Function Exploration. Front Immunol 8:771. doi:10.3389/fimmu.2017.00771
12. Benda C (1898) Ueber die spermatogenese der vertebraten und höherer evertebraten, II. Theil: Die histiogenese der spermien. Arch Anat Physiol 73:393-398
13. Berland L, Kim L, Abousaway O, Mines A, Mishra S, Clark L, Hofman P, Rashidian M (2021) Nanobodies for Medical Imaging: About Ready for Prime Time? Biomolecules 11 (5). doi:10.3390/biom11050637
14. Berman HM, Westbrook J, Feng Z, Gilliland G, Bhat TN, Weissig H, Shindyalov IN, Bourne PE (2000) The Protein Data Bank. Nucleic Acids Res 28 (1):235-242. doi:10.1093/nar/28.1.235
15. Bery N, Keller L, Soulié M, Gence R, Iscache AL, Cherier J, Cabantous S, Sordet O, Lajoie-Mazenc I, Pedelacq JD, Favre G, Olichon A (2019) A Targeted Protein Degradation Cell-Based Screening for Nanobodies Selective toward the Cellular RHOB GTP-Bound Conformation. Cell Chemical Biology 26 (11):1544-1558.e1546. doi:10.1016/J.CHEMBIOL.2019.08.009
16. Biocca S, Neuberger MS, Cattaneo A (1990) Expression and targeting of intracellular antibodies in mammalian cells. The EMBO journal 9 (1):101-108
17. Birsa N, Norkett R, Wauer T, Mevissen TE, Wu HC, Foltynie T, Bhatia K, Hirst WD, Komander D, Plun-Favreau H, Kittler JT (2014) Lysine 27 ubiquitination of the mitochondrial transport protein Miro is dependent on serine 65 of the Parkin ubiquitin ligase. J Biol Chem 289 (21):14569-14582. doi:10.1074/jbc.M114.563031
18. Bogan N, Cabot JB (1991) Light and electron microscopic analyses of intraspinal axon collaterals of sympathetic preganglionic neurons. Brain Res 541 (2):241-251. doi:10.1016/0006-8993(91)91024-u
19. Bossy B, Petrilli A, Klinglmayr E, Chen J, Lutz-Meindl U, Knott AB, Masliah E, Schwarzenbacher R, Bossy-Wetzel E (2010) S-Nitrosylation of DRP1 does not affect enzymatic activity and is not specific to Alzheimer's disease. J Alzheimers Dis 20 Suppl 2:S513-526. doi:10.3233/JAD-2010-100552
20. Boureux A, Vignal E, Faure S, Fort P (2007) Evolution of the Rho family of ras-like GTPases in eukaryotes. Molecular biology and evolution 24 (1):203-216. doi:10.1093/molbev/msl145
21. Braun MB, Traenkle B, Koch PA, Emele F, Weiss F, Poetz O, Stehle T, Rothbauer U (2016) Peptides in headlock--a novel high-affinity and versatile peptide-binding nanobody for proteomics and microscopy. Sci Rep 6:19211. doi:10.1038/srep19211

22. Buchfellner A, Yurlova L, Nuske S, Scholz AM, Bogner J, Ruf B, Zolghadr K, Drexler SE, Drexler GA, Girst S, Greubel C, Reindl J, Siebenwirth C, Romer T, Friedl AA, Rothbauer U (2016) A New Nanobody-Based Biosensor to Study Endogenous PARP1 In Vitro and in Live Human Cells. PLoS One 11 (3):e0151041. doi:10.1371/journal.pone.0151041
23. Burgess A, Lorca T, Castro A (2012) Quantitative live imaging of endogenous DNA replication in mammalian cells. PLoS One 7 (9):e45726. doi:10.1371/journal.pone.0045726
24. Butler JE, Ni L, Nessler R, Joshi KS, Suter M, Rosenberg B, Chang J, Brown WR, Cantarero LA (1992) The physical and functional behavior of capture antibodies adsorbed on polystyrene. J Immunol Methods 150 (1-2):77-90. doi:10.1016/0022-1759(92)90066-3
25. Castro IG, Richards DM, Metz J, Costello JL, Passmore JB, Schrader TA, Gouveia A, Ribeiro D, Schrader M (2018) A role for Mitochondrial Rho GTPase 1 (MIRO1) in motility and membrane dynamics of peroxisomes. Traffic (Copenhagen, Denmark) 19 (3):229-229. doi:10.1111/TRA.12549
26. Caussinus E, Kanca O, Affolter M (2011) Fluorescent fusion protein knockout mediated by anti-GFP nanobody. Nat Struct Mol Biol 19 (1):117-121. doi:10.1038/nsmb.2180
27. Chakravarty R, Goel S, Cai W (2014) Nanobody: the "magic bullet" for molecular imaging? Theranostics 4 (4):386-398. doi:10.7150/thno.8006
28. Chang KT, Niescier RF, Min KT (2011) Mitochondrial matrix Ca2+ as an intrinsic signal regulating mitochondrial motility in axons. Proc Natl Acad Sci U S A 108 (37):15456-15461. doi:10.1073/pnas.1106862108
29. Chazotte B (2011) Labeling Mitochondria with MitoTracker Dyes. Cold Spring Harbor Protocols 2011 (8):pdb.prot5648-pdb.prot5648. doi:10.1101/PDB.PROT5648
30. Cheloha RW, Harmand TJ, Wijne C, Schwartz TU, Ploegh HL (2020) Exploring cellular biochemistry with nanobodies. Journal of Biological Chemistry 295 (45):15307-15327. doi:10.1074/JBC.REV120.012960
31. Chen G, Kong Y, Li Y, Huang A, Wang C, Zhou S, Yang Z, Wu Y, Ren J, Ying T (2021) A Promising Intracellular Protein-Degradation Strategy: TRIMbody-Away Technique Based on Nanobody Fragment. Biomolecules 11 (10). doi:10.3390/biom11101512
32. Chen I, Dorr BM, Liu DR (2011) A general strategy for the evolution of bond-forming enzymes using yeast display. Proc Natl Acad Sci U S A 108 (28):11399-11404. doi:10.1073/pnas.1101046108

33. Cho DH, Nakamura T, Fang J, Cieplak P, Godzik A, Gu Z, Lipton SA (2009) S-nitrosylation of Drp1 mediates beta-amyloid-related mitochondrial fission and neuronal injury. Science 324 (5923):102-105. doi:10.1126/science.1171091
34. Cho HJ, Sung DH, Kim BJ, Ki CS (2007) Mitochondrial GTPase mitofusin 2 mutations in Korean patients with Charcot-Marie-Tooth neuropathy type 2. Clin Genet 71 (3):267-272. doi:10.1111/j.1399-0004.2007.00763.x
35. Cioni JM, Lin JQ, Holtermann AV, Koppers M, Jakobs MAH, Azizi A, Turner-Bridger B, Shigeoka T, Franze K, Harris WA, Holt CE (2019) Late Endosomes Act as mRNA Translation Platforms and Sustain Mitochondria in Axons. Cell 176 (1-2):56-72 e15. doi:10.1016/j.cell.2018.11.030
36. Clift D, So C, McEwan WA, James LC, Schuh M (2018) Acute and rapid degradation of endogenous proteins by Trim-Away. Nat Protoc 13 (10):2149-2175. doi:10.1038/s41596-018-0028-3
37. Colazet M, Chames P (2018) Phage Display and Selections on Purified Antigens. Methods Mol Biol 1827:165-178. doi:10.1007/978-1-4939-8648-4_9
38. Collins Y, Chouchani ET, James AM, Menger KE, Cochemé HM, Murphy MP (2012) Mitochondrial redox signalling at a glance. Journal of Cell Science 125 (4):801-806. doi:10.1242/jcs.098475
39. Conrad U, Scheller J (2005) Considerations on antibody-phage display methodology. Comb Chem High Throughput Screen 8 (2):117-126. doi:10.2174/1386207053258532
40. Conrath KE, Wernery U, Muyldermans S, Nguyen VK (2003) Emergence and evolution of functional heavy-chain antibodies in Camelidae. Dev Comp Immunol 27 (2):87-103. doi:10.1016/s0145-305x(02)00071-x
41. Coomber DWJ (2002) Panning of Antibody Phage-Display Libraries. In: O'Brien PM, Aitken R (eds) Antibody Phage Display: Methods and Protocols. Humana Press, Totowa, NJ, pp 133-145. doi:10.1385/1-59259-240-6:133
42. Cribbs JT, Strack S (2007) Reversible phosphorylation of Drp1 by cyclic AMP-dependent protein kinase and calcineurin regulates mitochondrial fission and cell death. EMBO Rep 8 (10):939-944. doi:10.1038/sj.embor.7401062
43. De Genst E, Silence K, Decanniere K, Conrath K, Loris R, Kinne J, Muyldermans S, Wyns L (2006) Molecular basis for the preferential cleft recognition by dromedary heavy-chain antibodies. Proc Natl Acad Sci U S A 103 (12):4586-4591. doi:10.1073/pnas.0505379103
44. De Genst EJ, Guilliams T, Wellens J, O'Day EM, Waudby CA, Meehan S, Dumoulin M, Hsu ST, Cremades N, Verschueren KH, Pardon E, Wyns L, Steyaert J, Christodoulou J, Dobson CM (2010) Structure and properties of a complex of alpha-synuclein and a

single-domain camelid antibody. J Mol Biol 402 (2):326-343. doi:10.1016/j.jmb.2010.07.001

45. De Meyer T, Muyldermans S, Depicker A (2014) Nanobody-based products as research and diagnostic tools. Trends Biotechnol 32 (5):263-270. doi:10.1016/j.tibtech.2014.03.001
46. De Vos J, Mathijs I, Xavier C, Massa S, Wernery U, Bouwens L, Lahoutte T, Muyldermans S, Devoogdt N (2014) Specific targeting of atherosclerotic plaques in ApoE(-/-) mice using a new Camelid sdAb binding the vulnerable plaque marker LOX-1. Mol Imaging Biol 16 (5):690-698. doi:10.1007/s11307-014-0731-6
47. Deschaght P, Vintém AP, Logghe M, Conde M, Felix D, Mensink R, Gonçalves J, Audiens J, Bruynooghe Y, Figueiredo R, Ramos D, Tanghe R, Teixeira D, Van de Ven L, Stortelers C, Dombrecht B (2017) Large Diversity of Functional Nanobodies from a Camelid Immune Library Revealed by an Alternative Analysis of Next-Generation Sequencing Data. Frontiers in Immunology 8
48. Desmyter A, Transue TR, Ghahroudi MA, Thi MH, Poortmans F, Hamers R, Muyldermans S, Wyns L (1996) Crystal structure of a camel single-domain VH antibody fragment in complex with lysozyme. Nat Struct Biol 3 (9):803-811. doi:10.1038/nsb0996-803
49. Duhoo Y, Roche J, Trinh TTN, Desmyter A, Gaubert A, Kellenberger C, Cambillau C, Roussel A, Leone P (2017) Camelid nanobodies used as crystallization chaperones for different constructs of PorM, a component of the type IX secretion system from Porphyromonas gingivalis. Acta Crystallogr F Struct Biol Commun 73 (Pt 5):286-293. doi:10.1107/S2053230X17005969
50. Ernster L, Schatz G (1981) Mitochondria: a historical review. J Cell Biol 91 (3 Pt 2):227s-255s. doi:10.1083/jcb.91.3.227s
51. Fagbadebo FO, Kaiser PD, Zittlau K, Bartlick N, Wagner TR, Froehlich T, Jarjour G, Nueske S, Scholz A, Traenkle B, Macek B, Rothbauer U (2022) A Nanobody-Based Toolset to Monitor and Modify the Mitochondrial GTPase Miro1. Frontiers in Molecular Biosciences 9
52. Fannjiang Y, Cheng WC, Lee SJ, Qi B, Pevsner J, McCaffery JM, Hill RB, Basanez G, Hardwick JM (2004) Mitochondrial fission proteins regulate programmed cell death in yeast. Genes Dev 18 (22):2785-2797. doi:10.1101/gad.1247904
53. Fatiga FF, Wang LJ, Hsu T, Capuno JI, Fu CY (2021) Miro1 functions as an inhibitory regulator of MFN at elevated mitochondrial Ca(2+) levels. Journal of cellular biochemistry. doi:10.1002/jcb.30138

54. Flannery PJ, Trushina E (2019) Mitochondrial dynamics and transport in Alzheimer's disease. Molecular and Cellular Neuroscience 98:109-120. doi:https://doi.org/10.1016/j.mcn.2019.06.009
55. Flego M, Frau A, Accardi L, Mallano A, Ascione A, Gellini M, Fanunza E, Vella S, Di Bonito P, Tramontano E (2019) Intracellular human antibody fragments recognizing the VP35 protein of Zaire Ebola filovirus inhibit the protein activity. BMC Biotechnol 19 (1):64. doi:10.1186/s12896-019-0554-2
56. Fransson Å, Ruusala A, Aspenström P (2003) Atypical Rho GTPases Have Roles in Mitochondrial Homeostasis and Apoptosis *. Journal of Biological Chemistry 278 (8):6495-6502. doi:10.1074/jbc.M208609200
57. Fransson Å, Ruusala A, Aspenström P (2006) The atypical Rho GTPases Miro-1 and Miro-2 have essential roles in mitochondrial trafficking. Biochemical and Biophysical Research Communications 344 (2):500-510. doi:10.1016/J.BBRC.2006.03.163
58. Frenzel A, Hust M, Schirrmann T (2013) Expression of recombinant antibodies. Front Immunol 4:217. doi:10.3389/fimmu.2013.00217
59. Fröhlich C, Grabiger S, Schwefel D, Faelber K, Rosenbaum E, Mears J, Rocks O, Daumke O (2013) Structural insights into oligomerization and mitochondrial remodelling of dynamin 1-like protein. The EMBO Journal 32 (9):1280-1292. doi:https://doi.org/10.1038/emboj.2013.74
60. Galli V, Sebastian R, Moutel S, Ecard J, Perez F, Roux A (2017) Uncoupling of dynamin polymerization and GTPase activity revealed by the conformation-specific nanobody dynab. eLife 6. doi:10.7554/eLife.25197
61. Gandre-Babbe S, van der Bliek AM (2008) The novel tail-anchored membrane protein Mff controls mitochondrial and peroxisomal fission in mammalian cells. Mol Biol Cell 19 (6):2402-2412. doi:10.1091/mbc.E07-12-1287
62. Gebauer M, Skerra A (2015) Alternative Protein Scaffolds as Novel Biotherapeutics. In: Rosenberg A, Demeule B (eds) Biobetters: Protein Engineering to Approach the Curative. Springer New York, New York, NY, pp 221-268. doi:10.1007/978-1-4939-2543-8_13
63. Gettemans J, De Dobbelaer B (2021) Transforming nanobodies into high-precision tools for protein function analysis. Am J Physiol Cell Physiol 320 (2):C195-C215. doi:10.1152/ajpcell.00435.2020
64. Gibson DG, Young L, Chuang R-Y, Venter JC, Hutchison CA, Smith HO (2009) Enzymatic assembly of DNA molecules up to several hundred kilobases. Nature Methods 6 (5):343-345. doi:10.1038/nmeth.1318

65. Glancy B (2020) Visualizing Mitochondrial Form and Function within the Cell. Trends Mol Med 26 (1):58-70. doi:10.1016/j.molmed.2019.09.009
66. Glancy B, Kim Y, Katti P, Willingham TB (2020) The Functional Impact of Mitochondrial Structure Across Subcellular Scales. Frontiers in Physiology 11
67. Gomes LC, Di Benedetto G, Scorrano L (2011) During autophagy mitochondria elongate, are spared from degradation and sustain cell viability. Nat Cell Biol 13 (5):589-598. doi:10.1038/ncb2220
68. Götzke H, Kilisch M, Martínez-Carranza MA-O, Sograte-Idrissi SA-O, Rajavel AA-O, Schlichthaerle T, Engels NA-O, Jungmann RA-O, Stenmark PA-O, Opazo FA-O, Frey SA-O (2019) The ALFA-tag is a highly versatile tool for nanobody-based bioscience applications. Nat Commun (2041-1723 (Electronic))
69. Grossmann D, Krüger R, Berenguer-Escuder C, Chemla A, Arena G (2020) The Emerging Role of RHOT1/Miro1 in the Pathogenesis of Parkinson's Disease. Frontiers in Neurology | wwwfrontiersinorg 11:587-587. doi:10.3389/fneur.2020.00587
70. Guo C, Wilkinson KA, Evans AJ, Rubin PP, Henley JM (2017) SENP3-mediated deSUMOylation of Drp1 facilitates interaction with Mff to promote cell death. Sci Rep 7:43811. doi:10.1038/srep43811
71. Hamers-Casterman C, Atarhouch T, Muyldermans S, Robinson G, Hamers C, Songa EB, Bendahman N, Hamers R (1993) Naturally occurring antibodies devoid of light chains. Nature 363 (6428):446-448. doi:10.1038/363446a0
72. Han H, Tan J, Wang R, Wan H, He Y, Yan X, Guo J, Gao Q, Li J, Shang S, Chen F, Tian R, Liu W, Liao L, Tang B, Zhang Z (2020) PINK1 phosphorylates Drp1(S616) to regulate mitophagy-independent mitochondrial dynamics. EMBO Rep 21 (8):e48686. doi:10.15252/embr.201948686
73. Hardiman O, Al-Chalabi A, Chio A, Corr EM, Logroscino G, Robberecht W, Shaw PJ, Simmons Z, van den Berg LH (2017) Amyotrophic lateral sclerosis. Nat Rev Dis Primers 3:17085. doi:10.1038/nrdp.2017.85
74. Harmand TJ, Islam A, Pishesha N, Ploegh HL (2021) Nanobodies as in vivo, non-invasive, imaging agents. RSC Chem Biol 2 (3):685-701. doi:10.1039/d1cb00023c
75. Harmsen MM, Ruuls RC, Nijman IJ, Niewold TA, Frenken LG, de Geus B (2000) Llama heavy-chain V regions consist of at least four distinct subfamilies revealing novel sequence features. Mol Immunol 37 (10):579-590. doi:10.1016/s0161-5890(00)00081-x
76. Hassanzadeh-Ghassabeh G, Devoogdt N, De Pauw P, Vincke C, Muyldermans S (2013) Nanobodies and their potential applications. Nanomedicine 8 (6):1013-1026. doi:10.2217/nnm.13.86

77. Hatch AL, Ji WK, Merrill RA, Strack S, Higgs HN (2016) Actin filaments as dynamic reservoirs for Drp1 recruitment. Mol Biol Cell 27 (20):3109-3121. doi:10.1091/mbc.E16-03-0193
78. Haun F, Nakamura T, Shiu AD, Cho DH, Tsunemi T, Holland EA, La Spada AR, Lipton SA (2013) S-nitrosylation of dynamin-related protein 1 mediates mutant huntingtin-induced mitochondrial fragmentation and neuronal injury in Huntington's disease. Antioxid Redox Signal 19 (11):1173-1184. doi:10.1089/ars.2012.4928
79. Henry KA, Hussack G, Collins C, Zwaagstra JC, Tanha J, MacKenzie CR (2016) Isolation of TGF-β-neutralizing single-domain antibodies of predetermined epitope specificity using next-generation DNA sequencing. Protein Engineering, Design and Selection 29 (10):439-443. doi:10.1093/protein/gzw043
80. Hsieh C-H, Shaltouki A, Gonzalez AE, Cruz ABd, Burbulla LF, Lawrence ES, Schüle B, Krainc D, Palmer TD, Wang X (2016) Functional Impairment in Miro Degradation and Mitophagy Is a Shared Feature in Familial and Sporadic Parkinson's Disease. Cell Stem Cell 19 (6):709-724. doi:10.1016/J.STEM.2016.08.002
81. Hsieh CH, Li L, Vanhauwaert R, Nguyen KT, Davis MD, Bu G, Wszolek ZK, Wang X (2019) Miro1 Marks Parkinson's Disease Subset and Miro1 Reducer Rescues Neuron Loss in Parkinson's Models. Cell metabolism 30 (6):1131-1140.e1137. doi:10.1016/j.cmet.2019.08.023
82. Ihenacho UK, Meacham KA, Harwig MC, Widlansky ME, Hill RB (2021) Mitochondrial Fission Protein 1: Emerging Roles in Organellar Form and Function in Health and Disease. Front Endocrinol (Lausanne) 12:660095. doi:10.3389/fendo.2021.660095
83. Im K, Mareninov S, Diaz MFP, Yong WH (2019) An Introduction to Performing Immunofluorescence Staining. In: Yong WH (ed) Biobanking: Methods and Protocols. Springer New York, New York, NY, pp 299-311. doi:10.1007/978-1-4939-8935-5_26
84. Jagasia R, Grote P, Westermann B, Conradt B (2005) DRP-1-mediated mitochondrial fragmentation during EGL-1-induced cell death in C. elegans. Nature 433 (7027):754-760. doi:10.1038/nature03316
85. Jenner A, Peña-Blanco A, Salvador-Gallego R, Ugarte-Uribe B, Zollo C, Ganief T, Bierlmeier J, Mund M, Lee JE, Ries J, Schwarzer D, Macek B, Garcia-Saez AJ (2022) DRP1 interacts directly with BAX to induce its activation and apoptosis. The EMBO Journal n/a (n/a):e108587. doi:https://doi.org/10.15252/embj.2021108587
86. Jewett JC, Bertozzi CR (2010) Cu-free click cycloaddition reactions in chemical biology. Chemical Society Reviews 39 (4):1272-1279. doi:10.1039/B901970G

87. Ji WK, Chakrabarti R, Fan X, Schoenfeld L, Strack S, Higgs HN (2017) Receptor-mediated Drp1 oligomerization on endoplasmic reticulum. J Cell Biol 216 (12):4123-4139. doi:10.1083/jcb.201610057
88. Jin SM, Lazarou M, Wang C, Kane LA, Narendra DP, Youle RJ (2010) Mitochondrial membrane potential regulates PINK1 import and proteolytic destabilization by PARL. J Cell Biol 191 (5):933-942. doi:10.1083/jcb.201008084
89. Jornayvaz FR, Shulman GI (2010) Regulation of mitochondrial biogenesis. Essays Biochem 47:69-84. doi:10.1042/bse0470069
90. Joshi AU, Saw NL, Vogel H, Cunnigham AD, Shamloo M, Mochly-Rosen D (2018) Inhibition of Drp1/Fis1 interaction slows progression of amyotrophic lateral sclerosis. EMBO Mol Med 10 (3). doi:10.15252/emmm.201708166
91. Ju Shin Y, Kyun Park S, Jung Jung Y, Na Kim Y, Sung Kim K, Kyu Park O, Kwon S-H, Ho Jeon S, Trinh LA, Fraser SE, Kee Y, Joon Hwang B (2015) Nanobody-targeted E3-ubiquitin ligase complex degrades nuclear proteins. Scientific Reports 5 (1):14269. doi:10.1038/srep14269
92. Kabat EA, Wu TT (1991) Identical V region amino acid sequences and segments of sequences in antibodies of different specificities. Relative contributions of VH and VL genes, minigenes, and complementarity-determining regions to binding of antibody-combining sites. The Journal of Immunology 147 (5):1709
93. Kaiser PD, Maier J, Traenkle B, Emele F, Rothbauer U (2014) Recent progress in generating intracellular functional antibody fragments to target and trace cellular components in living cells. Biochim Biophys Acta 1844 (11):1933-1942. doi:10.1016/j.bbapap.2014.04.019
94. Kalia R, Wang RY, Yusuf A, Thomas PV, Agard DA, Shaw JM, Frost A (2018) Structural basis of mitochondrial receptor binding and constriction by DRP1. Nature 558 (7710):401-405. doi:10.1038/s41586-018-0211-2
95. Kamerkar SC, Kraus F, Sharpe AJ, Pucadyil TJ, Ryan MT (2018) Dynamin-related protein 1 has membrane constricting and severing abilities sufficient for mitochondrial and peroxisomal fission. Nature Communications 9 (1):5239. doi:10.1038/s41467-018-07543-w
96. Kanfer G, Courthéoux T, Peterka M, Meier S, Soste M, Melnik A, Reis K, Aspenström P, Peter M, Picotti P, Benoıˆt, Kornmann Bt (2015) Mitotic redistribution of the mitochondrial network by Miro and Cenp-F. doi:10.1038/ncomms9015
97. Kang TH, Seong BL (2020) Solubility, Stability, and Avidity of Recombinant Antibody Fragments Expressed in Microorganisms. Front Microbiol 11:1927. doi:10.3389/fmicb.2020.01927

98. Karbowski M, Lee YJ, Gaume B, Jeong SY, Frank S, Nechushtan A, Santel A, Fuller M, Smith CL, Youle RJ (2002) Spatial and temporal association of Bax with mitochondrial fission sites, Drp1, and Mfn2 during apoptosis. J Cell Biol 159 (6):931-938. doi:10.1083/jcb.200209124
99. Karbowski M, Youle RJ (2011) Regulating mitochondrial outer membrane proteins by ubiquitination and proteasomal degradation. Curr Opin Cell Biol 23 (4):476-482. doi:10.1016/j.ceb.2011.05.007
100. Kashatus JA, Nascimento A, Myers LJ, Sher A, Byrne FL, Hoehn KL, Counter CM, Kashatus DF (2015) Erk2 phosphorylation of Drp1 promotes mitochondrial fission and MAPK-driven tumor growth. Mol Cell 57 (3):537-551. doi:10.1016/j.molcel.2015.01.002
101. Kay L, Pienaar IS, Cooray R, Black G, Soundararajan M (2018) Understanding Miro GTPases: Implications in the Treatment of Neurodegenerative Disorders. Molecular Neurobiology 55 (9):7352-7365. doi:10.1007/s12035-018-0927-x
102. Kazlauskaite A, Kelly V, Johnson C, Baillie C, Hastie CJ, Peggie M, Macartney T, Woodroof HI, Alessi DR, Pedrioli PG, Muqit MM (2014) Phosphorylation of Parkin at Serine65 is essential for activation: elaboration of a Miro1 substrate-based assay of Parkin E3 ligase activity. Open Biol 4:130213. doi:10.1098/rsob.130213
103. Kazlauskaite A, Muqit MM (2015) PINK1 and Parkin - mitochondrial interplay between phosphorylation and ubiquitylation in Parkinson's disease. FEBS J 282 (2):215-223. doi:10.1111/febs.13127
104. Keller BM, Maier J, Secker KA, Egetemaier SM, Parfyonova Y, Rothbauer U, Traenkle B (2018) Chromobodies to Quantify Changes of Endogenous Protein Concentration in Living Cells. Mol Cell Proteomics 17 (12):2518-2533. doi:10.1074/mcp.TIR118.000914
105. Keller L, Bery N, Tardy C, Ligat L, Favre G, Rabbitts TH, Olichon A (2019) Selection and Characterization of a Nanobody Biosensor of GTP-Bound RHO Activities. Antibodies (Basel) 8 (1). doi:10.3390/antib8010008
106. Klooster R, Maassen BT, Stam JC, Hermans PW, Ten Haaft MR, Detmers FJ, de Haard HJ, Post JA, Theo Verrips C (2007) Improved anti-IgG and HSA affinity ligands: clinical application of VHH antibody technology. J Immunol Methods 324 (1-2):1-12. doi:10.1016/j.jim.2007.04.005
107. Klosowiak JL, Focia PJ, Chakravarthy S, Landahl EC, Freymann DM, Rice SE (2013) Structural coupling of the EF hand and C-terminal GTPase domains in the mitochondrial protein Miro. EMBO reports 14 (11):968-974. doi:https://doi.org/10.1038/embor.2013.151

108. Klosowiak JL, Park S, Smith KP, French ME, Focia PJ, Freymann DM, Rice SE (2016) Structural insights into Parkin substrate lysine targeting from minimal Miro substrates. Scientific Reports 6. doi:10.1038/srep33019
109. Koide A, Koide S (2007) Monobodies: antibody mimics based on the scaffold of the fibronectin type III domain. Methods Mol Biol 352:95-109. doi:10.1385/1-59745-187-8:95
110. Krasniqi A, D'Huyvetter M, Xavier C, Van der Jeught K, Muyldermans S, Van Der Heyden J, Lahoutte T, Tavernier J, Devoogdt N (2017) Theranostic Radiolabeled Anti-CD20 sdAb for Targeted Radionuclide Therapy of Non-Hodgkin Lymphoma. Mol Cancer Ther 16 (12):2828-2839. doi:10.1158/1535-7163.MCT-17-0554
111. Kraus F, Roy K, Pucadyil TJ, Ryan MT (2021) Function and regulation of the divisome for mitochondrial fission. Nature 590 (7844):57-66. doi:10.1038/s41586-021-03214-x
112. Kuo C-L, Oyler GA, Shoemaker CB (2011) Accelerated Neuronal Cell Recovery from Botulinum Neurotoxin Intoxication by Targeted Ubiquitination. doi:10.1371/journal.pone.0020352
113. Lazarou M, Sliter DA, Kane LA, Sarraf SA, Wang C, Burman JL, Sideris DP, Fogel AI, Youle RJ (2015) The ubiquitin kinase PINK1 recruits autophagy receptors to induce mitophagy. Nature 524 (7565):309-314. doi:10.1038/nature14893
114. Lee YJ, Jeong SY, Karbowski M, Smith CL, Youle RJ (2004) Roles of the mammalian mitochondrial fission and fusion mediators Fis1, Drp1, and Opa1 in apoptosis. Mol Biol Cell 15 (11):5001-5011. doi:10.1091/mbc.e04-04-0294
115. Levi S, Rovida E (2009) The role of iron in mitochondrial function. Biochimica et Biophysica Acta (BBA) - General Subjects 1790 (7):629-636. doi:https://doi.org/10.1016/j.bbagen.2008.09.008
116. Li T, Huang M, Xiao H, Zhang G, Ding J, Wu P, Zhang H, Sheng J, Chen C (2017) Selection and characterization of specific nanobody against bovine virus diarrhea virus (BVDV) E2 protein. PLoS One 12 (6):e0178469. doi:10.1371/journal.pone.0178469
117. Lim CC, Woo PCY, Lim TS (2019) Development of a Phage Display Panning Strategy Utilizing Crude Antigens: Isolation of MERS-CoV Nucleoprotein human antibodies. Scientific Reports 9 (1):6088. doi:10.1038/s41598-019-42628-6
118. Liu D, Gao Y, Liu J, Huang Y, Yin J, Feng Y, Shi L, Meloni BP, Zhang C, Zheng M, Gao J (2021) Intercellular mitochondrial transfer as a means of tissue revitalization. Signal Transduction and Targeted Therapy 6 (1):65. doi:10.1038/s41392-020-00440-z
119. Liu S, Sawada T, Lee S, Yu W, Silverio G, Alapatt P, Millan I, Shen A, Saxton W, Kanao T, Takahashi R, Hattori N, Imai Y, Lu B (2012) Parkinson's disease-associated kinase

PINK1 regulates Miro protein level and axonal transport of mitochondria. PLoS Genet 8 (3):e1002537. doi:10.1371/journal.pgen.1002537

120. Liu W, Song H, Chen Q, Yu J, Xian M, Nian R, Feng D (2018) Recent advances in the selection and identification of antigen-specific nanobodies. Mol Immunol 96:37-47. doi:10.1016/j.molimm.2018.02.012

121. Lofblom J, Frejd FY, Stahl S (2011) Non-immunoglobulin based protein scaffolds. Curr Opin Biotechnol 22 (6):843-848. doi:10.1016/j.copbio.2011.06.002

122. López-Doménech G, Higgs Nathalie F, Vaccaro V, Roš H, Arancibia-Cárcamo IL, MacAskill Andrew F, Kittler Josef T (2016) Loss of Dendritic Complexity Precedes Neurodegeneration in a Mouse Model with Disrupted Mitochondrial Distribution in Mature Dendrites. Cell Reports 17 (2):317-327. doi:10.1016/j.celrep.2016.09.004

123. López-Doménech G, Howden JH, Covill-Cooke C, Morfill C, Patel JV, Bürli R, Crowther D, Birsa N, Brandon NJ, Kittler JT (2021) Loss of neuronal Miro1 disrupts mitophagy and induces hyperactivation of the integrated stress response. The EMBO journal 40 (14):e100715. doi:10.15252/embj.2018100715

124. Loson OC, Song Z, Chen H, Chan DC (2013) Fis1, Mff, MiD49, and MiD51 mediate Drp1 recruitment in mitochondrial fission. Mol Biol Cell 24 (5):659-667. doi:10.1091/mbc.E12-10-0721

125. Luo F, Herrup K, Qi X, Yang Y (2017) Inhibition of Drp1 hyper-activation is protective in animal models of experimental multiple sclerosis. Exp Neurol 292:21-34. doi:10.1016/j.expneurol.2017.02.015

126. Ma K, Chen G, Li W, Kepp O, Zhu Y, Chen Q (2020) Mitophagy, Mitochondrial Homeostasis, and Cell Fate. Frontiers in Cell and Developmental Biology 8

127. MacAskill AF, Brickley K, Stephenson FA, Kittler JT (2009a) GTPase dependent recruitment of Grif-1 by Miro1 regulates mitochondrial trafficking in hippocampal neurons. Molecular and Cellular Neuroscience 40 (3):301-312. doi:https://doi.org/10.1016/j.mcn.2008.10.016

128. MacAskill AF, Rinholm JE, Twelvetrees AE, Arancibia-Carcamo IL, Muir J, Fransson A, Aspenstrom P, Attwell D, Kittler JT (2009b) Miro1 Is a Calcium Sensor for Glutamate Receptor-Dependent Localization of Mitochondria at Synapses. Neuron 61 (4):541-555. doi:10.1016/j.neuron.2009.01.030

129. Magrané J, Cortez C, Gan WB, Manfredi G (2014) Abnormal mitochondrial transport and morphology are common pathological denominators in SOD1 and TDP43 ALS mouse models. Hum Mol Genet 23 (6):1413-1424. doi:10.1093/hmg/ddt528

130. Maier J, Traenkle B, Rothbauer U (2015) Real-time analysis of epithelial-mesenchymal transition using fluorescent single-domain antibodies. Scientific Reports 5 (1):13402. doi:10.1038/srep13402
131. Maiuri T, Mocle AJ, Hung CL, Xia J, van Roon-Mom WMC, Truant R (2017) Huntingtin is a scaffolding protein in the ATM oxidative DNA damage response complex. Human Molecular Genetics 26 (2):395-406. doi:10.1093/hmg/ddw395
132. Malli R, Frieden M, Osibow K, Zoratti C, Mayer M, Demaurex N, Graier WF (2003) Sustained Ca2+ transfer across mitochondria is Essential for mitochondrial Ca2+ buffering, sore-operated Ca2+ entry, and Ca2+ store refilling. J Biol Chem 278 (45):44769-44779. doi:10.1074/jbc.M302511200
133. Massa S, Vikani N, Betti C, Ballet S, Vanderhaegen S, Steyaert J, Descamps B, Vanhove C, Bunschoten A, van Leeuwen FWB, Hernot S, Caveliers V, Lahoutte T, Muyldermans S, Xavier C, Devoogdt N (2016) Sortase A-mediated site-specific labeling of camelid single-domain antibody-fragments: a versatile strategy for multiple molecular imaging modalities. Contrast Media and Molecular Imaging 11 (5):328-339. doi:10.1002/CMMI.1696
134. Matz J, Herate C, Bouchet J, Dusetti N, Gayet O, Baty D, Benichou S, Chames P (2014) Selection of intracellular single-domain antibodies targeting the HIV-1 Vpr protein by cytoplasmic yeast two-hybrid system. PLoS One 9 (12):e113729. doi:10.1371/journal.pone.0113729
135. Meeusen S, McCaffery JM, Nunnari J (2004) Mitochondrial fusion intermediates revealed in vitro. Science 305 (5691):1747-1752. doi:10.1126/science.1100612
136. Mikhaylova M, Cloin BM, Finan K, van den Berg R, Teeuw J, Kijanka MM, Sokolowski M, Katrukha EA, Maidorn M, Opazo F, Moutel S, Vantard M, Perez F, van Bergen en Henegouwen PM, Hoogenraad CC, Ewers H, Kapitein LC (2015) Resolving bundled microtubules using anti-tubulin nanobodies. Nat Commun 6:7933. doi:10.1038/ncomms8933
137. Misgeld T, Schwarz TL (2017) Mitostasis in Neurons: Maintaining Mitochondria in an Extended Cellular Architecture. Neuron 96 (3):651-666. doi:10.1016/j.neuron.2017.09.055
138. Mishra P, Chan DC (2014) Mitochondrial dynamics and inheritance during cell division, development and disease. Nature Reviews Molecular Cell Biology 15 (10):634-646. doi:10.1038/nrm3877
139. Mitchell LS, Colwell LJ (2018) Comparative analysis of nanobody sequence and structure data. Proteins 86 (7):697-706. doi:10.1002/prot.25497

140. Modi S, López-Doménech G, Halff EF, Covill-Cooke C, Ivankovic D, Melandri D, Arancibia-Cárcamo IL, Burden JJ, Lowe AR, Kittler JT (2019) Miro clusters regulate ER-mitochondria contact sites and link cristae organization to the mitochondrial transport machinery. Nature Communications 10 (1):4399. doi:10.1038/s41467-019-12382-4
141. Moller A, Bauer CS, Cohen RN, Webster CP, De Vos KJ (2017) Amyotrophic lateral sclerosis-associated mutant SOD1 inhibits anterograde axonal transport of mitochondria by reducing Miro1 levels. Human Molecular Genetics 26 (23):4668-4679. doi:10.1093/hmg/ddx348
142. Montecinos-Franjola F, Bauer BL, Mears JA, Ramachandran R (2020) GFP fluorescence tagging alters dynamin-related protein 1 oligomerization dynamics and creates disassembly-refractory puncta to mediate mitochondrial fission. Sci Rep 10 (1):14777. doi:10.1038/s41598-020-71655-x
143. Moutel S, Bery N, Bernard V, Keller L, Lemesre E, de Marco A, Ligat L, Rain JC, Favre G, Olichon A, Perez F (2016) NaLi-H1: A universal synthetic library of humanized nanobodies providing highly functional antibodies and intrabodies. eLife 5. doi:10.7554/eLife.16228
144. Mukherjee S, Erramilli SK, Ammirati M, Alvarez FJD, Fennell KF, Purdy MD, Skrobek BM, Radziwon K, Coukos J, Kang Y, Dutka P, Gao X, Qiu X, Yeager M, Eric Xu H, Han S, Kossiakoff AA (2020) Synthetic antibodies against BRIL as universal fiducial marks for single-particle cryoEM structure determination of membrane proteins. Nat Commun 11 (1):1598. doi:10.1038/s41467-020-15363-0
145. Munoz-Pinedo C, Guio-Carrion A, Goldstein JC, Fitzgerald P, Newmeyer DD, Green DR (2006) Different mitochondrial intermembrane space proteins are released during apoptosis in a manner that is coordinately initiated but can vary in duration. Proc Natl Acad Sci U S A 103 (31):11573-11578. doi:10.1073/pnas.0603007103
146. Muyldermans S (2013) Nanobodies: natural single-domain antibodies. Annual review of biochemistry 82:775-797. doi:10.1146/annurev-biochem-063011-092449
147. Muyldermans S (2021) A guide to: generation and design of nanobodies. FEBS J 288 (7):2084-2102. doi:10.1111/febs.15515
148. Muyldermans S, Atarhouch T, Saldanha J, Barbosa JA, Hamers R (1994) Sequence and structure of VH domain from naturally occurring camel heavy chain immunoglobulins lacking light chains. Protein Eng 7 (9):1129-1135. doi:10.1093/protein/7.9.1129
149. Muyldermans S, Baral TN, Retamozzo VC, De Baetselier P, De Genst E, Kinne J, Leonhardt H, Magez S, Nguyen VK, Revets H, Rothbauer U, Stijlemans B, Tillib S,

Wernery U, Wyns L, Hassanzadeh-Ghassabeh G, Saerens D (2009) Camelid immunoglobulins and nanobody technology. Veterinary Immunology and Immunopathology 128 (1):178-183. doi:https://doi.org/10.1016/j.vetimm.2008.10.299

150. Muyldermans S, Cambillau C, Wyns L (2001) Recognition of antigens by single-domain antibody fragments: the superfluous luxury of paired domains. Trends in biochemical sciences 26 (4):230-235. doi:10.1016/s0968-0004(01)01790-x

151. Nakahira K, Haspel JA, Rathinam VA, Lee SJ, Dolinay T, Lam HC, Englert JA, Rabinovitch M, Cernadas M, Kim HP, Fitzgerald KA, Ryter SW, Choi AM (2011) Autophagy proteins regulate innate immune responses by inhibiting the release of mitochondrial DNA mediated by the NALP3 inflammasome. Nat Immunol 12 (3):222-230. doi:10.1038/ni.1980

152. Nemani N, Carvalho E, Tomar D, Dong Z, Ketschek A, Breves SL, Jaña F, Worth AM, Heffler J, Palaniappan P, Tripathi A, Subbiah R, Riitano MF, Seelam A, Manfred T, Itoh K, Meng S, Sesaki H, Craigen WJ, Rajan S, Shanmughapriya S, Caplan J, Prosser BL, Gill DL, Stathopulos PB, Gallo G, Chan DC, Mishra P, Madesh M (2018) MIRO-1 Determines Mitochondrial Shape Transition upon GPCR Activation and Ca(2+) Stress. Cell reports 23 (4):1005-1019. doi:10.1016/j.celrep.2018.03.098

153. Nguyen D, Bharat V, Conradson DM, Nandakishore P, Wang X (2021) Miro1 Impairment in a Parkinson's At-Risk Cohort. Frontiers in molecular neuroscience 14:734273. doi:10.3389/fnmol.2021.734273

154. Nguyen TT, Oh SS, Weaver D, Lewandowska A, Maxfield D, Schuler MH, Smith NK, Macfarlane J, Saunders G, Palmer CA, Debattisti V, Koshiba T, Pulst S, Feldman EL, Hajnoczky G, Shaw JM (2014) Loss of Miro1-directed mitochondrial movement results in a novel murine model for neuron disease. Proc Natl Acad Sci U S A 111 (35):E3631-3640. doi:10.1073/pnas.1402449111

155. Ni H-M, Williams JA, Ding W-X (2015) Mitochondrial dynamics and mitochondrial quality control. Redox Biol 4:6-13. doi:10.1016/j.redox.2014.11.006

156. Norkett R, Lesept F, Kittler JT (2020) DISC1 Regulates Mitochondrial Trafficking in a Miro1-GTP-Dependent Manner. Front Cell Dev Biol 8:449. doi:10.3389/fcell.2020.00449

157. Nygren PA, Skerra A (2004) Binding proteins from alternative scaffolds. J Immunol Methods 290 (1-2):3-28. doi:10.1016/j.jim.2004.04.006

158. Oeding SJ, Majstrowicz K, Hu XP, Schwarz V, Freitag A, Honnert U, Nikolaus P, Bahler M (2018) Identification of Miro1 and Miro2 as mitochondrial receptors for myosin XIX. J Cell Sci 131 (17). doi:10.1242/jcs.219469

159. Oliver D, Reddy PH (2019) Dynamics of Dynamin-Related Protein 1 in Alzheimer's Disease and Other Neurodegenerative Diseases. Cells 8 (9):961. doi:10.3390/cells8090961
160. Otera H, Ishihara N, Mihara K (2013) New insights into the function and regulation of mitochondrial fission. Biochim Biophys Acta 1833 (5):1256-1268. doi:10.1016/j.bbamcr.2013.02.002
161. Pagliarini DJ, Rutter J (2013) Hallmarks of a new era in mitochondrial biochemistry. Genes Dev 27 (24):2615-2627. doi:10.1101/gad.229724.113
162. Pagliuso A, Cossart P, Stavru F (2018) The ever-growing complexity of the mitochondrial fission machinery. Cell Mol Life Sci 75 (3):355-374. doi:10.1007/s00018-017-2603-0
163. Palmer CS, Osellame LD, Laine D, Koutsopoulos OS, Frazier AE, Ryan MT (2011) MiD49 and MiD51, new components of the mitochondrial fission machinery. EMBO Rep 12 (6):565-573. doi:10.1038/embor.2011.54
164. Panza P, Maier J, Schmees C, Rothbauer U, Sollner C (2015) Live imaging of endogenous protein dynamics in zebrafish using chromobodies. Development 142 (10):1879-1884. doi:10.1242/dev.118943
165. Pardon E, Laeremans T, Triest S, Rasmussen SG, Wohlkonig A, Ruf A, Muyldermans S, Hol WG, Kobilka BK, Steyaert J (2014) A general protocol for the generation of Nanobodies for structural biology. Nat Protoc 9 (3):674-693. doi:10.1038/nprot.2014.039
166. Peruzzo R, Costa R, Bachmann M, Leanza L, Szabò I (2020) Mitochondrial Metabolism, Contact Sites and Cellular Calcium Signaling: Implications for Tumorigenesis. Cancers (Basel) 12 (9):2574. doi:10.3390/cancers12092574
167. Petersen OH (2002) Calcium signal compartmentalization. Biol Res 35 (2):177-182. doi:10.4067/s0716-97602002000200008
168. Pickles S, Vigié P, Youle RJ (2018) Mitophagy and Quality Control Mechanisms in Mitochondrial Maintenance. Curr Biol 28 (4):R170-R185. doi:10.1016/j.cub.2018.01.004
169. Pleiner T, Bates M, Trakhanov S, Lee CT, Schliep JE, Chug H, Bohning M, Stark H, Urlaub H, Gorlich D (2015) Nanobodies: site-specific labeling for super-resolution imaging, rapid epitope-mapping and native protein complex isolation. eLife 4:e11349. doi:10.7554/eLife.11349
170. Popp MW-L, Ploegh HL (2011) Making and Breaking Peptide Bonds: Protein Engineering Using Sortase. Angewandte Chemie International Edition 50 (22):5024-5032. doi:https://doi.org/10.1002/anie.201008267

171. Preger C, Wigren E, Ossipova E, Marks C, Lengqvist J, Hofstrom C, Andersson O, Jakobsson PJ, Graslund S, Persson H (2020) Generation and validation of recombinant antibodies to study human aminoacyl-tRNA synthetases. J Biol Chem 295 (41):13981-13993. doi:10.1074/jbc.RA120.012893
172. Prole DL, Taylor CW (2019) A genetically encoded toolkit of functionalized nanobodies against fluorescent proteins for visualizing and manipulating intracellular signalling. BMC Biol 17 (1):41. doi:10.1186/s12915-019-0662-4
173. Ramirez DH, Aonbangkhen C, Wu HY, Naftaly JA, Tang S, O'Meara TR, Woo CM (2020) Engineering a Proximity-Directed O-GlcNAc Transferase for Selective Protein O-GlcNAcylation in Cells. ACS Chem Biol 15 (4):1059-1066. doi:10.1021/acschembio.0c00074
174. Ravn U, Gueneau F, Baerlocher L, Osteras M, Desmurs M, Malinge P, Magistrelli G, Farinelli L, Kosco-Vilbois MH, Fischer N (2010) By-passing in vitro screening—next generation sequencing technologies applied to antibody display and in silico candidate selection. Nucleic Acids Research 38 (21):e193-e193. doi:10.1093/nar/gkq789
175. Reddy PH (2009) Amyloid beta, mitochondrial structural and functional dynamics in Alzheimer's disease. Exp Neurol 218 (2):286-292. doi:10.1016/j.expneurol.2009.03.042
176. Reddy PH, Reddy TP, Manczak M, Calkins MJ, Shirendeb U, Mao P (2011) Dynamin-related protein 1 and mitochondrial fragmentation in neurodegenerative diseases. Brain Res Rev 67 (1-2):103-118. doi:10.1016/j.brainresrev.2010.11.004
177. Reis K, Fransson Å, Aspenström P (2009) The Miro GTPases: At the heart of the mitochondrial transport machinery. FEBS Letters 583 (9):1391-1398. doi:10.1016/j.febslet.2009.04.015
178. Ries J, Kaplan C, Platonova E, Eghlidi H, Ewers H (2012) A simple, versatile method for GFP-based super-resolution microscopy via nanobodies. Nat Methods 9 (6):582-584. doi:10.1038/nmeth.1991
179. Roberts RF, Tang MY, Fon EA, Durcan TM (2016) Defending the mitochondria: The pathways of mitophagy and mitochondrial-derived vesicles. Int J Biochem Cell Biol 79:427-436. doi:10.1016/j.biocel.2016.07.020
180. Roca-Portoles A, Tait SWG (2021) Mitochondrial quality control: from molecule to organelle. Cell Mol Life Sci 78 (8):3853-3866. doi:10.1007/s00018-021-03775-0
181. Roe AJ, Qi X (2018) Drp1 phosphorylation by MAPK1 causes mitochondrial dysfunction in cell culture model of Huntington's disease. Biochemical and biophysical research communications 496 (2):706-711. doi:10.1016/j.bbrc.2018.01.114

182. Rothbauer U, Zolghadr K, Muyldermans S, Schepers A, Cardoso MC, Leonhardt H (2008) A versatile nanotrap for biochemical and functional studies with fluorescent fusion proteins. Mol Cell Proteomics 7 (2):282-289. doi:10.1074/mcp.M700342-MCP200
183. Rothbauer U, Zolghadr K, Tillib S, Nowak D, Schermelleh L, Gahl A, Backmann N, Conrath K, Muyldermans S, Cardoso MC, Leonhardt H (2006) Targeting and tracing antigens in live cells with fluorescent nanobodies. Nat Methods 3 (11):887-889. doi:10.1038/nmeth953
184. Roux KJ, Kim DI, Raida M, Burke B (2012) A promiscuous biotin ligase fusion protein identifies proximal and interacting proteins in mammalian cells. J Cell Biol 196 (6):801-810. doi:10.1083/jcb.201112098
185. Rube DA, Van Der Bliek AM (2004) Mitochondrial morphology is dynamic and varied. Molecular and Cellular Biochemistry, vol 256.
186. Ruthel G, Hollenbeck PJ (2003) Response of mitochondrial traffic to axon determination and differential branch growth. J Neurosci 23 (24):8618-8624
187. Samangouei P, Crespo-Avilan GE, Cabrera-Fuentes H, Hernandez-Resendiz S, Ismail NI, Katwadi KB, Boisvert WA, Hausenloy DJ (2018) MiD49 and MiD51: New mediators of mitochondrial fission and novel targets for cardioprotection. Cond Med 1 (5):239-246
188. Saotome M, A S, Szabadkai G, Das S, Fransson Å, Aspenstrom P, Rizzuto R, Hajnoczky G (2008) Bidirectional Ca2+-dependent control of mitochondrial dynamics by the Miro GTPase. Proceedings of the National Academy of Sciences 105:20728. doi:10.1073/pnas.0808953105
189. Sarraf SA, Raman M, Guarani-Pereira V, Sowa ME, Huttlin EL, Gygi SP, Harper JW (2013) Landscape of the PARKIN-dependent ubiquitylome in response to mitochondrial depolarization. Nature 496 (7445):372-376. doi:10.1038/nature12043
190. Schlehuber S, Skerra A (2005) Lipocalins in drug discovery: from natural ligand-binding proteins to "anticalins". Drug Discov Today 10 (1):23-33. doi:10.1016/S1359-6446(04)03294-5
191. Schmidthals K (2013) Generation and characterization of heavy-chain antibodies derived from Camelids.,
192. Schornack S, Fuchs R, Huitema E, Rothbauer U, Lipka V, Kamoun S (2009) Protein mislocalization in plant cells using a GFP-binding chromobody. Plant J 60 (4):744-754. doi:10.1111/j.1365-313X.2009.03982.x
193. Schorpp K, Rothenaigner I, Maier J, Traenkle B, Rothbauer U, Hadian K (2016) A Multiplexed High-Content Screening Approach Using the Chromobody Technology to

Identify Cell Cycle Modulators in Living Cells. J Biomol Screen 21 (9):965-977. doi:10.1177/1087057116641935

194. Serasinghe MN, Chipuk JE (2017) Mitochondrial Fission in Human Diseases. Handb Exp Pharmacol 240:159-188. doi:10.1007/164_2016_38

195. Shaltouki A, Hsieh CH, Kim MJ, Wang X (2018) Alpha-synuclein delays mitophagy and targeting Miro rescues neuron loss in Parkinson's models. Acta Neuropathol 136 (4):607-620. doi:10.1007/s00401-018-1873-4

196. Sigoillot M, Overtus M, Grodecka M, Scholl D, Garcia-Pino A, Laeremans T, He L, Pardon E, Hildebrandt E, Urbatsch I, Steyaert J, Riordan JR, Govaerts C (2019) Domain-interface dynamics of CFTR revealed by stabilizing nanobodies. Nature Communications 10 (1):2636. doi:10.1038/s41467-019-10714-y

197. Skerra A (2007) Alternative non-antibody scaffolds for molecular recognition. Curr Opin Biotechnol 18 (4):295-304. doi:10.1016/j.copbio.2007.04.010

198. Skrlec K, Strukelj B, Berlec A (2015) Non-immunoglobulin scaffolds: a focus on their targets. Trends Biotechnol 33 (7):408-418. doi:10.1016/j.tibtech.2015.03.012

199. Slastnikova TA, Ulasov AV, Rosenkranz AA, Sobolev AS (2018) Targeted Intracellular Delivery of Antibodies: The State of the Art. Front Pharmacol 9:1208. doi:10.3389/fphar.2018.01208

200. Smirnova E, Griparic L, Shurland DL, van der Bliek AM (2001) Dynamin-related protein Drp1 is required for mitochondrial division in mammalian cells. Mol Biol Cell 12 (8):2245-2256. doi:10.1091/mbc.12.8.2245

201. Smith GP (1985) Filamentous fusion phage: novel expression vectors that display cloned antigens on the virion surface. Science 228 (4705):1315-1317. doi:10.1126/science.4001944

202. Smith KP, Focia PJ, Chakravarthy S, Landahl EC, Klosowiak JL, Rice SE, Freymann DM (2020) Insight into human Miro1/2 domain organization based on the structure of its N-terminal GTPase. Journal of Structural Biology 212 (3):107656. doi:https://doi.org/10.1016/j.jsb.2020.107656

203. Song W, Chen J, Petrilli A, Liot G, Klinglmayr E, Zhou Y, Poquiz P, Tjong J, Pouladi MA, Hayden MR, Masliah E, Ellisman M, Rouiller I, Schwarzenbacher R, Bossy B, Perkins G, Bossy-Wetzel E (2011) Mutant huntingtin binds the mitochondrial fission GTPase dynamin-related protein-1 and increases its enzymatic activity. Nat Med 17 (3):377-382. doi:10.1038/nm.2313

204. Steeland S, Vandenbroucke RE, Libert C (2016) Nanobodies as therapeutics: big opportunities for small antibodies. Drug Discov Today 21 (7):1076-1113. doi:10.1016/j.drudis.2016.04.003

205. Steels A, Verhelle A, Zwaenepoel O, Gettemans J (2018) Intracellular displacement of p53 using transactivation domain (p53 TAD) specific nanobodies. MAbs 10 (7):1045-1059. doi:10.1080/19420862.2018.1502025
206. Stephenson FA (2010) Activity-dependent immobilization of mitochondria: the role of miro. Frontiers in molecular neuroscience 3:9. doi:10.3389/fnmol.2010.00009
207. Stijlemans B, Conrath K, Cortez-Retamozo V, Van Xong H, Wyns L, Senter P, Revets H, De Baetselier P, Muyldermans S, Magez S (2004) Efficient targeting of conserved cryptic epitopes of infectious agents by single domain antibodies. African trypanosomes as paradigm. J Biol Chem 279 (2):1256-1261. doi:10.1074/jbc.M307341200
208. Suárez-Rivero JM, Villanueva-Paz M, de la Cruz-Ojeda P, de la Mata M, Cotán D, Oropesa-Ávila M, de Lavera I, Álvarez-Córdoba M, Luzón-Hidalgo R, Sánchez-Alcázar JA (2016) Mitochondrial Dynamics in Mitochondrial Diseases. Diseases 5 (1):1. doi:10.3390/diseases5010001
209. Sultana A, Lee JE (2015) Measuring Protein-Protein and Protein-Nucleic Acid Interactions by Biolayer Interferometry. Curr Protoc Protein Sci 79. doi:10.1002/0471140864.ps1925s79
210. Suzuki T, Mochizuki Y, Kimura S, Akazawa-Ogawa Y, Hagihara Y, Nemoto N (2018) Anti-survivin single-domain antibodies derived from an artificial library including three synthetic random regions by in vitro selection using cDNA display. Biochem Biophys Res Commun 503 (3):2054-2060. doi:10.1016/j.bbrc.2018.07.158
211. Tafuri F, Ronchi D, Magri F, Comi GP, Corti S (2015) SOD1 misplacing and mitochondrial dysfunction in amyotrophic lateral sclerosis pathogenesis. Front Cell Neurosci 9:336. doi:10.3389/fncel.2015.00336
212. Thammasit P, Sangboonruang S, Suwanpairoj S, Khamaikawin W, Intasai N, Kasinrerk W, Tayapiwatana C, Tragoolpua K (2015) Intracellular Acidosis Promotes Mitochondrial Apoptosis Pathway: Role of EMMPRIN Down-regulation via Specific Single-chain Fv Intrabody. J Cancer 6 (3):276-286. doi:10.7150/jca.10879
213. Tikunova NV, Morozova VV (2009) Phage display on the base of filamentous bacteriophages: application for recombinant antibodies selection. Acta Naturae 1 (3):20-28
214. Tilokani L, Nagashima S, Paupe V, Prudent J (2018) Mitochondrial dynamics: overview of molecular mechanisms. Essays in biochemistry 62 (3):341-360. doi:10.1042/EBC20170104

215. Traenkle B, Rothbauer U (2017) Under the Microscope: Single-Domain Antibodies for Live-Cell Imaging and Super-Resolution Microscopy. Front Immunol 8:1030. doi:10.3389/fimmu.2017.01030
216. Traenkle B, Segan S, Fagbadebo FO, Kaiser PD, Rothbauer U (2020) A novel epitope tagging system to visualize and monitor antigens in live cells with chromobodies. Scientific reports 10 (1):1-13
217. van der Bliek AM, Shen Q, Kawajiri S (2013) Mechanisms of mitochondrial fission and fusion. Cold Spring Harb Perspect Biol 5 (6). doi:10.1101/cshperspect.a011072
218. van der Linden RH, Frenken LG, de Geus B, Harmsen MM, Ruuls RC, Stok W, de Ron L, Wilson S, Davis P, Verrips CT (1999) Comparison of physical chemical properties of llama VHH antibody fragments and mouse monoclonal antibodies. Biochim Biophys Acta 1431 (1):37-46. doi:10.1016/s0167-4838(99)00030-8
219. van Spronsen M, Mikhaylova M, Lipka J, Schlager Max A, van den Heuvel Dave J, Kuijpers M, Wulf Phebe S, Keijzer N, Demmers J, Kapitein Lukas C, Jaarsma D, Gerritsen Hans C, Akhmanova A, Hoogenraad Casper C (2013) TRAK/Milton Motor-Adaptor Proteins Steer Mitochondrial Trafficking to Axons and Dendrites. Neuron 77 (3):485-502. doi:10.1016/j.neuron.2012.11.027
220. Virant D, Traenkle B, Maier J, Kaiser PD, Bodenhofer M, Schmees C, Vojnovic I, Pisak-Lukats B, Endesfelder U, Rothbauer U (2018) A peptide tag-specific nanobody enables high-quality labeling for dSTORM imaging. Nat Commun 9 (1):930. doi:10.1038/s41467-018-03191-2
221. Vlahou G, Elias M, von Kleist-Retzow JC, Wiesner RJ, Rivero F (2011) The Ras related GTPase Miro is not required for mitochondrial transport in Dictyostelium discoideum. Eur J Cell Biol 90 (4):342-355. doi:10.1016/j.ejcb.2010.10.012
222. Vosjan MJ, Perk LR, Roovers RC, Visser GW, Stigter-van Walsum M, van Bergen En Henegouwen PM, van Dongen GA (2011) Facile labelling of an anti-epidermal growth factor receptor Nanobody with 68Ga via a novel bifunctional desferal chelate for immuno-PET. Eur J Nucl Med Mol Imaging 38 (4):753-763. doi:10.1007/s00259-010-1700-1
223. Wagner TR, Rothbauer U (2020) Nanobodies Right in the Middle: Intrabodies as Toolbox to Visualize and Modulate Antigens in the Living Cell. Biomolecules 10 (12). doi:10.3390/biom10121701
224. Wagner TR, Rothbauer U (2021) Nanobodies – Little helpers unravelling intracellular signaling. Free Radical Biology and Medicine 176:46-61. doi:https://doi.org/10.1016/j.freeradbiomed.2021.09.005

225. Wang H, Zhang Y, Zeng K, Qiang J, Cao Y, Li Y, Fang Y, Zhang Y, Chen Y (2021) Selective Mitochondrial Protein Labeling Enabled by Biocompatible Photocatalytic Reactions inside Live Cells. JACS Au 1 (7):1066-1075. doi:10.1021/jacsau.1c00172
226. Wang X, Schwarz TL (2009) The Mechanism of Ca2+-Dependent Regulation of Kinesin-Mediated Mitochondrial Motility. Cell 136 (1):163-174. doi:10.1016/J.CELL.2008.11.046
227. Wang X, Winter D, Ashrafi G, Schlehe J, Wong YL, Selkoe D, Rice S, Steen J, LaVoie MJ, Schwarz TL (2011) PINK1 and Parkin target Miro for phosphorylation and degradation to arrest mitochondrial motility. Cell 147 (4):893-906. doi:10.1016/j.cell.2011.10.018
228. Warnders FJ, Terwisscha van Scheltinga AGT, Knuehl C, van Roy M, de Vries EFJ, Kosterink JGW, de Vries EGE, Lub-de Hooge MN (2017) Human Epidermal Growth Factor Receptor 3-Specific Tumor Uptake and Biodistribution of (89)Zr-MSB0010853 Visualized by Real-Time and Noninvasive PET Imaging. J Nucl Med 58 (8):1210-1215. doi:10.2967/jnumed.116.181586
229. Weihofen A, Thomas KJ, Ostaszewski BL, Cookson MR, Selkoe DJ (2009) Pink1 forms a multiprotein complex with Miro and Milton, linking Pink1 function to mitochondrial trafficking. Biochemistry 48 (9):2045-2052. doi:10.1021/bi8019178
230. Weinberg Samuel E, Sena Laura A, Chandel Navdeep S (2015) Mitochondria in the Regulation of Innate and Adaptive Immunity. Immunity 42 (3):406-417. doi:https://doi.org/10.1016/j.immuni.2015.02.002
231. Wells RC, Picton LK, Williams SCP, Tan FJ, Hill RB (2007) Direct binding of the dynamin-like GTPase, Dnm1, to mitochondrial dynamics protein Fis1 is negatively regulated by the Fis1 N-terminal arm. J Biol Chem 282 (46):33769-33775. doi:10.1074/jbc.M700807200
232. West AP, Shadel GS, Ghosh S (2011) Mitochondria in innate immune responses. Nature Reviews Immunology 11 (6):389-402. doi:10.1038/nri2975
233. Whitley BN, Lam C, Cui H, Haude K, Bai R, Escobar L, Hamilton A, Brady L, Tarnopolsky MA, Dengle L, Picker J, Lincoln S, Lackner LL, Glass IA, Hoppins S (2018) Aberrant Drp1-mediated mitochondrial division presents in humans with variable outcomes. Hum Mol Genet 27 (21):3710-3719. doi:10.1093/hmg/ddy287
234. Xavier C, Vaneycken I, D'Huyvetter M, Heemskerk J, Keyaerts M, Vincke C, Devoogdt N, Muyldermans S, Lahoutte T, Caveliers V (2013) Synthesis, preclinical validation, dosimetry, and toxicity of 68Ga-NOTA-anti-HER2 Nanobodies for iPET imaging of HER2 receptor expression in cancer. J Nucl Med 54 (5):776-784. doi:10.2967/jnumed.112.111021

235. Xian H, Liou YC (2021) Functions of outer mitochondrial membrane proteins: mediating the crosstalk between mitochondrial dynamics and mitophagy. Cell Death Differ 28 (3):827-842. doi:10.1038/s41418-020-00657-z

236. Yaari G, Kleinstein SH (2015) Practical guidelines for B-cell receptor repertoire sequencing analysis. Genome Medicine 7 (1):121. doi:10.1186/s13073-015-0243-2

237. Yamaoka S, Hara-Nishimura I (2014) The mitochondrial Ras-related GTPase Miro: views from inside and outside the metazoan kingdom. Front Plant Sci 5:350-350. doi:10.3389/fpls.2014.00350

238. Yu R, Lendahl U, Nister M, Zhao J (2020) Regulation of Mammalian Mitochondrial Dynamics: Opportunities and Challenges. Front Endocrinol (Lausanne) 11:374. doi:10.3389/fendo.2020.00374

239. Zhang C, Liu Z, Bunker E, Ramirez A, Lee S, Peng Y, Tan A-C, Eckhardt SG, Chapnick DA, Liu X (2017) Sorafenib targets the mitochondrial electron transport chain complexes and ATP synthase to activate the PINK1-Parkin pathway and modulate cellular drug response. J Biol Chem 292 (36):15105-15120. doi:10.1074/jbc.M117.783175

240. Zhang F, Wang W, Siedlak SL, Liu Y, Liu J, Jiang K, Perry G, Zhu X, Wang X (2015) Miro1 deficiency in amyotrophic lateral sclerosis. Front Aging Neurosci 7:100-100. doi:10.3389/fnagi.2015.00100

241. Zhang Q, Raoof M, Chen Y, Sumi Y, Sursal T, Junger W, Brohi K, Itagaki K, Hauser CJ (2010) Circulating mitochondrial DAMPs cause inflammatory responses to injury. Nature 464 (7285):104-107. doi:10.1038/nature08780

242. Zhao X, Tian C, Puszyk WM, Ogunwobi OO, Cao M, Wang T, Cabrera R, Nelson DR, Liu C (2013) OPA1 downregulation is involved in sorafenib-induced apoptosis in hepatocellular carcinoma. Laboratory Investigation 93 (1):8-19. doi:10.1038/labinvest.2012.144

243. Zhao Y, Song E, Wang W, Hsieh C-H, Wang X, Feng W, Wang X, Shen K (2021) Metaxins are core components of mitochondrial transport adaptor complexes. Nature Communications 12 (1):83. doi:10.1038/s41467-020-20346-2

244. Zhou R, Yazdi AS, Menu P, Tschopp J (2011) A role for mitochondria in NLRP3 inflammasome activation. Nature 469 (7329):221-225. doi:10.1038/nature09663

245. Zhu PP, Patterson A, Stadler J, Seeburg DP, Sheng M, Blackstone C (2004) Intra- and intermolecular domain interactions of the C-terminal GTPase effector domain of the multimeric dynamin-like GTPase Drp1. J Biol Chem 279 (34):35967-35974. doi:10.1074/jbc.M404105200

246. Zolghadr K, Gregor J, Leonhardt H, Rothbauer U (2012) Case study on live cell apoptosis-assay using lamin-chromobody cell-lines for high-content analysis. Methods Mol Biol 911:569-575. doi:10.1007/978-1-61779-968-6_36

247. Zolghadr K, Mortusewicz O, Rothbauer U, Kleinhans R, Goehler H, Wanker EE, Cardoso MC, Leonhardt H (2008) A fluorescent two-hybrid assay for direct visualization of protein interactions in living cells. Mol Cell Proteomics 7 (11):2279-2287. doi:M700548-MCP200 [pii]

6 ANNEX

6.1 Publications

Parts of this thesis are published in:

Fagbadebo FO, Kaiser PD, Zittlau K, Bartlick N, Wagner TR, Froehlich T, Jarjour G, Nueske S, Scholz A, Traenkle B, Macek B, Rothbauer U (2022). A Nanobody-Based Toolset to Monitor and Modify the Mitochondrial GTPase Miro1. Front Mol Biosci 9:835302. doi:10.3389/fmolb.2022.835302

Other publications:

Fagbadebo FO, Rothbauer U (2022) Peptide-Tag Specific Nanobodies for Studying Proteins in Live Cells. Methods Mol Biol 2446:555-579. doi:10.1007/978-1-0716-2075-5_29

Traenkle B, Segan S, **Fagbadebo FO**, Kaiser PD, Rothbauer U (2020) A novel epitope tagging system to visualize and monitor antigens in live cells with chromobodies. Scientific reports 10 (1):1-13

6.2 Acknowledgements

My gratitude goes to my supervisor, Prof. Dr Ulrich Rothbauer for giving me the opportunity to study and grow in his lab. Thank you Uli for the training and support you gave me, and most especially for teaching me to pursue answers logically.

I am very grateful to Prof. Dr Thilo Stehle and Prof. Dr Steffen Jung for the advice and constructive feedback I received during my yearly TAC meetings. Thank you for your prompt responses too.

My appreciation goes to all members of the Rothbauer lab at NMI, Reutlingen: Philipp Kaiser, for his constant counsel, willingness to help and for teaching me almost everything I know about molecular biology methods, Björn Traenkle for sharing insights regarding microscopy and other things, Sandra Burgstaller for her advice and encouragement, Teresa Wagner for her advice and assistance with BLI measurements, Desiree Frecot for her advice and making the lab a warm place, Theresa Fröhlich for her collaboration in the final stages of my project and Ursula Härle for her willingness to help. I am especially grateful to lab alumni, Sören Segan for his kindness and assistance during and after his time at the lab, thank you.

I would like to thank all members of MOMbrane GRK2364 for providing a great scientific environment, thank you all for the support and collaborative efforts. I specially want to thank Natascha Bartlick for providing countless batches of Miro1, Andreas Jenner for supplying DRP1, Katharina Zittlau for the last-minute MS experiments, Lisa Schwarz and Dr Julia Fitzgerald for their suggestions, protocols, and collaboration. I appreciate Dr Regina Grupp for her kindness, patience and for her assistance in navigating a lot of administrative issues.

Finally, I want to thank my family and friends for their unending support. To my dad and Mama, thank you for your prayers and words of comfort, my brothers, Yinka and Kay, thanks for listening to my complaints and for the continuous motivation. My special thanks go to my sister, Funke, for being a rock, thank you so much for being there. To a friend like no other, Tope, thank you and yes, we did it! To the ICCG family, the Ntie-Kangs, Rosy and Sabbath, thanks for your support.

Most importantly, I could never have done this without my Maker and Friend who carried me through the good and the dark days in a foreign land.